UNIVERSITY OF BERGEN

Department of Physics and Technology

MASTER'S THESIS IN OCEAN TECHNOLOGY

Optimisation of multi-rotor wind turbine configurations for maximum performance

---

Daniel Kvalheim

June 2024

Abstract

Increasing demand for renewable energy has made wind energy a prolific part of the energy race. As wind turbines continue to expand with hub heights reaching 150 m and rotor diameters reaching 250 m, critical challenges concerning transportation and manufacturing appear. The need for new solutions to counteract the trend arises. Multi-rotor wind turbines show potential for solving this problem. Several experiments have been performed on different multi-rotor configurations, investigating parameters such as wake flow, aerodynamic performance and power production. Using computational fluid dynamics analysis, this thesis investigated the optimal distance between rotors in a multi-rotor configuration consisting of seven rotors for maximising its performance. The simulation models were validated and compared against experimental data gathered at the Western Norway University of Applied Sciences and at the Carl von Ossietzky Universität Oldenburg. A surrogate-based optimisation was employed to reveal the optimal distance.

The findings of the thesis indicated that an inter-rotor spacing of s/d=1.0 (one rotor diameter between each rotor) is optimal for maximising the performance of the multi-rotor configuration with seven rotors. The power- and thrust coefficients were maximised for this spacing, and the velocity deficit in the wake was minimised. An increase of 7.8 % in power coefficient is discovered for an inter-rotor spacing of s/d=1.0 compared to s/d=0.0. For the thrust coefficient, an increase of 3.7 % is measured for the same comparison. Concerning velocity deficit at four diameters downstream, the spacing of s/d=1.0 shows a mean velocity deficit of 0.22, a decrease of 172 % compared to the mean velocity deficit of 0.59 with a spacing of s/d=0.0.

Multi-rotor simulation results showed good agreement in the rotor plane compared to experimental data, but deviations were observed in the wake due to the lack of mixing and velocity recovery. As the forces and power acting in the rotor are affected by the wake flow, the deviations in the wake may have led to consequential errors in the simulated thrust force and power output.

- This page is intentionally left blank -

Acknowledgments

I would like to express my sincerest gratitude to a number of people involved in the completion of this master's thesis.

First of all, I must express my gratefulness to my supervisors Jan Bartl and Thomas Hansen, Associate Professors at the Western Norway University of Applied Sciences (HVL). Thanks for the great discussions, good help along the way, and for being sincere individuals who I respect and have appreciated working with. A special thanks go to Professor Bjørn Tore Hjertaker, my supervisor from the University of Bergen (UiB). Thanks for proofreading, feedback and support through all my years studying Ocean Technology at UiB, I am forever grateful for five fantastic years here.

Furthermore, I want to thank my fellow students at Ocean Technology for making the years of studying both joyful and educational. Thanks for all the hours studying together, solving calculus problems, 3D-modelling of bearings and shafts, and analysing floating offshore wind turbines, it's been a joy. Thanks to Amalie, my girlfriend, for always being able to shift my mood after long days of working towards the completion of this thesis. Thanks to my family, for always having my back and encouraging me to do my best work.

- This page is intentionally left blank -

Contents

List of Figures

List of Tables

List of abbreviations

AD Actuator Disc

AEP Annual Energy Production

BEM Blade Element Momentum

CFD Computational Fluid Dynamics

DES Detached Eddy Simulation

DNS Direct Numerical Simulation

EU European Union

GHG Greenhouse Gases

HAWT Horizontal-Axis Wind Turbine

RANS Reynolds-averaged Navier-Stokes

LES Large Eddy Simulation

LCA Life Cycle Assessment

MWT Model Wind Turbine

MR Multi-Rotor

MR4 Multi-Rotor setup with four rotors

MR7 Multi-Rotor setup with seven rotors

PD Porous Disc

SR Single-Rotor

SBO Surrogate-based Optimisation

UDM User Defined Method

Chapter 1

Introduction

Det Norske Veritas (DNV)[1] has forecasted that energy-related CO_2 emissions in 2030 will only be 4 % lower than they are today and that the pace of the energy transition is far from fast enough for reaching a net-zero energy system by 2050, as stated in the Paris Agreement [2] from 2015. The overachieving goal of the Paris Agreement [2] is to hold the increase in the global average temperature to well below 2 °C above pre-industrial levels and pursue efforts to limit the temperature increase to 1.5 °C above pre-industrial levels. DNV also states that from 2030 and going forward nearly all energy additions will be wind and solar [1]. Wind energy capacity is projected to increase by a factor of nine between the present time and 2050.

According to the United Nations (UN) [3], fossil fuels still account for more than 80 % of global energy production, but cleaner sources of energy are gaining ground. About 29 % of electricity currently comes from renewable sources of energy. In 2021, more than 22 % of the gross final energy consumed in the European Union (EU) came from renewables, but the share of renewables in the energy mix varies substantially across the EU [4].

Recent reports (Nov 2023) from the UN Climate Change [5] indicate that national climate action plans remain insufficient to limit global temperature rise to 1.5 °C and thereby meet the goals set in the Paris Agreement. The current progress towards the goals is too slow. The latest science states that greenhouse gas (GHG) emissions need to be cut by 43 % by 2030, compared with 2019 levels [5]. That is a critical point to limit temperature rise to 1.5 °C by the end of this century and avoid the worst impacts of climate change such as natural disasters.

DNV states that wind energy will play a crucial role in reaching net-zero energy systems by 2050 [1]. Wind energy is a clean source of energy, as its systems are energised only by the naturally flowing wind. Wind does not pollute air like power plants, which rely on the combustion of fossil fuels, such as coal or natural gas. Wind turbines do not produce any atmospheric emissions that will cause acid rain or greenhouse gases [6]. Wind energy is also a domestic source of energy, and is not confined to a limited amount countries, as in the case of oil.

Although all sources of electricity emit some emissions during their lifetime, wind energy systems have significantly lower emissions than conventional coal and gas as illustrated in Table 1.1.

Table 1.1: *Lifetime emissions from conventional coal, gas and wind power plants. Data retrieved from Ackerman & Söder [7].*

Pollutant	**Conventional Coal**	**Gas**	**Wind**
Sulfur oxides SO_x [kg/GWh]	630 - 1370	45 - 140	2 - 8
Nitrogen oxides NO_x [kg/GWh]	630 - 1560	650 - 810	14 - 22
Carbon dioxide CO_2 [kg/GWh]	830 000 - 920 000	370 000 - 420 000	10 000 - 17 000

Such findings about CO_2-emissions from wind power plants have also been found by Bonou et al. [8]. In their study, life cycle assessment (LCA) was assessed on both onshore and offshore wind power plants in Europe. Findings from this study showcased that the energy payback time was less than a year for both onshore and offshore plants, and GHG emissions were less than 7 g CO_2-eq/kWh for onshore and less than 11 g CO_2-eq/kWh for offshore plants. Isolated, those numbers do not tell much, but when compared with LCAs of natural gas (437-758 g CO_2-eq/kWh) [9] and coal (675-1689 g CO_2-eq/kWh) [10], the CO_2-eq/kWh emissions from wind farms are significantly lower.

In 2022, Europe witnessed 19.1 GW of new wind installations, distributed by 16.7 GW onshore and 2.5 GW offshore [11]. The average power rating for turbines installed onshore was 4.1 MW, and offshore the average rated capacity was 8 MW. Challenges in 2022 included both the difficult economic environment and supply chain difficulties. More challenges will appear as wind turbines grow to a rated power of 20 MW, with rotor diameters of 250 m and hub heights

of 150 m, as discussed in Sieros et al. [12]. In this article, geometrical similarity was used to assess the theoretical implications of upscaling to such sizes. It was shown that the limiting loads increase with scale, and unfavourable conditions were imposed for such wind turbines. An unfavourable weight increase was also shown for the upscaling of wind turbines.

As modern wind turbines tend to increase in both size and weight, the need for new concepts within wind energy that counteract this trend arises. The introduction of larger turbine blades not only calls for the deployment of larger cranes for handling and installation but also necessitates larger vehicles for transportation. The counteract to this trend of increasingly larger turbine blades can be standardisation of parts, a solution which fits perfectly for multi-rotor (MR) wind turbines. MR systems offer advantages in terms of standardisation, transportation and ease of installation and maintenance as discussed in Verma [13].

1.1 Motivation for Multi-Rotor Wind Turbines

Similar to Sieros et al. [12], Jamieson and Branney [14] stated in an article from 2012 how the upscaling of traditional wind turbines was becoming a problem considering the area-to-weight relationship of wind turbines. The ratio of the mass, R, between a multi-rotor to that of a large single-rotor (SR) is determined by

$$R = \frac{1}{\sqrt{n}} \tag{1.1}$$

where n is the number of rotors in the multi-rotor setup. MR wind turbines take advantage of the area-to-weight relationship, by having a lower weight for the same area. The swept area is a contributor to the power production from wind turbines, which will be further looked upon in Chapter 2. Results from the study suggested that four 5 MW rotors will cost ~ 80 % of a single 20 MW rotor and that a 20 MW multi-rotor system can further reduce the cost to ~ 89 % of four 5 MW rotors or ~ 70 % of a 20 MW single-rotor.

Further studies on MR wind turbines have been performed by van der Laan et al. [15]. In this article, numerical and field measurements were conducted on the Vestas multi-rotor wind turbine (4R-V29), displayed in Figure 1.1, a multi-rotor demonstrator with four rotors (MR4) located at Risø Campus in Denmark at the Technical University of Denmark (DTU).

Figure 1.1: *Vestas multi-rotor demonstrator. Each rotor has a diameter of 29.2 m, and the tip spacing is 1.82 m. Retrieved from [15].*

Numerical simulations showed an enhancement of 0-2 % in power performance due to rotor interaction below rated wind speed, as a result of increased thrust force and axial induction factor [15]. The increase in power performance below rated wind speed can lead to an increase in annual energy production (AEP) of 1.5 %. Near wake measurements showed four distinct wake deficits which merge into a single structure at 2-3D, with D being the rotor diameter of 29.2 m. Compared with an equivalent single-rotor, Reynolds-averaged Navier-Stokes (RANS) simulations of the wake recovery showed a shorter wake recovery distance for the 4R-V29, which could lead to more closely spaced wind turbines in a multi-rotor wind farm compared to a single-rotor wind farm.

Another numerical simulation on multi-rotors was performed by Ghaisas et al. [16]. A Large Eddy Simulation (LES) study on multi-rotor wind turbines was carried out and compared with a single-rotor wind turbine. Different multi-rotor configurations were simulated, with varying spacings between the rotors in an MR4 setup. The smaller rotors had a diameter half of the diameter of the single-rotor (d=D/2). It was shown that the velocity deficit was

significantly reduced for the MR4 compared with the SR at each downstream distance. This is due to the individual rotor wakes for the MR4 having a characteristic length scale d=D/2, while the SR recovers with a characteristic length of D. The reduced recovery distance can also be associated with the fact that the MR4 has a rotor perimeter-to-frontal area ratio that is twice that of the SR. This enables greater entrainment and faster recovery of the wake, particularly in the near wake region. The study concluded that MR4 turbines are particularly beneficial when the spacings between turbines are relatively close, and when the operating thrust coefficient is large in a wind farm layout.

Bastankhah and Akbar [17] also utilised LES on an MR4 setup to compare the wake flow properties of a multi-rotor wind turbine with those of a single-rotor wind turbine. The selected diameter value of the SR was 80 m (D), such that the rotor diameter for the MR4 setup was 40 m (d), and the inter-rotor spacing was set to s/d=0.1, inspired by the Vestas 4R-V29 demonstrator. Downstream, the mixing of the individual rotor wakes by the MR4 makes the whole wake more uniformly distributed at 4D. At 7D, the wakes of both the MR4 and SR resembled each other, while at 10D the wakes had almost identical mean flow distribution. Regarding inter-rotor spacing, it was shown in the study that the velocity deficit downstream in the range where a downwind turbine is usually located was lower for all tested rotor spacings (s/d=0, s/d=0.1, s/d=0.25, with s being tip-to-tip spacing in the MR4 setup). An increase in rotor spacing extends the streamwise distance each rotor wake can travel downstream without strong interactions with the neighbouring rotor wakes. It was concluded that MR wind turbines can mitigate wake effects in wind farms. All the tested MR wakes were associated with lower velocity deficit and turbulence intensity downstream where a second turbine is usually placed.

Energy production from a wind farm consisting of multi-rotor wind turbines was investigated by van der Laan and Akbar [18]. A 4x4 rectangular wind farm layout was investigated using RANS simulations, and three different inter-spacings were tested (3, 4 and 5D, with D being the diameter of the SR). The DTU-10MW single-rotor wind turbine was compared to a multi-rotor system consisting of four downscaled versions of the DTU-10MW turbine. Simulations indicated an increase in AEP of 0.3-1.7 % for the MR farm compared to the SR wind farm. This was mainly because the wake recovers faster for the MR wind turbine, which makes the first

downstream wind turbine experience 7-16 % more power in the MR wind farm. The results from this study are in contradiction with the results from Ghaisas et al. [16], which showed that all downstream MR wind turbines in a row of five wind turbines produce 15-45 % more power compared to SR wind turbines in a row. Therefore, an additional LES test case was performed to show that the results in Ghaisas et al. [16] were caused by unrealistically large tip clearances.

A similar approach was chosen by Chasapiogannis et al. [19], when the aerodynamic performance of the MR7 concept was analysed. The SR had the same diameter as each of the rotors in the MR7 setup. The performance of the MR7 compared with the SR case predicted an increase of ~ 3 % in power generation and an ~ 1.5 % increase in thrust force. The individual wake cores of the MR7 merged into one wake at a distance comparable to the SR's core length. Regarding axial loading, the central rotor in the MR7 experienced 2 % more loading in comparison to the SR. The study concluded that, from an aerodynamic standpoint, the MR7 will deliver performance on par with that of seven single-rotors.

An increase in power extraction was also discovered by Nishino and Draper [20] in their investigation of the effect of local blockage on wind turbines. A combined theoretical and CFD study was conducted on power extraction from a closely spaced lateral array of wind turbines. RANS simulations with actuator discs indicated an increase of 5 % in power extraction for a closely spaced array of wind turbines compared to an array with more spacing.

1.2 Aim of Thesis

Multi-rotor wind turbines offer advantages as stated in the previous section. At the Western Norway University of Applied Sciences (HVL), several model-scale experiments regarding multi-rotors have been conducted in their hydrodynamic testing facility, MarinLab [21] [22] [23] [24]. These experiments yield substantial data that can be harnessed for various other applications. Building a computational model based on the physical experiments performed in MarinLab will give further insights into the flow physics of multi-rotor wind turbines.

This thesis will aim to build simulation models using computational fluid dynamics (CFD), validate them against experimental data, and use them for design optimisation of the multi-

rotor concept. The first goal of the thesis will be to build a simulation model based on SR measurements published by Sindre Øye [24] and Ingrid Neunaber [25]. Their experimental campaigns have produced experimental data that will be utilised to build a trustworthy SR simulation model. Further on, an MR model will be built based on the measurements published by Koi [21] and Skoland [23]. Both these master's theses have provided experimental data which will be used to validate the MR computational model.

After the MR computational model has been built and validated, optimisation techniques will be applied to the CFD model. A Kriging surrogate-based optimisation (SBO) technique will be applied to find the optimal inter-rotor spacing for maximum performance of the MR7 wind turbine configuration. Figure 1.2 illustrates the setup that will be investigated in this thesis. It is common to refer to the inter-rotor spacing with the single-rotor diameter as a reference, such as s/d=0.1 meaning that the distance between rotors is 10 % of the rotor diameter.

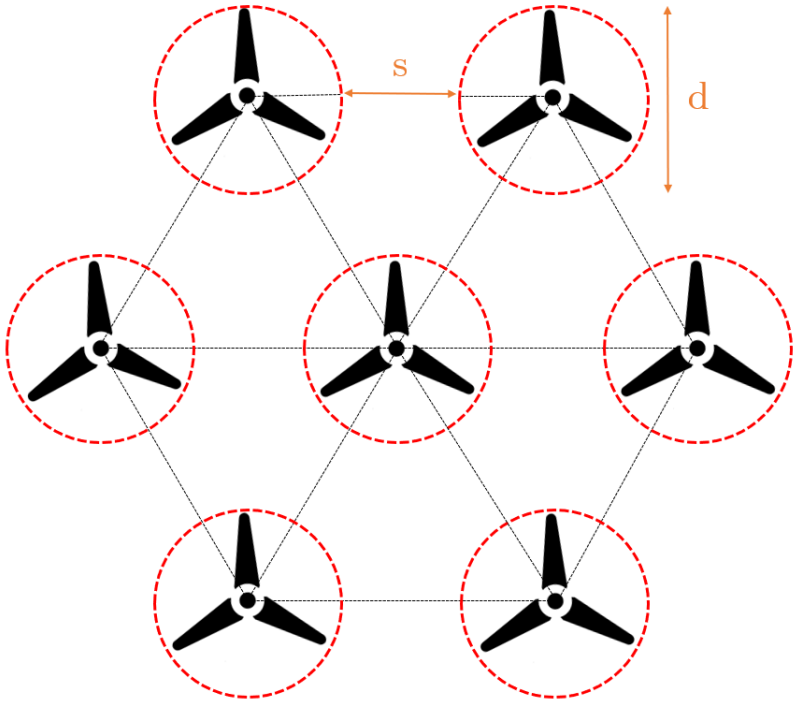

Figure 1.2: *MR7 configuration. The spacing between rotors is defined as s, while the d represents the diameter of the single rotors.*

- This page is intentionally left blank -

Chapter 2

Theory

In this chapter, an in-depth exploration of key concepts within the fields of wind energy and wind turbines will be presented. Firstly, the chapter will cover the fundamentals of wind energy, followed by a detailed review of how wind turbines harness energy from the wind to generate electrical power. Then some fundamental theories within the wind turbine world will be reviewed, before going into depth about wake flow and its generation. Results from previous experimental campaigns which will be used for validation of the simulation models will be presented, together with a literature review of porous disc and model wind turbine experiments.

2.1 Wind Turbine Aerodynamics

Within the field of wind energy, wind turbines harness the kinetic energy of air in motion, to generate mechanical energy. Subsequently, the mechanical energy is transformed into electrical energy in a generator [26]. In terms of mathematics, the kinetic energy in the wind is expressed as

$$E_k = \frac{1}{2} m U_0^2, \tag{2.1}$$

where U_0 is the free stream velocity of wind and m is the air mass. The mass flow rate of the passing wind $\dot{m}$ through a wind turbine rotor, is given by

$$\dot{m} = \rho A_r U_0, \tag{2.2}$$

in which A_r is the swept area of the wind turbine rotor and ρ is the density of the air [26]. Rotor swept area is defined by,

$$A_r = \pi r^2 \tag{2.3}$$

where the r is the radius of the wind turbine rotor.

Rotor blades are built up of different types of airfoils. An airfoil is a structure designed to alter the flow of a fluid to produce a reaction, in this case, aerodynamic lift [27]. Figure 2.1 illustrates an airfoil along with some important parameters.

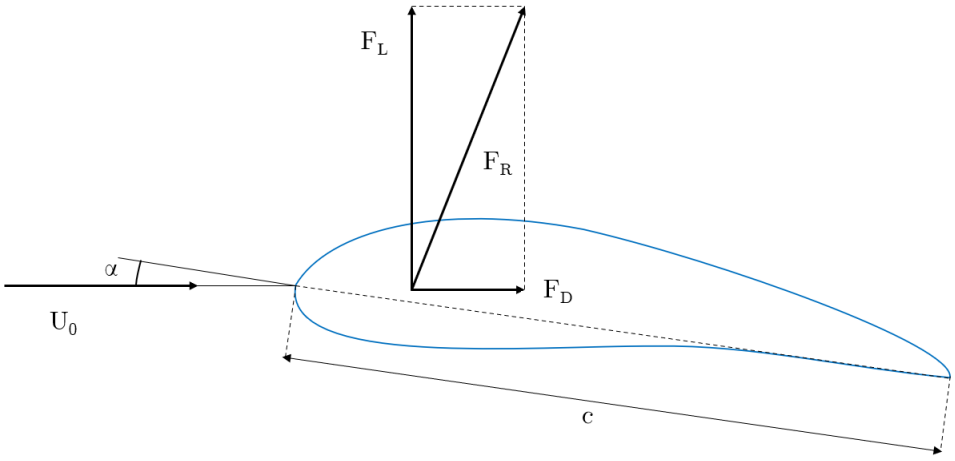

Figure 2.1: *When an airfoil is hit by the incoming wind, U_0, the forces acting on it include lift force, F_L and drag force, F_L. The angle between the incoming wind and the chord line, c, is known as the angle of attack, α. F_R is the resultant aerodynamic force of F_L and F_D.*

Lift force always acts perpendicular to the incoming wind. Lift force is generated through pressure differences over the airfoil which occurs when wind forces act on the airfoil. A high-pressure and a low-pressure side is created. Because of the atmospheric pressure, p_0 far away from the airfoil, there must be a pressure lower than p_0 on the upper side of the airfoil, the low-pressure side, and a pressure higher than p_0 on the high-pressure side. This pressure difference is what generates a lifting force on the airfoil [26]. Lift and drag force are the perpendicular and parallel components to U_0 of the resultant aerodynamic force.

An important parameter when discussing fluid flow is the Reynolds number, *Re*. The Reynolds number is the ratio of internal forces to viscous forces in the fluid and is expressed as

$$Re = \frac{u_{avg}L}{\nu} = \frac{\rho u_{avg}L}{\mu} \tag{2.4}$$

where u_{avg} is the average velocity of the flow, L is the characteristic length of the geometry, i.e. the diameter for internal pipe flows, μ is the dynamic viscosity and ν is the kinematic viscosity of the fluid ($\nu = \rho/\mu$) [28]. When the Reynolds number gets sufficiently high, such that the inertial forces are sufficiently larger than the viscous forces, the viscous forces can not prevent the random and rapid fluctuations of the fluid, and the flow becomes turbulent. When the viscous forces are large enough to suppress these fluctuations, the fluid is kept in line, i.e. the flow is laminar [28]. An illustration of laminar and turbulent flow is shown in Figure 2.2.

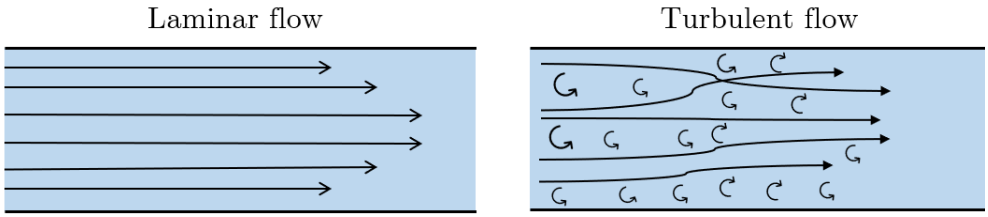

Figure 2.2: *Laminar and turbulent flow. The laminar flow remains stable, and the fluctuations of the fluid are kept in line. The turbulent flow is unstable, with random and rapid fluctuations of the fluid.*

2.2 One-Dimensional Momentum Theory

In the one-dimensional momentum theory, the rotor is regarded as an ideal actuator disc, and the theory is based on some simple assumptions [26]:

- The rotor (actuator disc) is permeable and non-rotating.
- The flow around the rotor is frictionless, stationary and incompressible.

From Figure 2.3 it can be seen how the pressure and velocity in the wake, u_w, of the actuator disc is affected. Wake flow will be further explained in Section 2.4.

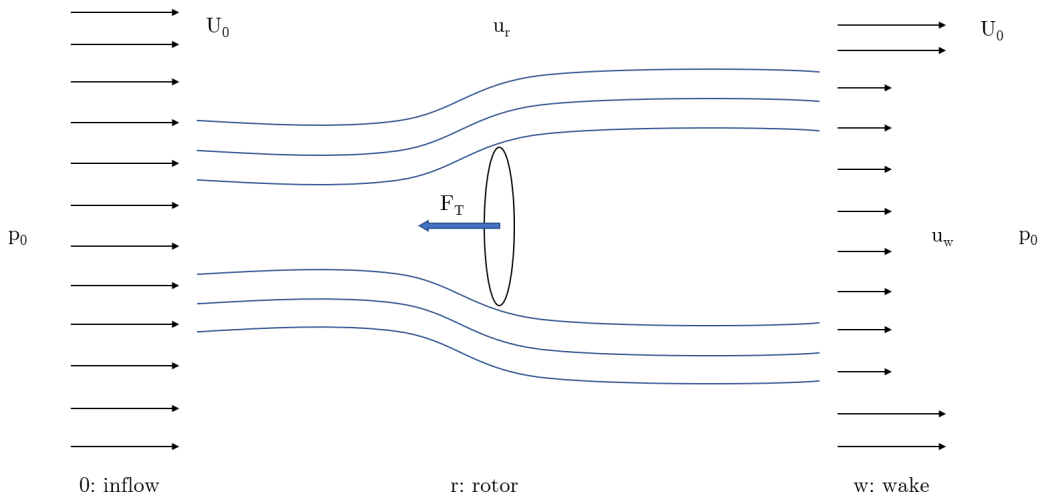

Figure 2.3: *Streamlines indicating how the actuator disc affects the pressure and velocity of the wind. The streamlines expand as they interact with the rotor, and their behaviour is determined by the thrust coefficient.*

The thrust force, F_T, can be seen acting towards the incoming wind from the rotor and slowing down the wind as it moves towards the rotor plane. The thrust force is created by the pressure drop over the rotor [26]. Figure 2.4 illustrates how the pressure and velocity change as the wind passes the rotor plane.

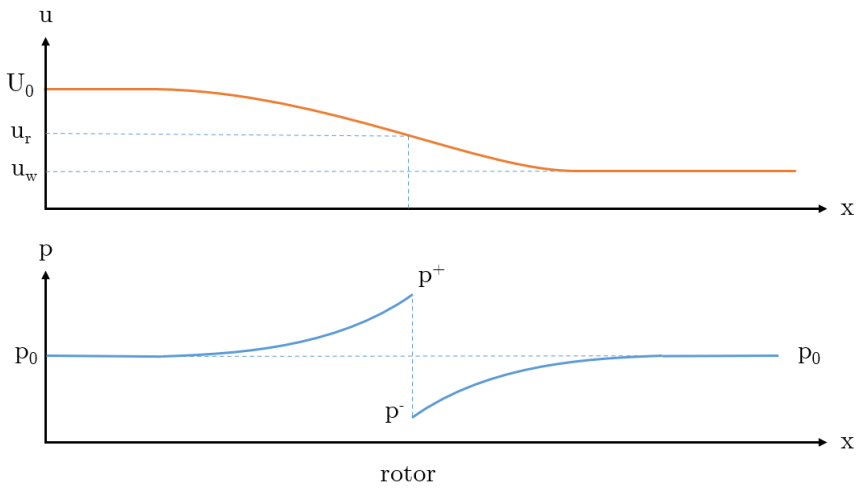

Figure 2.4: *Velocity and pressure drop over an actuator disc. Regarding velocity, it is evident that the velocity is slowed down in front of the rotor, and the velocity downstream is lower than upstream. The pressure illustration demonstrates how the pressure increases in front of the rotor, before suddenly dropping below the initial value behind the rotor, before stabilising further downstream.*

Given the assumptions in the one-dimensional momentum theory, with stationary, incompressible and frictionless flow, and that no external forces are present, Bernoulli's equation

can be used to calculate the pressure drop over the rotor.

$$\Delta p_r = p_r^+ - p_r^- = \frac{1}{2}\rho(U_0^2 - u_w^2) \tag{2.5}$$

By using the conservation of mass flow, the velocity in the rotor plane can be found [26],

$$A_0 U_0 \rho = A_r u_r \rho = A_w u_w \rho \tag{2.6}$$

where A and u are the respective areas and velocities far upstream, in the rotor plane and in the wake. The velocities in the rotor plane and wake can be expressed as,

$$u_r = (1-a)U_0 \tag{2.7}$$

$$u_w = (1-2a)U_0 \tag{2.8}$$

where a is the axial induction factor. The axial induction factor determines the reduction of velocity over the rotor plane [26]. The thrust force, as can be seen in Figure 2.3 is given by [26],

$$F_T = \Delta p A_r = \frac{1}{2}\rho A_r(U_0^2 - u_w^2) = \frac{1}{2}\rho A_r U_0^2(4a(1-a)) \tag{2.9}$$

but can also be expressed with the thrust coefficient, C_T,

$$F_T = \frac{1}{2}\rho A_r U_0^2 C_T \tag{2.10}$$

and C_T can be expressed as both

$$C_T = \frac{F_T}{\frac{1}{2}\rho A_r U_0^2} \tag{2.11}$$

and

$$C_T = 4a(1-a). \tag{2.12}$$

The power output, P, is obtained by multiplying the thrust force (Eq. 2.10) with the velocity in the rotor plane (Eq. 2.7)

$$P = F_T u_r = \frac{1}{2}\rho A_r U_0^2 C_T(1-a)U_0 = \frac{1}{2}\rho A_r U_0^3 C_P \tag{2.13}$$

with C_P being the power coefficient. The power coefficient is described as

$$C_P = \frac{P}{\frac{1}{2}\rho A_r U_0^3} \tag{2.14}$$

and

$$C_P = 4a(1-a)^2. \tag{2.15}$$

Deriving Equation 2.15 with respect to a gives:

$$\frac{dC_P}{da} = 4(1-a)(1-3a). \tag{2.16}$$

Based on Equation 2.16, C_P has its maximum value at 16/27 when the axial induction factor is equal to 1/3. The maximum value of 16/27 is equal to 0.593 which is known as the Betz limit [26]. This limit states that no wind turbine can extract more than 59.3 % of the kinetic energy available in the wind. The changes in thrust- and power coefficients with the axial induction factor can be seen in Figure 2.5.

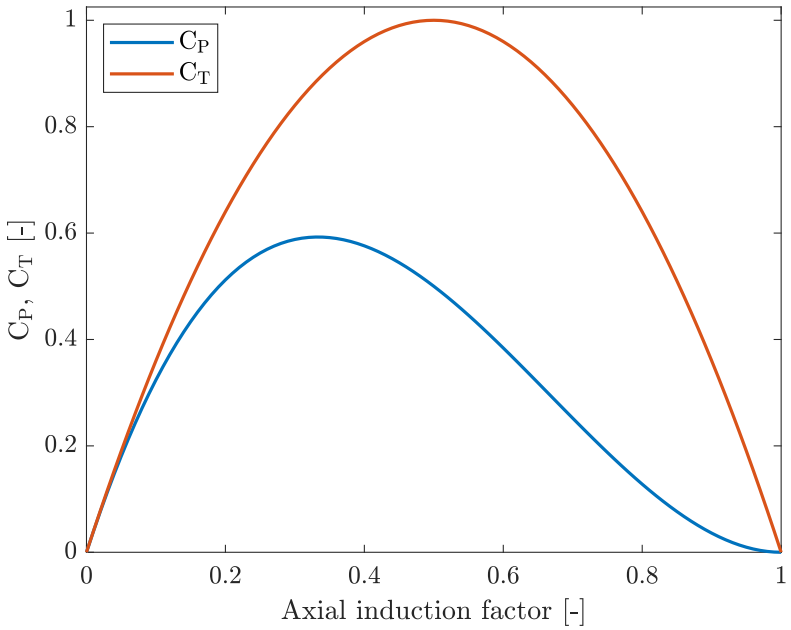

Figure 2.5: *Changes in thrust- and power coefficient with increasing axial induction factor. Studying the C_P curve, it can be seen that it never exceeds the Betz' limit of 0.593.*

It can be seen that the maximum value of the C_P curve occurs at an axial induction factor of 0.33, as stated earlier. Experiments have revealed that the assumptions underlying the ideal wind turbine, which result in the equation $C_T = 4a(1-a)$, hold true only for axial induction factors of less than approximately 0.4 [26].

Tip speed ratio λ, describes the realtionship between the rotational and natural wind velocities at the blade tip U_0, and is given by

$$\lambda = \frac{\omega r}{U_0} \tag{2.17}$$

where ω is the tangential velocity and r is the rotor radius. The tip speed ratio is one of the most important parameters concerning turbine performance as can be seen in Figure 2.6, where the relationship between the power coefficient and tip speed ratio is shown for the ForWind model wind turbine.

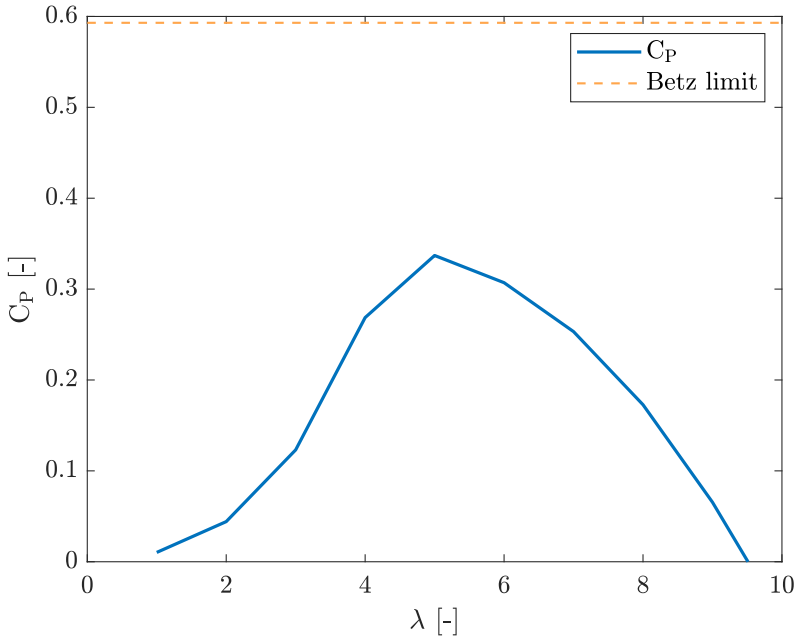

Figure 2.6: *$C_P - \lambda$ curve for the ForWind model wind turbine. Data retrieved from blade element momentum (BEM) calculations in QBlade. The figure illustrates that operating at the proper tip speed ratio can make a difference in the power output delivered by the wind turbine.*

Betz' limit can be seen as the dashed orange line in Figure 2.6 and represents the maximum amount of energy a wind turbine can extract from the wind. From Figure 2.6 it is shown that power coefficients up to 0.33 can be reached if the rotational speed of the turbine is well chosen in relation to the incoming wind speed for the ForWind model wind turbine.

If an ideal rotor is depicted, there is no rotation in the wake, i.e. the tangential induction factor *a'* is equal to zero [26]. However, for modern wind turbines wake rotation will always be included. For a rotating wind turbine rotor, the flow behind the rotor rotates in the opposite direction to the rotor, in reaction to the torque exerted by the flow on the rotor [29]. High torque will result in extra kinetic energy in the wake, i.e. a stronger wake which will take a

longer downstream distance to recover. The induced rotational velocity in the wake can be expressed as [26]

$$C_\theta = 2a'\omega r \tag{2.18}$$

where ω is the tangential velocity. An illustration can be seen in Figure 2.7.

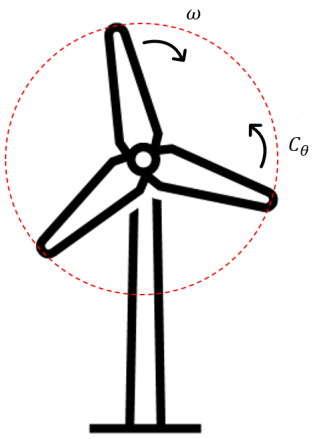

Figure 2.7: *Induced rotational velocity. The tangential velocity creates rotation in the same direction as the rotor blades are rotating, while the induced rotational velocity creates rotation in the wake the opposite way.*

The equation for power including the effects of rotation can be written as

$$P = \int_{R=0}^{r} 4\pi R^3 \rho a'(1-a) U_0 \omega^2 dR. \tag{2.19}$$

The power coefficient can be expressed as

$$C_P = \frac{8}{\lambda^2} \int_{\xi=0}^{\lambda} \xi^3 a'(1-a) d\xi \tag{2.20}$$

where ξ is the local rotational speed at the radius R non-dimensionalised with respect to the incoming wind speed U_0 [26].

2.3 Blade Element Momentum Theory

The one-dimensional momentum theory does not take the geometry of the rotor into account, i.e. which airfoils are used, number of blades and the chord/twist distribution. The rotor geometry is included in the blade element momentum (BEM) method by coupling the one-dimensional momentum theory with local forces acting on the rotor blades. The stream tube depicted in Figure 2.3 is discretised into N annular elements of height dr, as shown in Figure 2.8. For each blade element, the induced velocities $U_0(1-\alpha)$ and $\omega r a'$ are calculated from the one-dimensional momentum theory. Next, the tangential and normal forces are calculated for each element. Integration of the tangential and normal forces across the span of the blade gives the power and thrust of the rotor [26].

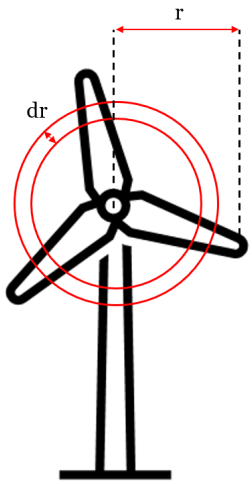

Figure 2.8: *Annular elements on rotor used in blade element momentum theory. For each blade element, dr, the induced velocities and forces are calculated. These elements are integrated across the span of the blade, r, to give the power and thrust of the rotor. Inspired by Figure 1 in [30]*

The BEM method assumes that there is no radial dependency on the annular elements, i.e. that what's happening on one radial element is not felt by the others. It also assumes that the force from the blades on the flow is constant for each annular element. The velocities at the rotor plane and the local loads on the blade can be seen in Figure 2.9.

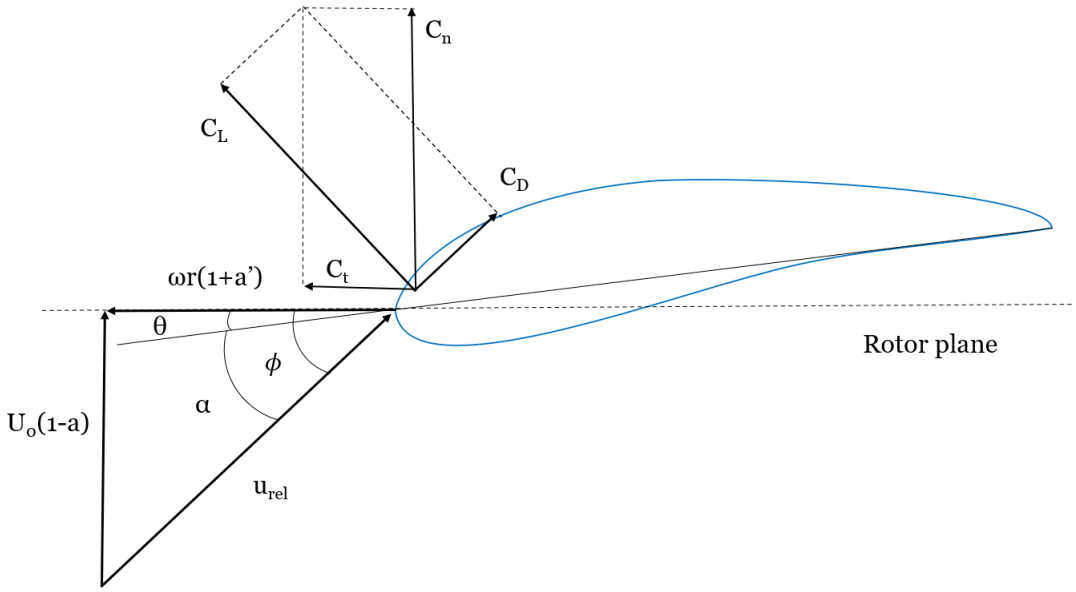

Figure 2.9: *Velocities at rotor plane and local loads on blade. Inspired by Figures 6.2 and 6.3 in [26].*

In Figure 2.9, θ is the local pitch angle of the blade, the angle between the rotor plane and the chord. ϕ is the flow angle, the angle between the rotor plane and the relative velocity, u_{rel}. It can also be seen that the angle of attack α is the difference between the flow angle ϕ and the pitch angle θ. The relative velocity is described as a combination of the axial velocity $U_0(1-a)$ and the tangential velocity $\omega r(1+a')$. C_D and C_L are the coefficients of the drag and lift force respectively, while C_n and C_t are the normal and tangential coefficients, and are given by

$$C_n = C_L \cos\phi + C_D \sin\phi \tag{2.21}$$

and

$$C_t = C_L \sin\phi - C_D \cos\phi. \tag{2.22}$$

The BEM algorithm can be summarised into eight steps [26]:

1. Initialise a and a' (typical 0 for both)
2. Calculate the flow angle ϕ
3. Calculate the local angle of attack α
4. Read lift- and drag coefficients from the table for the specific airfoil
5. Calculate normal- and tangential coefficients C_n and C_t

6. Calculate a and a'
7. If a and a' have changed more than a preset tolerance, go back to step 2, or else finish
8. Calculate local loads on blade element.

Two corrections are needed to the algorithm to get good results. Prandtl's tip loss factor corrects the assumption of an infinite number of blades [26]. The vortex system in the wake is different for a rotor with an infinite number of blades versus a finite number of blades. Prandtl's correction factor F is computed by

$$F = \frac{2}{\pi}\cos^{-1}(e^{-f}) \tag{2.23}$$

with f being

$$f = \frac{B}{2}\frac{r-R}{R\sin\phi} \tag{2.24}$$

and B is the number of blades, R is the variable radius and r is the total rotor radius.
The other correction is the Glauert correction. It corrects for the fact that the simple momentum theory breaks down when the axial induction factor becomes larger than approximately 0.4 [26]. As seen in Figure 2.10 the C_T curve from the simple momentum theory goes to zero for an axial induction factor of 1.0, when in reality measured data indicate that thrust coefficients increase up to about 2.0 at an axial induction factor of 1.0 [29].

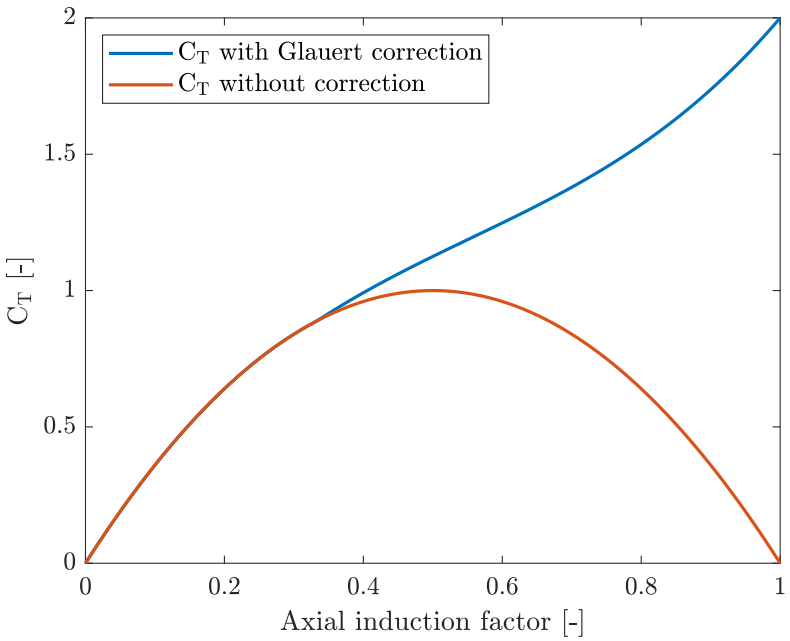

Figure 2.10: *Glauert correction for large induction factors. It can be seen that a clear distinction is present when the axial induction factor exceeds 0.4.*

2.4 Wake Flow

A wind turbine wake is the region downstream of the wind turbine where the airflow is disrupted and slowed down by the presence of the rotor blades of the turbine. As the turbine blades extract kinetic energy from the wind, it causes a drop in wind speed as described in Section 2.2. In large offshore wind farms, wind turbine wakes are the reason for an average power loss of 10-20 % of total power output [31]. The wake can be divided into different regions, that being the near wake and the far wake [32]. Near wake is typically the region < 1-2 diameters downstream of the wind turbine, and far wake is the region > 3-4 diameters. An illustration of this can be seen in Figure 2.11.

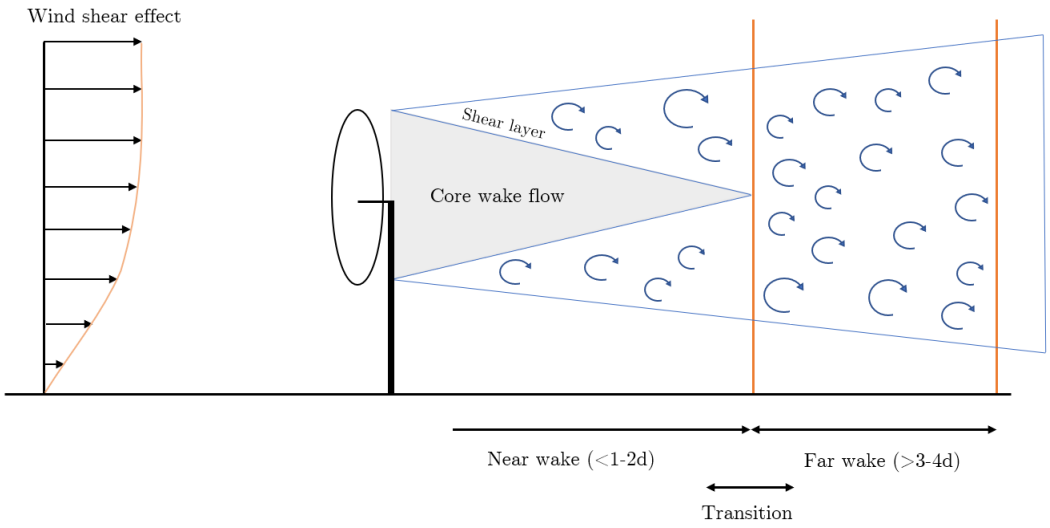

Figure 2.11: *Regions of a wake flow. Inspired by Figure 1 in [33].*

Wind turbines operate in the lower part of the atmospheric boundary layer and are continuously affected by the underlying surface and the corresponding exchange processes of energy and matter [34]. Abkar and Porté-Agel [35] did LES studies on how the wake is affected by atmospheric stability. It was concluded that atmospheric thermal stability plays a significant role on the spatial distribution of the mean velocity deficit, turbulence intensity and turbulent shear stresses. The unstable atmosphere condition led to faster wake recovery compared to stable and neutral conditions. This was likely caused by more turbulence in the incoming wind, leading to a higher turbulent entrainment flux into the wake.

Wind shear describes the increase in average wind speed with height above the surface

and depends mainly on surface roughness. A simple power law is often used to quantify the effect,

$$\frac{u}{u_0} = (\frac{h}{h_0})^{\alpha} \tag{2.25}$$

where u is the wind velocity at height h, u_0 is the velocity of the wind at height h_0 and α is the power law exponent that depends on the roughness of the surface [36].

In the near wake, the shape of the wake is influenced by pressure equalisation between the air immediately behind the rotor and the vortex wakes created by the airflow around the rotor blades [37]. As the wake transitions further downstream, turbulence is generated, mingling with the surrounding free stream airflow. Moving away from the wind turbine, the tip vortices generated by the rotor blades eventually dissipate into turbulence. Turbulence represents irregular fluid motion resulting from cross-flow movements and vortices of various scales.

As a result of wake flows, the downstream turbines experience lower inflow velocity compared to the upstream one, because of energy extraction from the upstream wind turbine. Wind turbines should therefore be spaced as far apart as possible in the prevailing wind direction. However, area allocations and connecting turbines to the grid force the spacing to be closer [6]. Some known wind farms have turbine spacings between 5 and 10 diameters, like the Horns Rev (7d) [38], Nysted (5.8d north-south, 10.5d east-west) [39] and Rødsand II (5-10d) [40]. Optimisation of wind farm layouts has become an important parameter within wind energy, to ensure that the wind farm is performing as efficient as possible.

At Horns Rev, located 14 km west of Denmark, the effects of wind speed, wind turbine spacing, turbulence intensity and stability conditions when it comes to power deficit because of wind turbine wakes have been analysed by Hansen et al. [41]. It was shown that stable atmospheric conditions led to an average low turbulence intensity of 4 %. As the atmospheric conditions become more unstable, the turbulence levels tend to increase. The lowest turbulence intensities were experienced between 8-12 m/s when wake losses were high because of the relatively high thrust coefficient. The analysis showed that the maximum power deficit decreased with increasing wind speed. Between the first and second wind turbines, the largest power deficit was experienced, while the remaining power deficit downstream was small.

2.5 Experimental Campaigns for Validation

Numerous physical experiments on single-rotor (SR) and multi-rotor (MR) wind turbine configurations have been performed using actuator discs and model wind turbines. In MarinLab, a hydrodynamic testing facility located at the Western Norway University of Applied Sciences in Bergen, actuator disc experiments have been conducted [21] [23] [24] [42]. Actuator discs are simplifications of rotating blades on a horizontal-axis wind turbine (HAWT) and are used in both experiments and simulations. Actuator discs are easier and cheaper to manufacture per mass, and often more robust than rotating parts [43]. Experiments with actuator discs have also been performed by Kurelek et al. [44], Ranjbar et al. [45], Öztürk et al. [46] and Lignarolo et al. [47] [48]. The ForWind model wind turbine (MWT) has been experimented on by Neunaber [25], Hulsman et al. [49] and Schottler et al. [50], in wind tunnels located at the University of Oldenburg and the Norwegian University of Science and Technology (NTNU). All of these experimental campaigns yield substantial data that will be used to validate the numerical models.

2.5.1 Single-Rotor Actuator Disc Experiments

In 2022, Øye [24] did an experimental study of the wake flow and thrust coefficient of porous actuator discs. He performed experiments on force measurements and velocity profiles for a porous disc with a diameter of 200 mm and a solidity of 57 %. Solidity is expressed as

$$\sigma = 1 - \Phi \tag{2.26}$$

where Φ is porosity, given by

$$\Phi = \frac{A_{open}}{A_{closed}} \tag{2.27}$$

describing the ratio between the open and total area of the disc. The disc has varying solidity from disc centre to disc edge, as shown in Figure 2.12.

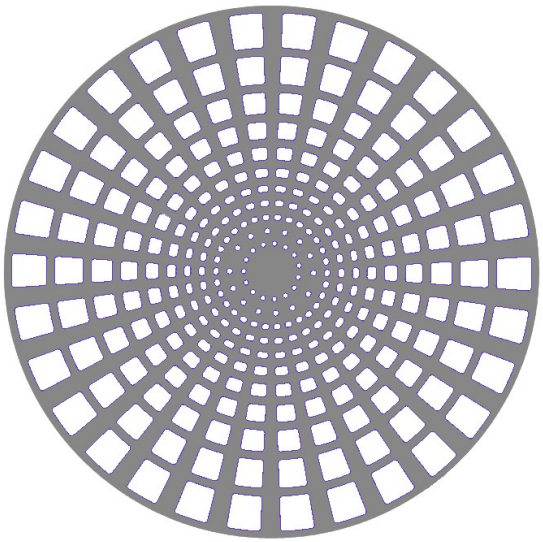

Figure 2.12: *Porous actuator disc used in the experimental campaign by Øye [24]. The disc has a diameter of 200 mm, a thickness of 5 mm and is made of aluminium.*

Wake measurements from Øye [24] are shown in Figure 2.13.

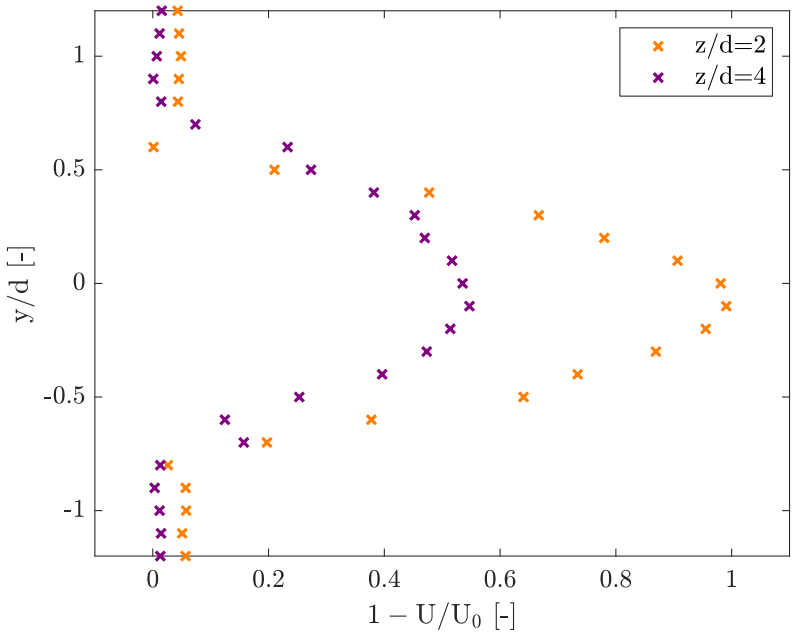

Figure 2.13: *Normalised velocity profiles obtained from experimental data by Øye [24], d equals the porous disc diameter, the y-axis lies in the plane of the rotor, the z-axis is oriented in the downstream direction, U is the measured velocity and U_0 is the inlet velocity.*

Figure 2.13 demonstrates how the velocity in the wake changes as the flow propagates downstream. At z/d=2, the velocity deficit is at its maximum right behind the centre of the disc, where the velocity is approximately equal to zero. In the wake at a downstream distance of z/d=4, the velocity in the wake recovers, where the velocity behind the disc is approximately

half of the free stream velocity.

Three criteria for a new design methodology for porous disc wind turbine modelling were presented by Kurelek et al. in [44]. By matching a porous disc to a HAWT on (i) thrust coefficient, (ii) radial solidity distribution and (iii) length scale, a well-performing model is obtained, which is not dependent on free stream turbulence intensity and does not require iterative tuning. Three different porous discs were designed, all with different design parameters. The discs were also compared against a wind turbine model, with a diameter of 200 mm and a solidity of 18.2 %, designed by Miller et al. [51]. The discs used in the experiment with their design parameters can be seen in Table 2.1.

Table 2.1: *Porous disc designs in Kurelek et al.[44]*

Porous disc	**Design parameters**
UD	(i) Thrust coefficient, (iii) length scale
ND1	(i) Thrust coefficient, (ii) radial solidity distribution
ND2	(i) Thrust coefficient, (ii) radial solidity distribution, (iii) length scale

The uniform disc (UD) and non-uniform disc 1 (ND1) were designed to lack a specific feature intentionally, to see how it affected the wake. It was discovered that the effect of radial solidity distribution greatly affects the mean velocity in the wake. The wake behind the UD porous disc creates a 'top-hat' mean velocity profile, with a flat velocity deficit between disc edges. The UD velocity deficit was also discovered to recover much slower compared to the rotor. Results showed that matching the thrust coefficient is insufficient for porous disc design. The comparison of UD against ND1 and non-uniform disc 2 (ND2) made it clear that radial solidity distribution matching the rotor is the clear choice for porous disc design. It was clear that both the ND1 and ND2 outperformed the UD, but differences occurred also between ND1 and ND2, especially in the far wake, where the ND1 has a faster wake recovery, much due to larger openings which create more turbulent kinetic energy which dominates the wake and its recovery. The study concluded that incorporating all three design parameters yields a model that performs well at high Reynolds numbers and low free stream turbulence intensities.

How the solidity impacts wind turbine parameters such as axial induction factor, thrust coefficient and power coefficient were investigated by Ranjbar et al. [45]. In their study, solidities ranging from 0.2 to 0.6 (20 % to 60 %) were tested both experimentally and numerically.

Based on more than 200 experiments and numerical simulations along with momentum theory, they were able to extract the following equations for power- and thrust coefficient:

$$C_P = \frac{64}{27}\sigma(1-\sigma) \tag{2.28}$$

$$C_T = \frac{64}{9}\frac{\sigma(1-\sigma)}{3-2\sigma}. \tag{2.29}$$

The above equations are only valid for a solidity range of $0.2 < \sigma < 0.6$. The mean errors between the extracted equations and experimental results were 1.59 % and 2.82 % for C_P and C_T respectively. Results from the study also showed that porous discs with a solidity of 0.5 reach the Betz limit of 0.593.

Effects of free stream turbulence on the wake growth rate of a model wind turbine (MWT) and a porous disc (PD) were investigated by Öztürk et al. [46]. The porous disc and model wind turbine tested had a diameter of 120 mm and matching thrust coefficients. The disc porosity was non-uniform, similar to the porous disc used in MarinLab experiments [21] [23] [24] [42]. A turbulence grid was placed 6 m upstream of the MWT/PD to generate turbulence. Experiments were run both with and without the grid. Experiments without the grid, i.e. with ambient turbulence (0.5 %) showed a faster wake recovery for the PD in the immediate near wake ($0.5 \leq d \leq 1.5$), probably because of the PD acting as a passive grid and adding turbulence to the wake. Further downstream ($d \geq 3$), it was observed that the wake velocity deficit decreased faster for the MWT than the PD. With added turbulence from the grid, the wake was recovering faster for both PD and MWT, as expected with higher turbulence intensity levels. In the near wake, the PD showed a faster wake recovery, the same as with no added turbulence from the grid.

While Öztürk et al. looked at the wake growth, Lignarolo et al. investigated turbulent mixing in the wake for wind turbines and actuator discs [47] and a comparison of the near wake for the two [48]. In [47] and [48] a two-bladed wind turbine with a diameter of 0.6 m was compared against a porous disc with the same diameter. The thrust coefficients was 0.93, and the disc had a solidity of 32 %. A free-stream turbulence intensity of 0.5 % was applied for both experiments. It was shown that the two models matched in both wake expansion and energy extraction, within 4 % [48] (within 3 % in [47]). In the near wake shear layer, similar

values for mean kinetic energy flux were obtained, despite the turbulence intensity in the wind turbines near wake being four times larger than in the wake of the porous disc.

2.5.2 Single-Rotor Model Wind Turbine Experiments

A study on wake flow and how turbulence influences wake formation was performed by Neunaber [25]. Wind tunnel experiments were carried out using an actuator disc and the ForWind model wind turbine (MWT) exposed to different turbulent inflows to examine the influence of turbulence on the wake's development. The ForWind MWT is presented in Figure 2.14.

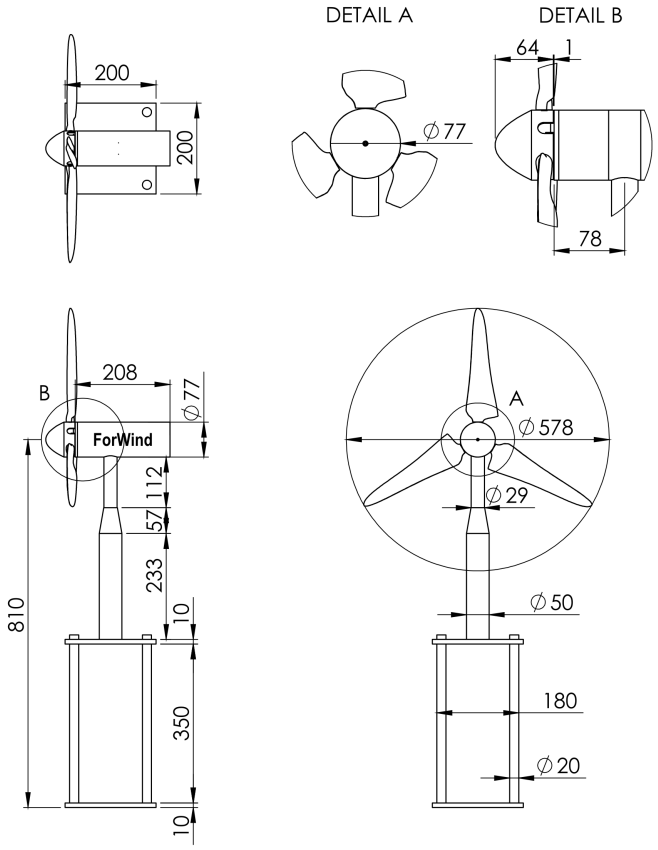

Figure 2.14: *ForWind model wind turbine, dimensions in mm. Retrieved from Sætran et al. [52]*

The turbine blades consist of the SD7003 airfoil. The airfoil is designed for operation at low Reynolds numbers [53]. The measured airfoil polars for the SD7003-085-88 airfoil can be located in Selig et al. [53] and the airfoil profile is shown in Figure 2.15.

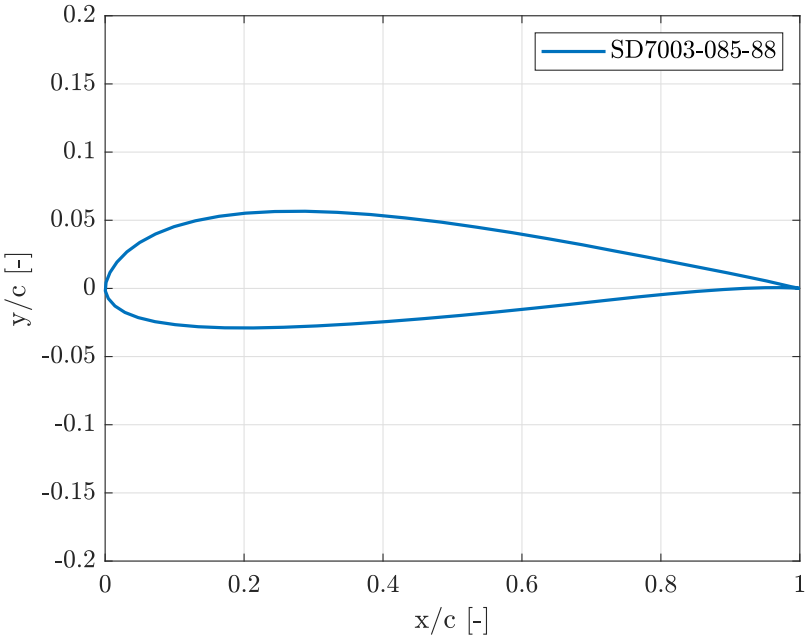

Figure 2.15: *SD7003 airfoil coordinates*

The thrust- and power coefficient curves for the ForWind MWT are shown in Figure 2.16

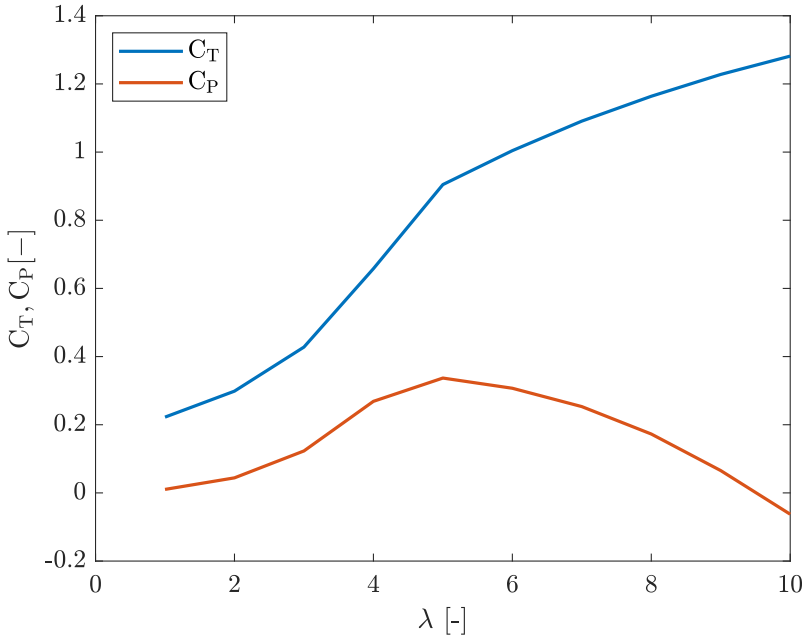

Figure 2.16: *$C_T - \lambda$ and $C_P - \lambda$ curve for the ForWind model wind turbine*

The measurements were taken using hot-wire anemometry. Table 2.2 presents the different inflow conditions.

Table 2.2: *Inflow conditions in Neunaber [25]*

Inflow condition	Characteristics
Laminar	Free flow, no grid
Uniform turbulent inflow	Regular grid inflow
Turbulent inflow	Active grid

Data from wake measurements were retrieved in the near wake (1d-4d) for the laminar inflow condition is shown in Figure 2.17.

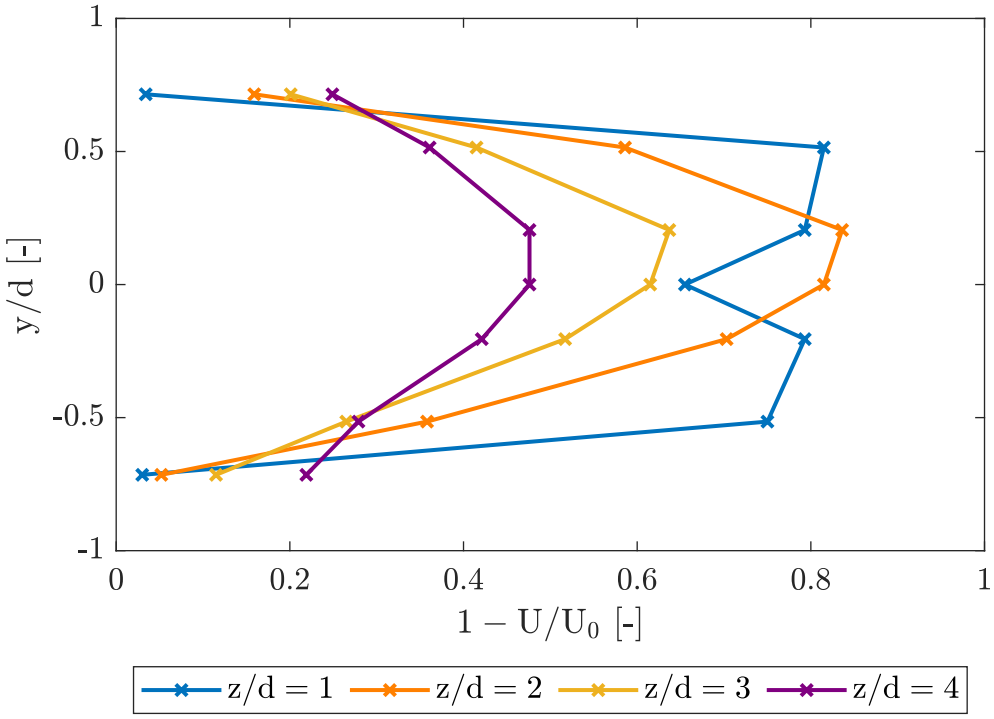

Figure 2.17: *Normalised velocity profiles measured for the ForWind model wind turbine retrieved from [25] for four different downstream distances (z), where d equals the rotor diameter of 0.578 m.*

Results from Neunaber [25] indicated that the mean flow fields of both models evolve similarly. Regarding wake generation, the comparison between actuator disc wake and turbine wake was in agreement with [47] and [48]. The study also found that the influence of inflow on the wake was minimal, indicating that the wake develops largely independently of the inflow. The actuator disc was deemed suitable for far wake studies, as all the quantities behave similarly. In the direction of the inflow, the turbine's wake exhibited sensitivity within a specific area, whereas the turbine disc remained almost unaffected.

While Neunaber performed hot-wire anemometry in her measurements on the ForWind

model turbine, Hulsman et al. [49] used the Lidar WindScanner to investigate wake development. Similar to Neunaber [25], measurements were performed in the wind tunnel at the University of Oldenburg. Measurements were taken with an inflow speed of 7.5 m/s with different inflow conditions, using no grid or a passive grid to generate extra turbulence. For the measurements with turbulent inflow (passive grid), the tip and root vortices started breaking down at 2d while they were broken down at 4d for the inflow condition without a grid. Results were compared against Neunaber [25] and showed great comparison.

Wind tunnel experiments for investigating the wake behind the ForWind turbine have also been performed at the Norwegian University of Science and Technology (NTNU) by Schottler et al. [50]. In this study, laser Doppler anemometry was used to compare the wakes of the ForWind model turbine and the NTNU turbine, a model wind turbine with a larger diameter (0.894 m vs 0.580 m) and a higher blockage (13 % vs 5.4 %) than the ForWind model turbine. The two turbines had similar thrust coefficients of 0.87 and both operated at a tip speed ratio of 6. Measurements of velocity deficit indicated a slight wake expansion, and the minimum velocity was $U/U_0 = 0.64$.

2.5.3 Multi-Rotor Actuator Disc Experiments

Koi [21] used several actuator discs of the same type (AD20) as Øye [24] when she investigated how different MR7 configurations affected the aerodynamic interaction effects of the models. Three different inter-rotor spacings, s/d=0.0, s/d=0.1 and s/d=0.4 were tested, where d equals the diameter of the actuator disc (200 mm). Results by Koi [21] indicated that less spacing between rotors leads to a higher thrust force as shown in Table 2.3.

Table 2.3: *Thrust force measurements on centre disc performed by Koi [21]*

Model	**Measured thrust force [N]**
MR7 s/d=0.0	2.59 ± 0.02
MR7 s/d=0.1	2.53 ± 0.02
MR7 s/d=0.4	2.45 ± 0.02

It can be seen that as the spacing between the discs increases, the thrust force acting on the centre disc decreases. It was also concluded that the edge discs experience lower thrust force than the centre one. Looking at the measured thrust coefficients in Table 2.4, it can be seen that the centre disc has the highest thrust coefficient.

Table 2.4: *Thrust coefficient measurements by Koi [21]*

Model	**C_T centre disc [-]**	**C_T edge disc [-]**
MR7 s/d=0.0	1.03 ± 0.01	0.94 ± 0.02*
MR7 s/d=0.1	1.005 ± 0.007	0.97 ± 0.02
MR7 s/d=0.4	0.975 ± 0.008	0.97 ± 0.02

Regarding the edge disc measurements, no clear trend was discovered due to inconsistent results for the s/d=0.0 model.

Koi [21] also did measurements in the induction zone, which showed that the individual induction zones eventually merge into one single, global induction zone. Higher velocity deficits in the induction zone for a smaller spacing were discovered as well.

Another experimental campaign in MarinLab was performed by Skoland [23]. He researched how different MR setups affected the wake flow. The results indicated that an increase in spacing between rotors leads to a decrease in velocity deficit and turbulence. The same inter-rotor spacings as in Koi [21] were used here as well. It was shown that the largest spacing led to faster wake recovery, because of initial low velocity deficit. As discovered in Koi [21], smaller spacing between rotors leads to a higher velocity deficit in the induction zone. The normalised velocity deficit measurements from Skoland [23] with an inter-rotor spacing of s/d=0.1 for an MR7 configuration can be seen in Figure 2.18, compared against the single AD20 disc.

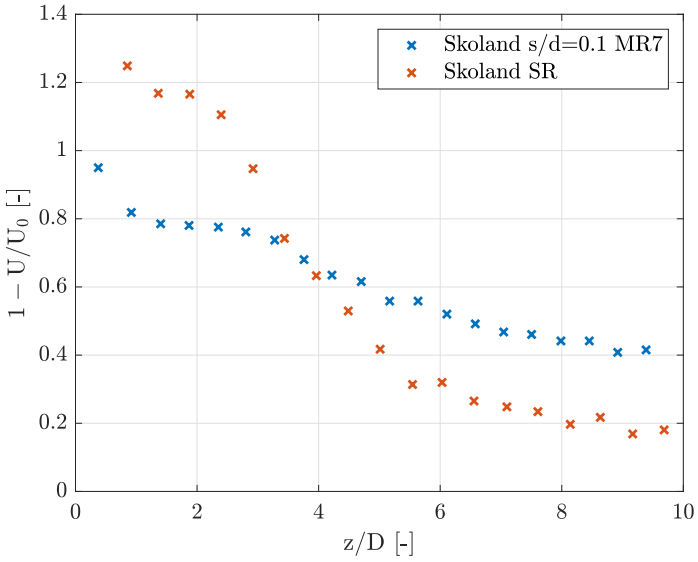

Figure 2.18: *Centerline measurements of normalised velocity deficit from Skoland [23] at different downstream locations (z/D). D equals the total diameter of the multi-rotor system with an inter-rotor spacing of s/d=0.1.*

As Figure 2.18 displays, the SR has a higher velocity deficit in the near wake, while the MR7 has a higher velocity deficit in the far wake. It can also be seen that the velocity in the wake is approximately similar at four diameters downstream. Wake measurements from Skoland [23] obtained from his experimental campaign are shown in Figure 2.19.

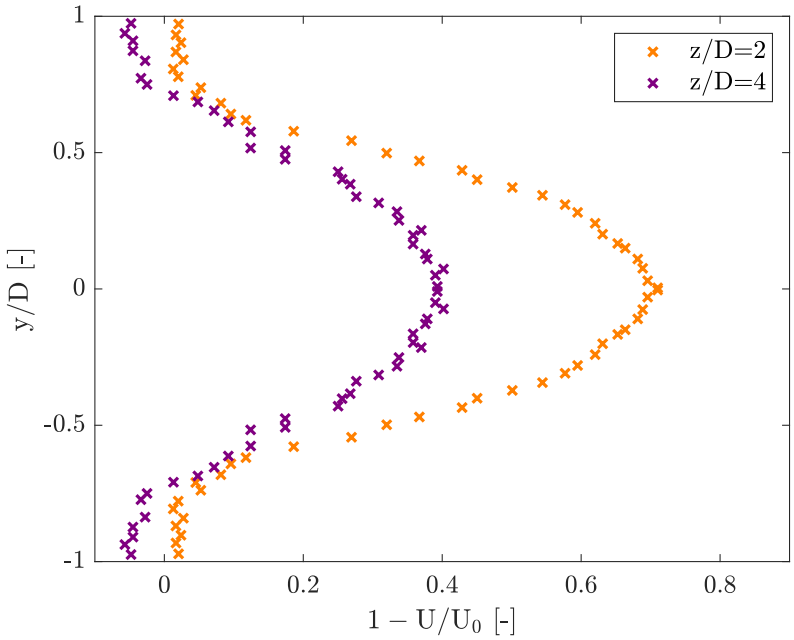

Figure 2.19: *Normalised velocity deficit profiles retrieved from experimental data obtained by Skoland [23]. In this figure, D represents the total diameter of the multi-rotor system, the y-axis lies in the plane of the rotor, the z-axis is oriented in the downstream direction, U is the measured velocity and U_0 is the inlet velocity*

Jørs and Mjåtveit [22] did measurements of MR wake flow in MarinLab, similar to Skoland [23]. They compared an MR setup consisting of four actuator discs with a spacing of s/d=0.1 (d is 200 mm), an MR setup with seven discs with a spacing of s/d=0.4, and an SR model consisting of one single actuator disc with diameter d. It was shown that both MR models had faster wake recoveries in the near wake, compared to the SR model. In the far wake, it was shown that the MR wake recovers slower, due to lower turbulence in the wake, which makes the SR wake- and the MR wake deficits similar in the far wake region. In their study, the spacing in an MR setup was also researched. It was shown that an increased spacing leads to a lower velocity deficit in the near wake and a reduction in turbulence levels.

In 2023, Eriksen [42] conducted additional research on the wake flow of various multi-rotor configurations. Eriksen investigated how local thrust variations influenced the wake recovery. To perform this, three different centre discs were used in the MR7 setup to alter the thrust force. The discs had solidities of 47 %, 57 % and 67 %. The different configurations were compared to an SR setup. It was shown that a centre turbine with greater solidity leads to higher thrust force in the upstream region and faster wake recovery because of higher shear stress, turbulent kinetic energy and cross-stream in the near wake region. Downstream of the turbine, increased thrust force and associated turbulent kinetic energy could lead to energy loss because of turbulence and vortices. Eriksen's experimental campaign showed that multi-rotors have wake recovery advantages in the near wake.

Chapter 3

Methodology

In this chapter, the methodology used in the thesis is presented. Firstly, computational fluid dynamics (CFD) will be presented, going through key concepts such as the underlying Navier-Stokes equations, boundary conditions, mesh, turbulence modelling and exploration of the accuracy of computational simulations. Furthermore, the computational solvers used in the thesis, STAR-CCM+ and QBlade, are explained. The virtual disk model within STAR-CCM+ which will be utilised for both single-rotor and multi-rotor simulations will be elaborated upon. The setup for the virtual disk will also be explained, and how it is used for simulating the behaviour of a wind turbine using both a porous disc and a model wind turbine as a reference. Different ways of modelling the thrust force distribution will be explained before the optimisation technique applied is presented. A surrogate-based optimisation technique is utilised.

3.1 Computational Fluid Dynamics

CFD is used to model the behaviour of fluids, based on the Navier-Stokes equations [28]. Running a CFD simulation is far more time-efficient than performing a physical experiment, but there are several factors which affect the results of the CFD simulation. Factors such as poorly generated mesh, improperly applied boundary conditions or flow parameters all affect the results of the simulation. CFD analyses are often run in parallel with experimental studies. Global properties like thrust force can be obtained experimentally, while CFD can give details about the flow field, pressure profiles and streamlines. Experimental data is

often used to validate CFD solutions by matching the computationally and experimentally determined global quantities. CFD is then employed to shorten the time to run through carefully controlled parametric studies [28].

3.1.1 Navier-Stokes Equations

CFD simulations are based on the Navier-Stokes equations, which are used to describe the motions of fluids. The Navier-Stokes equations for an incompressible fluid with constant viscosity μ consist of the continuity equation (Eq. 3.1) [26] given as

$$\frac{\partial u_x}{\partial x} + \frac{\partial u_y}{\partial y} + \frac{\partial u_z}{\partial z} = 0, \tag{3.1}$$

and three momentum equations (Eq. 3.2, Eq. 3.3, Eq. 3.4) [26] expressed by

$$\rho\left(\frac{\partial u_x}{\partial t} + u_x\frac{\partial u_x}{\partial x} + u_y\frac{\partial u_x}{\partial y} + u_z\frac{\partial u_x}{\partial z}\right) = -\frac{\partial p}{\partial x} + \mu\left(\frac{\partial^2 u_x}{\partial x^2} + \frac{\partial^2 u_x}{\partial y^2} + \frac{\partial^2 u_x}{\partial z^2}\right) + f_x \tag{3.2}$$

$$\rho\left(\frac{\partial u_y}{\partial t} + u_x\frac{\partial u_y}{\partial x} + u_y\frac{\partial u_y}{\partial y} + u_z\frac{\partial u_y}{\partial z}\right) = -\frac{\partial p}{\partial y} + \mu\left(\frac{\partial^2 u_y}{\partial x^2} + \frac{\partial^2 u_y}{\partial y^2} + \frac{\partial^2 u_y}{\partial z^2}\right) + f_y \tag{3.3}$$

$$\rho\left(\frac{\partial u_z}{\partial t} + u_x\frac{\partial u_z}{\partial x} + u_y\frac{\partial u_z}{\partial y} + u_z\frac{\partial u_z}{\partial z}\right) = -\frac{\partial p}{\partial z} + \mu\left(\frac{\partial^2 u_z}{\partial x^2} + \frac{\partial^2 u_z}{\partial y^2} + \frac{\partial^2 u_z}{\partial z^2}\right) + f_z \tag{3.4}$$

where u_x, u_y and u_z are the velocity components of x, y and z respectively in a cartesian frame of reference, t is time, ρ is density, p is pressure and f are the external body forces. The continuity equation (Eq. 3.1) makes sure that for an infinitesimal box with side lengths dx, dy and dz, the net mass flow in and out is equal to zero. The momentum equations (Eq. 3.2, Eq. 3.3, Eq. 3.4) are, in the x, y and z directions respectively, Newton's second law for an infinitesimal box in the fluid, which is fixed in space [26]. The left side of the momentum equations consists of inertial forces, while the right side consists of pressure forces, viscous forces and external body forces [26].

3.1.2 Boundary Conditions

Appropriate boundary conditions are required to obtain an accurate CFD solution [28]. Not only does the accuracy of the solution depend strongly on a proper physical model and

numerical treatment of the boundaries, but also the robustness and the convergence speed are considerably influenced [54]. The different boundary conditions to apply in CFD are inlet, outlet, wall and symmetry. Figure 3.1 displays some of the different boundary conditions that are applied to a computational domain.

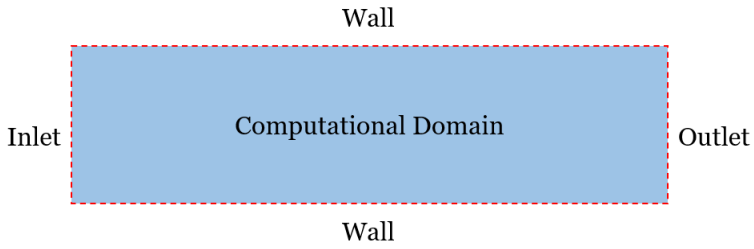

Figure 3.1: *Boundaries of the computational domain. Inspired by Figure 15-19 in [28].*

The wall boundary condition does not allow flow propagation through it and will reflect waves off itself [55]. Wall settings can be set to either "slip" or "no-slip". The no-slip condition assumes that the velocity of the fluid layer in immediate contact with the boundary matches the velocity of the boundary itself, resulting in no relative motion between them, i.e.

$$u = v = w = 0.$$

In contrast, for the slip wall boundary condition, the fluid slides along the wall without any shear forces, and does not correspond to the wall velocity [55].

Where the fluid enters the computational domain is called the inlet. The inlet is usually categorised as velocity-inlet or pressure-inlet. For a velocity inlet, the velocity is specified along the face of the inlet, while for a pressure inlet, the pressure is specified along the face of the inlet. The outlet boundary is located where the flow should be directed outwards and is usually defined as a pressure outlet. At the pressure outlet, the pressure imposes the working pressure [55].

A cylindrical fluid domain was created for the simulation. The diameter and length of the domain were set large enough to enclose all of the flow within the domain. The distance downstream needs to be sufficient to catch the wake as it propagates, and upstream to catch the induction zone properly. An illustration of the fluid domain with its boundary conditions

can be seen in Figure 3.2.

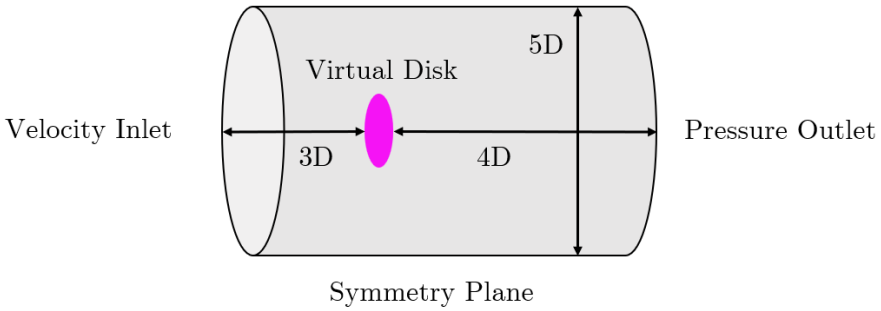

Figure 3.2: *Fluid domain for CFD simulations with boundary conditions*

The inlet boundary was set to velocity inlet, as the distribution of velocity and fluid properties are known. At the outlet, a pressure outlet was specified, with a reference pressure set at 0 Pa to ensure that no backflow occurred from the outlet, similarly performed in Acker [56]. A symmetry plane boundary was set at the sides of the simulation domain, as with this setting there is minimum interaction with the flow [56]. The same domain and boundary conditions were applied to the multi-rotor simulations as well, scaled according to the total diameter of the multi-rotor system, as seen in Figure 3.3.

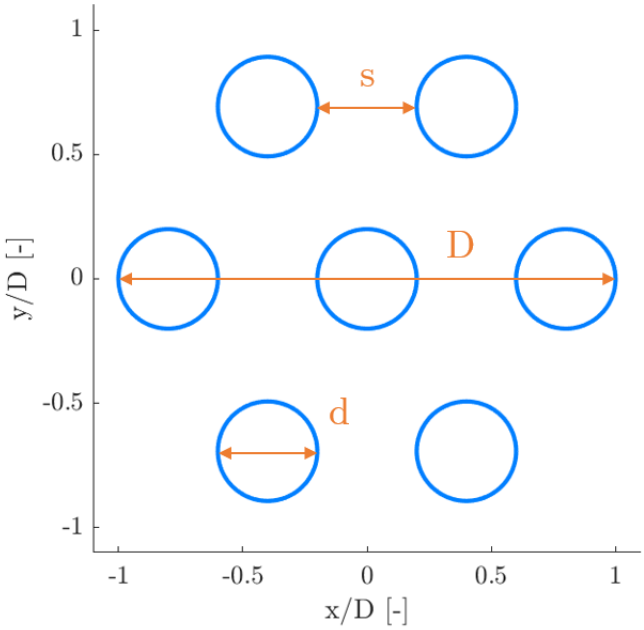

Figure 3.3: *Layout for MR setup, shown for s/d=1.0. Capital D represents the diameter of the whole MR system, lowercase d is the individual rotor diameters, while s refers to the spacing between rotors.*

3.1.3 Mesh

A mesh is a discretised representation of a geometric domain into a grid. Mesh cells are also called grid cells. A two-dimensional mesh is often built of triangles and/or quadrilaterals. In a three-dimensional grid, the cells are made of tetrahedra, hexahedra, prisms, or pyramids. Different types of grid cells can be seen in Figure 3.4. The primary requirement for grid generation is to ensure that there are no gaps between the grid cells and make sure they are not overlapping. Another important parameter is that the mesh should be smooth, with no sudden changes in the volume of cells or the stretching of the cells. If these things are not considered, numerical errors are likely to occur in the simulations [54].

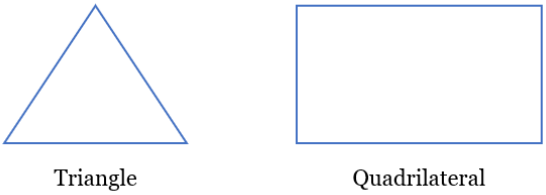

(a) *Two-dimensional grid cells*

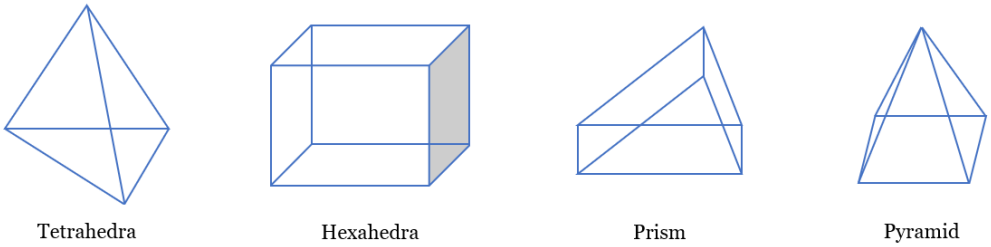

(b) *Three-dimensional grid cells*

Figure 3.4: *Grid cells*

A base mesh size of 0.1 m was set initially for the entire domain. This mesh size is relatively large compared to the area of interest, but for computational efficiency, it was chosen a large mesh outside the area of interest. Custom meshes were created around the areas of interest, one of them being the virtual disk, to accurately capture all the effects of the flow around the rotor. Another custom mesh was created in the wake, to capture all the flow characteristics going on downstream of the disk. The MR wake mesh was also stretched far upstream to catch the rotor interaction effect in the induction zone, as seen in Figure 3.7. Which mesh sizes were used for which simulations is shown in Table 3.1.

Table 3.1: *Mesh properties in different simulations*

Simulation	Virtual disk mesh size	Wake mesh size	Grid cells
SR using porous disc	5 mm	40 mm	~ 400 000
SR using model wind turbine	6 mm	20 mm	~ 1 500 000
MR using model wind turbine	6 mm	20 mm	~ 12 000 000

As the simulations with the porous disc were run with adaptive meshing, the number of grid cells presented in Table 3.1 show the number of cells before running the simulation. The meshing around the virtual disk for the simulations can be seen in Figure 3.5.

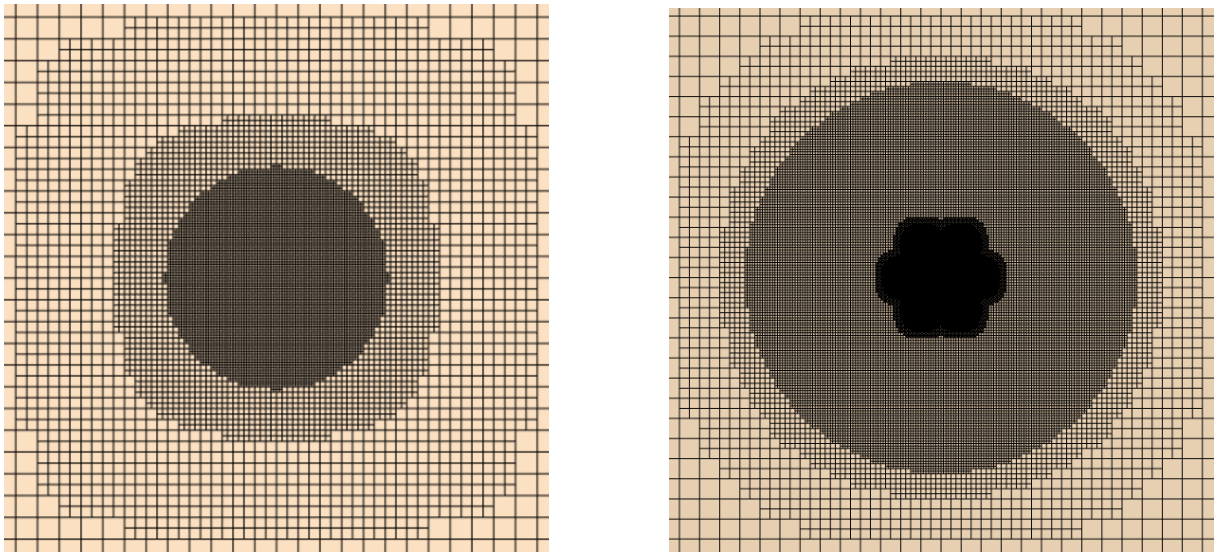

(a) *SR virtual disk model mesh* ***(b)*** *MR virtual disk model mesh, s/d=0.0*

Figure 3.5: *Virtual disk mesh*

The wake mesh size for the SR simulations can be seen in Figure 3.6, while the wake mesh for the MR simulations is shown in Figure 3.7.

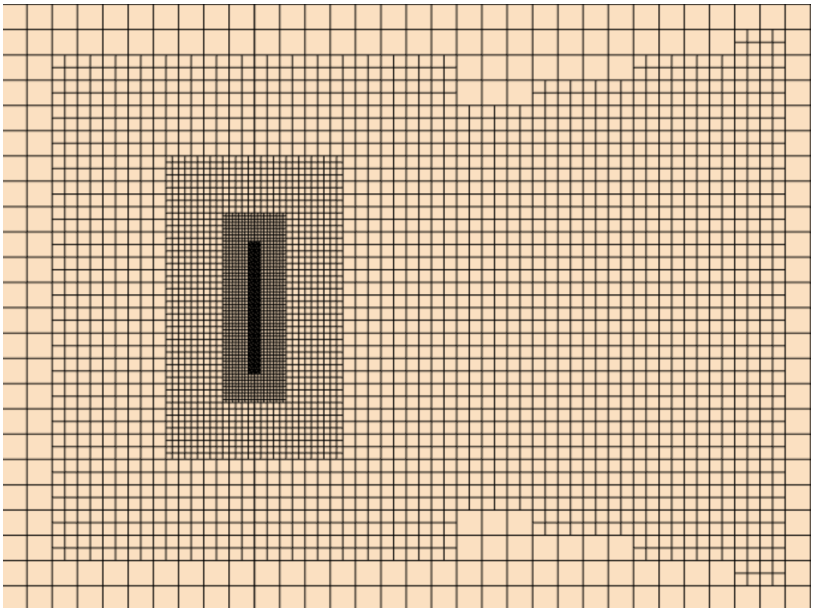

Figure 3.6: *Mesh in the wake of the SR virtual disk model*

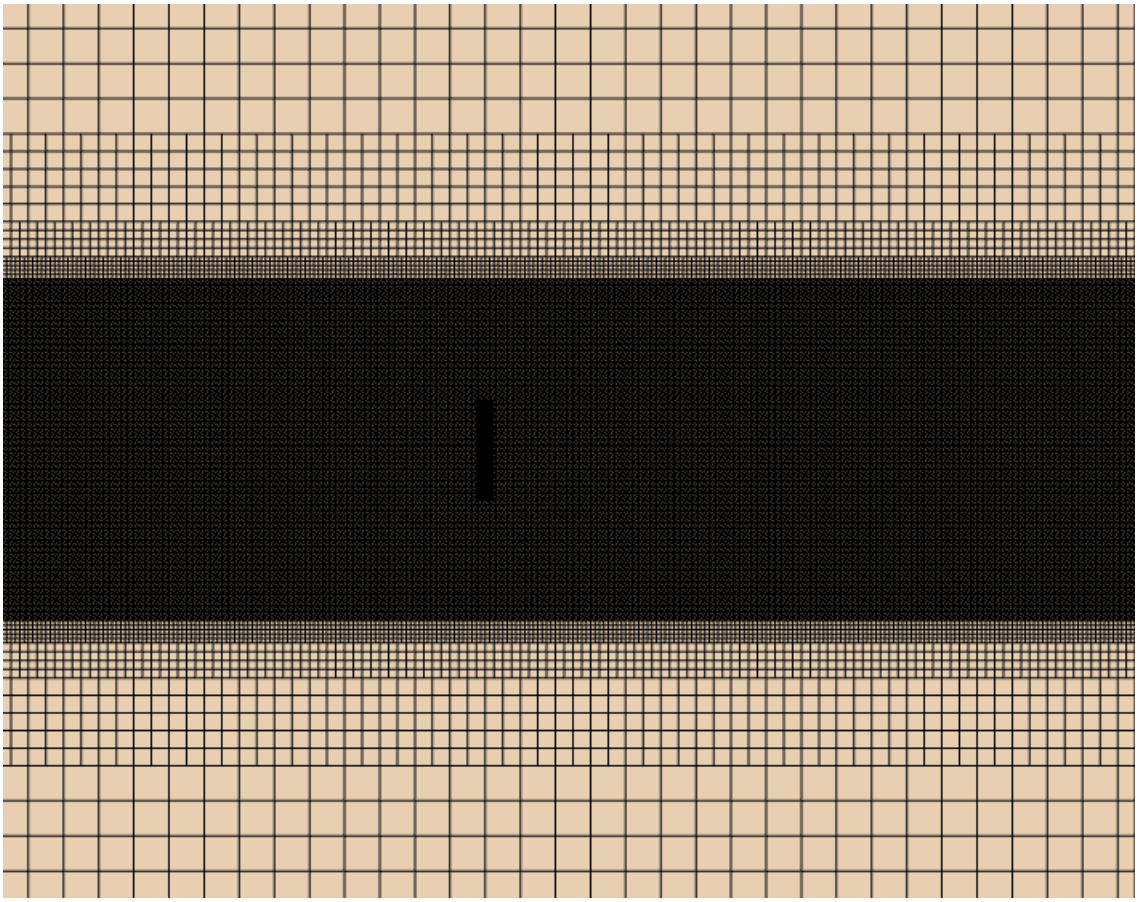

Figure 3.7: *Mesh in the wake of the MR virtual disk model, s/d=0.0*

For porous disc simulations, adaptive meshing was applied as well. This is a meshing technique where the area of interest, like for example the wake region, is meshed finer than the

surrounding domain. An example can be seen in Figure 3.8. In this simulation, the initial mesh is identical in the wake area. As the simulation starts and the wake propagates downstream, the mesh is refined to capture the flow more accurately. There are several criteria to set to determine the behaviour of the adaptive mesh. The adaptive mesh minimum size was set to 4 mm, both for accuracy and computational capacity reasons.

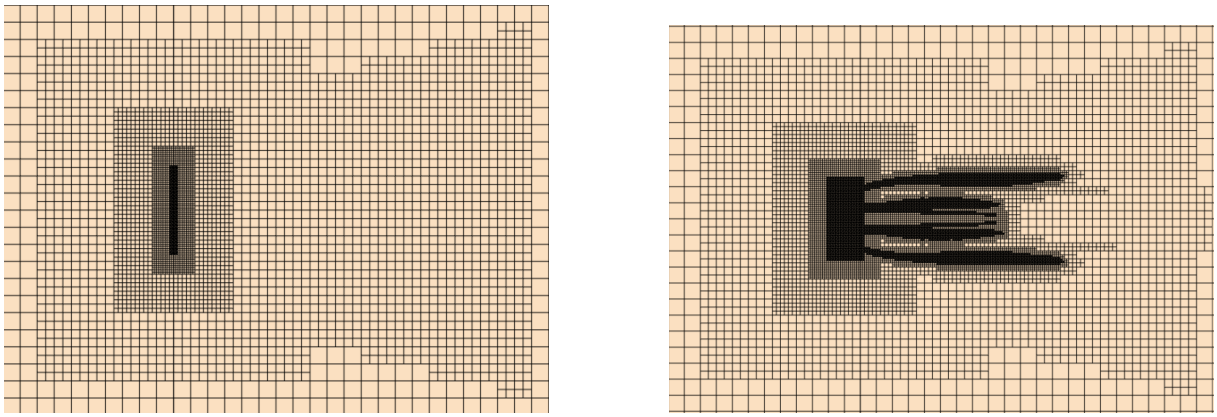

(a) *Initial mesh* ***(b)*** *Adaptive mesh*

Figure 3.8: *Adaptive meshing*

A close-up of the adaptive mesh can be seen in Figure 3.9

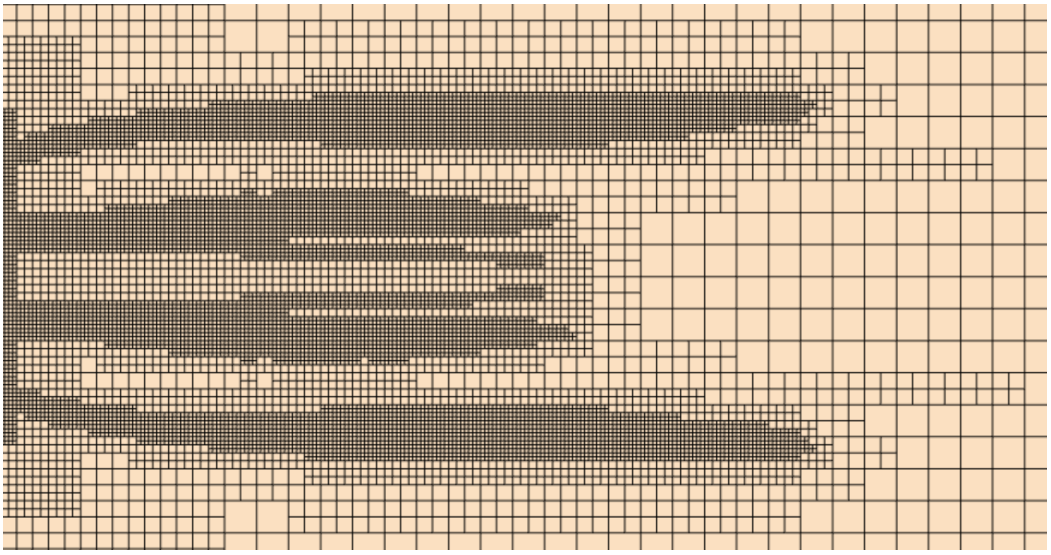

Figure 3.9: *Close-up of adaptive mesh in wake region*

The adaptive mesher was set to refine the mesh every 50 iterations of the simulation, in the regions where the vorticity was between 5 and 50 rotations per second, as this was the area of interest. Vorticity is a measure of the local rotation of a fluid element within a fluid flow [57]. The vorticity is equal to twice the angular velocity of the fluid element [26].

A mesh independence study was conducted to ensure the mesh was refined enough to accurately capture the physics. The mesh independence study will also confirm that the results are independent of the mesh size. Two separate mesh independence studies were performed, one for the mesh refinement around the virtual disks, and one in the wake behind the disks. Both the refinement zones can be seen in Figure 3.10, where the red zones are the refinement around the disks, and the green is the wake refinement.

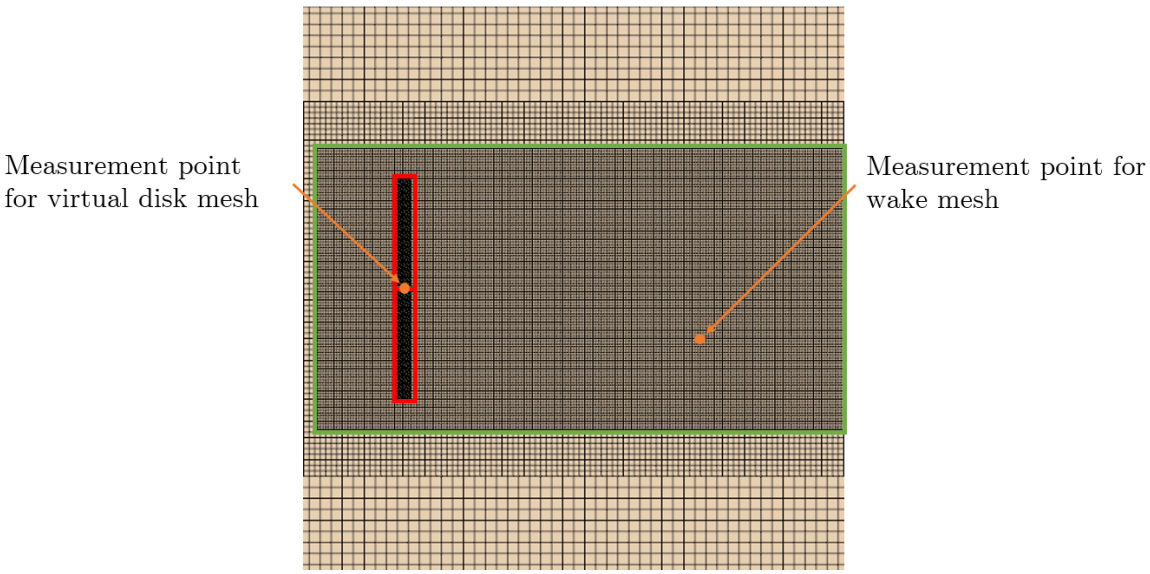

Figure 3.10: *Mesh independency study overview. The red zone represents the mesh around the virtual disk and the green is the wake mesh. Two measurement points are also presented, where velocity measurements for the study were performed. One point was placed between rotors, and the other was placed at a distance of three diameters downstream in the wake.*

For the wake mesh independence study, it was decided to measure the centerline velocity at a distance three diameters downstream of the virtual disk, as the wake velocity is a key parameter for wake studies. A point probe was placed at a distance of 3D downstream of the virtual disk as seen in Figure 3.10, where the velocity in the z-direction was measured at this point. Results from this study are presented in Figure 3.11.

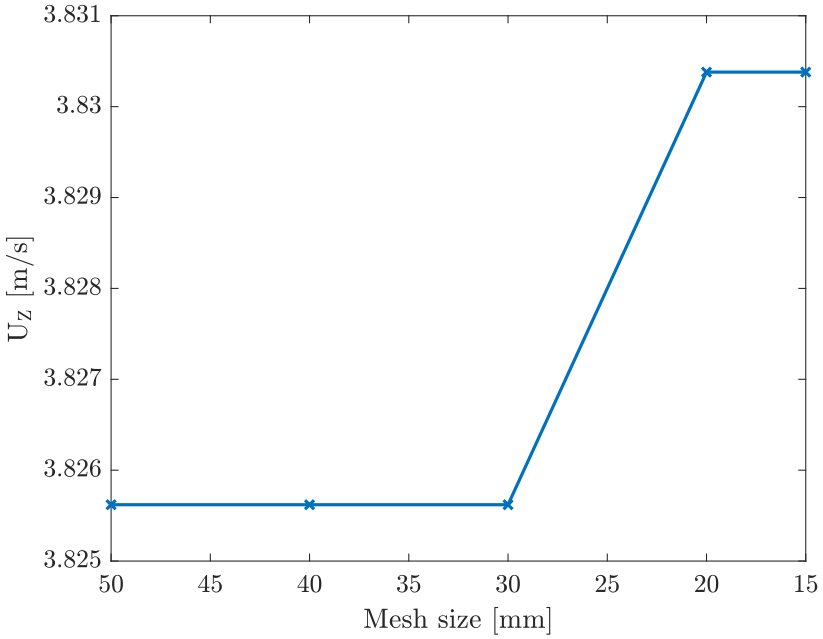

Figure 3.11: *Mesh independence study for wake mesh*

It was concluded to proceed with a mesh size in the wake of 20 mm, to keep the simulations as accurate as possible, while at the same time retaining the most amount of computational power. For the mesh refinement around the disk, the measured parameter was the velocity between the disks, to see how the disk interaction behaves with different mesh sizes. The virtual disk mesh independence study results are presented in Figure 3.12.

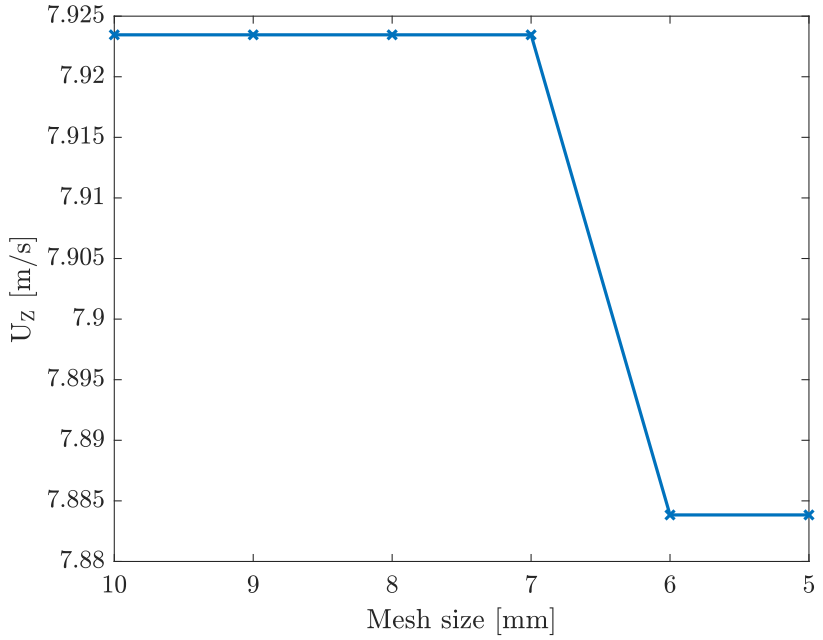

Figure 3.12: *Mesh independence study for virtual disk mesh*

Based on the results from the study, a mesh size of 6 mm was chosen around the virtual disk,

to retrieve the most accurate results while retaining the most computational power.

3.1.4 Turbulence Modelling

Irregularly fluctuating flow quantities characterise fluid flows at most times. The molecules within the flow move in a chaotic fashion along complex irregular paths. Because of increased momentum and energy exchange between molecules and solid walls, turbulent flow leads at the same conditions to higher skin friction and heat transfer as compared to laminar flow [54]. Turbulence plays a key role in transporting the mean kinetic energy from one location to another in turbulent flows [17].

In 1895, Osborne Reynolds presented the first approach for the approximate treatment of turbulent flows [58]. The governing Navier-Stokes equations are being solved for the mean values. He divided the flow variables into a mean and a fluctuating part. The velocity component and pressure from Eq. 3.1 and Eq. 3.2, 3.3, 3.4 can then be substituted by

$$u_i = \bar{u}_i + u_i' \tag{3.5}$$

and

$$p = \bar{p} + p' \tag{3.6}$$

where the mean values are denoted by an overbar and the turbulent part by a prime. Mean values are obtained by averaging, and there are three different forms of Reynolds averaging:

1. Time averaging
2. Spatial averaging
3. Ensemble averaging.

Time averaging is appropriate for stationary turbulence, spatial averaging can be used for homogenous turbulence while ensemble averaging, which is the most general type, is suitable for flows that decay in time [58]. Substituting Equations 3.5 and 3.6 into the Navier-Stokes equations given in Section 3.1.1 and dividing the momentum equations by density, ρ, gives

$$\frac{\partial \bar{u}_i}{\partial x_i} = 0 \tag{3.7}$$

and

$$\frac{\partial \bar{u}_i}{\partial t} + \frac{\partial}{\partial x_j}(\overline{u_i u_j}) = -\frac{\partial \bar{p}}{\partial x_i} + \nu \frac{\partial^2 \bar{u}_i}{\partial x_j \partial x_j}. \tag{3.8}$$

The quantity of the overscore is given as [59]

$$\overline{u_i u_j} = \overline{(\bar{u}_i + u_i')(\bar{u}_j + u_j')} = \overline{\bar{u}_i \bar{u}_j} + \overline{\bar{u}_i u_j'} + \overline{u_i' \bar{u}_j} + \overline{u_i' u_j'} = \bar{u}_i \bar{u}_j + \overline{u_i' u_j'} \tag{3.9}$$

which gives

$$\frac{\partial \bar{u}_i}{\partial t} + \frac{\partial}{\partial x_j}(\overline{u_i u_j}) = -\frac{\partial \bar{p}}{\partial x_i} + \nu \frac{\partial^2 \bar{u}_i}{\partial x_j \partial x_j} - \frac{\partial}{\partial x_j}(\overline{u_i' u_j'}), \tag{3.10}$$

and the Reynolds-averaged Navier-Stokes (RANS) equations are obtained [59] with Eq. 3.11 and Eq. 3.12

$$\frac{\partial \bar{u}_i}{\partial t} + \bar{u}_j \frac{\partial \bar{u}_i}{\partial x_j} = -\frac{\partial \bar{p}}{\partial x_i} + \nu \frac{\partial^2 \bar{u}_i}{\partial x_j \partial x_j} - \frac{\partial \tau_{ij}}{\partial x_j} \tag{3.11}$$

$$\frac{\partial \bar{u}_i}{\partial x_i} = 0 \tag{3.12}$$

with τ_{ij} being the Reynolds-stress term given as

$$\tau_{ij} = (\overline{u_i' u_j'}). \tag{3.13}$$

There are several different RANS turbulence models, both one-equation models like the *Spalart-Allmaras* model, and two-equation models such as the k-ϵ and k-ω turbulence models [58].

The k-ϵ turbulence model is the most used two-equation eddy-viscosity model and solves the transport equations for turbulent kinetic energy k and the turbulent dissipation rate ϵ [54]. The transport equations were suggested in the 1970s by Jones and Launder [60] and coefficients were suggested by Launder and Sharma [61]. The Launder-Sharma model is known as the Standard k-ϵ model and its kinematic eddy viscosity ν_t is given by

$$\nu_t = C_\mu \frac{k^2}{\epsilon} \tag{3.14}$$

where C_μ is an adjustable constant with a typical value of 0.09. The equation for turbulent kinetic energy k is

$$\frac{\partial k}{\partial t} + \bar{u}_j \frac{\partial k}{\partial x_j} = \frac{\partial}{\partial x_j}\left[\frac{(\nu + \nu_t)}{\sigma_k}\frac{\partial k}{\partial x_j}\right] - \epsilon + \tau_{ij}\frac{\partial \bar{u}_i}{\partial x_j}, \tag{3.15}$$

and turbulence energy dissipation ϵ is given by

$$\frac{\partial \epsilon}{\partial t} + \bar{u_j}\frac{\partial \epsilon}{\partial x_j} = \frac{\partial}{\partial x_j}\left[\frac{(\nu + \nu_t)}{\sigma_\epsilon}\frac{\partial \epsilon}{\partial x_j}\right] + C_{\epsilon 1}\frac{\epsilon}{k}\tau_{ij}\frac{\partial \bar{u_i}}{\partial x_j} - C_{\epsilon 2}\frac{\epsilon^2}{k}. \tag{3.16}$$

The closure coefficients and auxiliary relations in Equations 3.14, 3.15 and 3.16 are:

$$C_{\epsilon 1} = 1.44, \quad C_{\epsilon 2} = 1.92, \quad \sigma_k = 1.0, \quad \sigma_\epsilon = 1.3, \quad \omega = \epsilon/(C_\mu k) \quad \text{and} \quad l = C_\mu k^{\frac{3}{2}}/\epsilon \tag{3.17}$$

In the k-ϵ equations, σ_k and σ_ϵ are the Prandtl numbers for k and ϵ, equal to 1.0 and 1.3 respectively. $C_{\epsilon 1}$ and $C_{\epsilon 2}$ are also model constants similar to C_μ, equal to 1.44 and 1.92 respectively. The directional velocity component is represented by u_i and the rate of deformation is τ_{ij} [58]. k-ϵ is suitable for accurately predicting turbulent shear flows [62].

The k-ω is another widely used two-equation turbulence model. It was first composed by Kolmogorov in 1942 [63], improved further by Spalding and Launder in 1972 [64] and equations presented in this thesis are gathered from the Wilcox (2006) k-ω model. This version of the model dramatically improves the predictive accuracy of the Wilcox (1988a) model for free shear flows and strongly separated flows [58]. The kinematic eddy viscosity in this model is given as

$$\nu_T = \frac{k}{\tilde{\omega}} \tag{3.18}$$

where

$$\tilde{\omega} = \max\left\{\omega, C_{lim}\sqrt{\frac{2S_{ij}S_{ij}}{\beta^*}}\right\}, \qquad C_{lim} = \frac{7}{8}. \tag{3.19}$$

The turbulence kinetic energy k is defined as

$$\frac{\partial k}{\partial t} + U_j\frac{\partial \omega}{\partial x_j} = \tau_{ij}\frac{\partial U_i}{\partial x_j} - \beta^* k\omega + \frac{\partial}{\partial x_j}\left[\left(\nu + \sigma^*\frac{k}{\omega}\right)\frac{\partial k}{\partial x_j}\right] \tag{3.20}$$

and the specific dissipation rate ω is represented by

$$\frac{\partial \omega}{\partial t} + U_j\frac{\partial \omega}{\partial x_j} = \alpha\frac{\omega}{k}\tau_{ij}\frac{\partial U_i}{\partial x_j} - \beta\omega^2 + \frac{\sigma_d}{\omega}\frac{\partial k}{\partial x_j}\frac{\partial \omega}{\partial x_j} + \frac{\partial}{\partial x_j}\left[\left(\nu + \sigma\frac{k}{\omega}\right)\frac{\partial \omega}{\partial x_j}\right]. \tag{3.21}$$

The closure coefficients and auxiliary relations in Equations 3.19, 3.20 and 3.21 are [58]:

$$\alpha = \frac{13}{25}, \qquad \beta = \beta_o f_\beta, \qquad \beta^* = \frac{9}{100}, \qquad \sigma = \frac{1}{2}, \qquad \sigma^* = \frac{3}{5}, \qquad \sigma_{do} = \frac{1}{8} \tag{3.22}$$

where

$$\sigma_d = \begin{cases} 0, & \frac{\partial k}{\partial x_j}\frac{\partial \omega}{\partial x_j} \leq 0 \\ \sigma_{do} & \frac{\partial k}{\partial x_j}\frac{\partial \omega}{\partial x_j} > 0 \end{cases}. \tag{3.23}$$

Further,

$$\beta_o = 0.0708, \qquad f_\beta = \frac{1+85\chi_\omega}{1+100\chi_\omega}, \qquad \chi_\omega = \left|\frac{\Omega_{ij}\Omega_{jk}S_{ki}}{(\beta^*\omega)^3}\right| \tag{3.24}$$

and

$$\epsilon = \beta^*\omega k \qquad \text{and} \qquad l = k^{\frac{1}{2}}/\omega. \tag{3.25}$$

Ω_{ij} and S_{ij} are tensors for mean-rotation and mean-strain-rate, given by

$$\Omega_{ij} = \frac{1}{2}\left(\frac{\partial U_i}{\partial x_j} - \frac{\partial U_j}{\partial x_i}\right) \qquad \text{and} \qquad S_{ij} = \frac{1}{2}\left(\frac{\partial U_i}{\partial x_j} + \frac{\partial U_j}{\partial x_i}\right). \tag{3.26}$$

In the k-ω equations, C_{lim} is the stress-limiter strength, f_β is the vortex-stretching function, χ_ω is the dimensionless vortex-stretching parameter. The k-ω has replaced the k-ϵ as the most used two-equation model and has several advantages [58]. It is significantly more accurate for two-dimensional boundary layers with both adverse and favourable pressure gradients and with viscous corrections included, it accurately reproduces subtle features of turbulent kinetic energy behaviour close to a solid boundary and even describes boundary-layer transition reasonably well [58].

Three different RANS models were tested in Mcnaughton et al. [65] to model a turbulent flow past a tidal stream turbine. The different models were the k-ϵ and k-ω SST eddy viscosity models and the Launder-Reece-Rodi (LRR) Reynolds Stress Model (RSM). RSM possess the capability to capture anisotropy by addressing distinct transport equations for each of the Reynolds stresses. In contrast, the eddy-viscosity models fall short in achieving this level of sophistication as they make the assumption that the Reynolds Stress tensor is directly proportional to the mean strain rate. For a range of the tip speed ratios tested in [65] the *k-ω SST* model gave the closest results to the compared experimental data. The LRR model underpredicted the force coefficients of the SST while showing greater fluctuations in the instantaneous values. It was found that the k-ϵ model performed poorly and was unsuitable for the complex flow of the simulation.

The k-ϵ and the k-ω turbulence models were also used in Stergiannis et al. [66] in their

investigation of the single wake expansion of an upstream wind turbine. Two wind turbine generators including the exact geometry of blades and hub were compared against a simplified actuator disc. The study showed that the k-ϵ model had better agreement with the experimental data for the case of the actuator disc, whereas the k-ω performed better for full wind turbine simulations.

CFD simulations of HAWT were performed by Garcia-Ribeiro et al. [67] in 2023. The performance of the turbulence models k-ϵ, Spalart-Allmaras and k-ω SST was analysed with RANS equations. The simulations were compared against experimental data from Boorsma and Schepers [68], where the wind turbine studied was the New Mexico HAWT with three blades and a rotor radius of 4.5 m. The k-ϵ model underestimated both torque and thrust for all wind speeds, but the agreement was still within 15 % for the whole range. For high wind speeds, the k-ϵ model had an agreement within 5 %. The k-ω SST model also underpredicted both torque and thrust. For high wind speeds, the model accurately predicted torque and thrust. The margins from the k-ω SST model are similar to the margins from the k-ϵ model but with a higher computational cost. It was concluded that even though the k-ω SST model is the most used in HAWT simulations, the k-ϵ model emerges as a promising alternative due to its comparable overall accuracy to the k-ω SST model, using a coarser mesh and has lower computational costs.

3.1.5 Computational Accuracy

When the flow in numerical simulations such as CFD becomes turbulent instead of laminar, the difficulty of solving the simulations increases significantly. When the flow is turbulent, the turbulent eddies appear, which are random, swirling, vertical structures that are always unsteady and three-dimensional [28]. There are different ways of dealing with these eddies in CFD simulations. Techniques such as DNS (Direct Numerical Simulation), LES (Large Eddy Simulation) and RANS (Reynolds-averaged Navier-Stokes) all have different methods of solving the flow field of the unsteady eddies. All turbulent eddies in the flow are simulated with DNS, as shown in Figure 3.13.

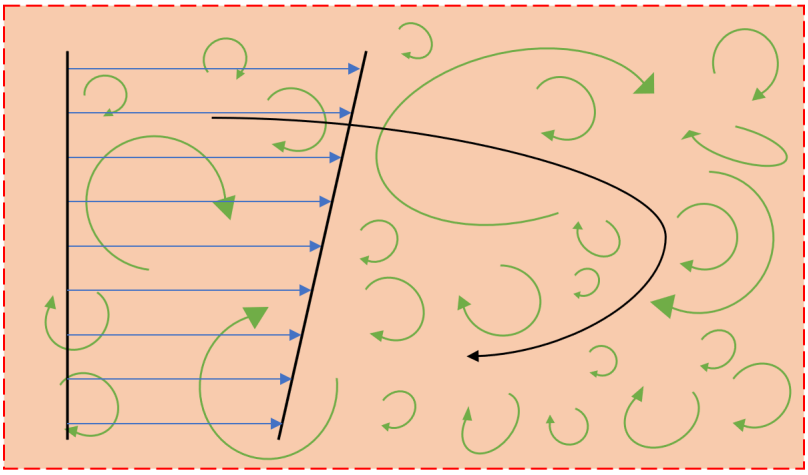

Figure 3.13: *DNS illustration. The average velocity profile is shown along with all turbulent eddies simulated in the flow. Inspired by Figure 15-44 in [28].*

As all the eddies vary in size and length, this technique requires significant amounts of computational power and an extremely refined grid. Because of this, solving CFD simulations using DNS takes too long time to be an option for most simulation purposes [28]. Some simplifications and assumptions are needed to simulate these turbulent flow fields, leading to LES, which resolve the largest eddies, while the smaller ones are modelled, as seen in Figure 3.14.

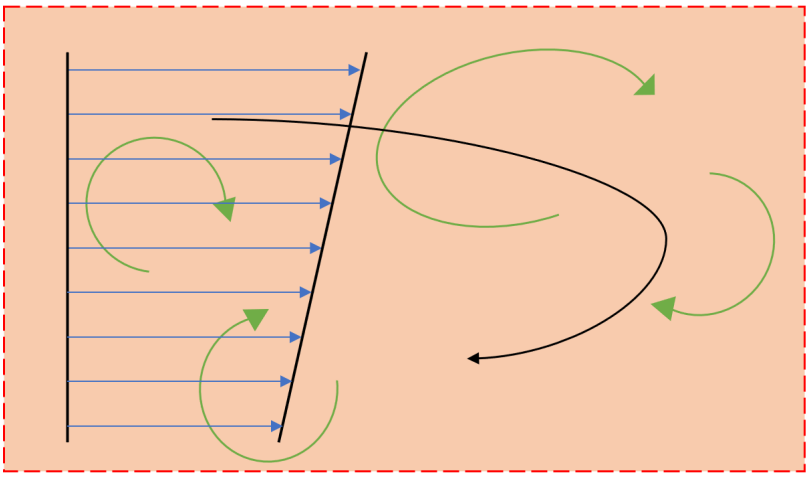

Figure 3.14: *LES illustration. Shown is the average velocity profile with only the largest turbulent eddies simulated, the smaller ones are modelled. Inspired by Figure 15-45 in [28].*

The smaller eddies are assumed to be isotropic [28]. When modelling the small eddies instead of resolving them, the need for such enormous data power is reduced. However, these simulations still require such amounts of computational power that one simulation might take several days or even weeks on a powerful computer with several CPUs. To further

reduce the computational time to run the simulations, all the unsteady eddies are modelled by the use of a turbulence model. With this technique, the Reynolds-averaged Navier-Stokes equation is employed to mathematically model the mixing and diffusion which are caused by the turbulent eddies [28]. Figure 3.15 illustrates how this technique resolves the flow field.

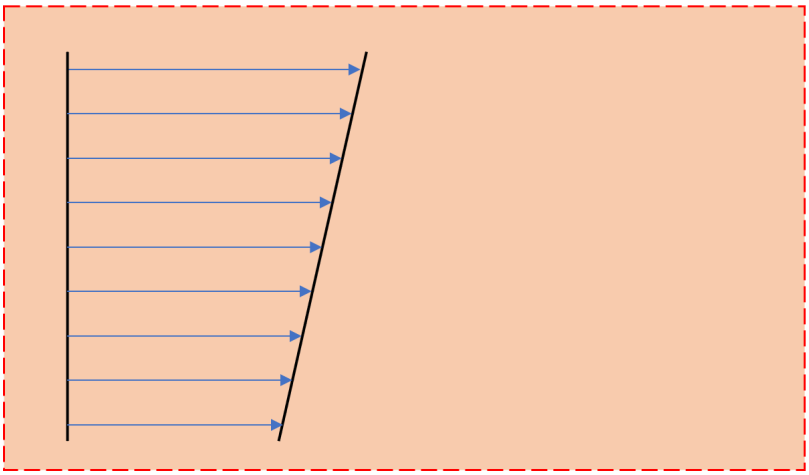

Figure 3.15: *RANS illustration. Shown is the average velocity profile, where all the eddies are modelled. Inspired by Figure 15-46 in [28].*

As turbulence models are approximations which rely on the underlying mathematical expressions, the choice of which turbulence model to use depends on the simulation to be performed, although one model works for one simulation, it may not work for other simulations.

3.2 Computational Solvers

Two computational solvers are being utilised throughout this thesis. For CFD simulations, STAR-CCM+ is employed. For blade element momentum (BEM) calculations, the QBlade software is being used.

3.2.1 STAR-CCM+

STAR-CCM+ was initially developed by CD-adapco and was acquired and further developed by Siemens Digital Industries Software. The Simcenter STAR-CCM+ Software is a computational aided engineering (CAE) solution for solving multidisciplinary problems in both fluid and solid continuum mechanics, within a single integrated user interface [55].

The physics represented in STAR-CCM+ originates from the fundamental laws of physics. For fluid flow, the governing equations are the continuity equation, as well as the momentum equation and energy equation. The turbulence models in STAR-CCM+ are subdivided into two categories, the Reynolds-averaged Navier-Stokes (RANS) turbulence models and scale-resolving simulations, such as Large Eddy Simulation and Detached Eddy Simulation. The RANS turbulence models provide closure relations for the Reynolds-averaged Navier-Stokes equations, that govern the transport of the mean flow quantities. The RANS turbulence models include six variants of the k-ϵ model, as well as two variants of the k-ω model [55]. Unlike the RANS models, the scale-resolving simulations resolve large scales of turbulence and model small-scale motions. Both LES and DES fall within this category. LES is a transient technique where the large scales of turbulence are directly resolved everywhere in the flow domain, and the small-scale motions are modelled [55]. DES is a hybrid between RANS and LES, which combines the two approaches. A DES was performed to extract the forces acting on the disc for the porous disc simulations. In this simulation, RANS was applied on the disc and in the immediate vicinity, while LES was applied in the wake behind the porous disc.

3.2.2 QBlade

QBlade is an aero-servo-hydro-elastic code which covers all aspects required for wind turbine design, simulation and certification [69]. For aerodynamic calculations, QBlade utilises the lifting line free vortex wake method and simulations of HAWT are performed using the blade element momentum (BEM) method.

Marten et al. [70] compared the BEM algorithm of QBlade against experimental data, and the comparisons showed great agreement. Alaskari et al. [71] performed an analysis of a HAWT blade using the QBlade software. The QBlade analysis calculated that the maximum C_L/C_D value occurred at an angle of attack of 2° and that the optimum rotor performance occurred at a tip speed ratio of 8. The results from QBlade were of high resolution, and the authors concluded that for the design and optimisation of blades and rotors, the QBlade software is considered one of the most important.

3.3 Virtual Disk Model

The virtual disk model in STAR-CCM+ is based on representing propellers, turbines, rotors, fans and so on as an actuator disk. The use of an actuator disk approach becomes useful when the focus is on understanding the impact of rotor behaviour on the flow, instead of the detailed interactions between the flow and the rotating device's blades [55]. There are different methods implemented in the virtual disk model, the "Blade Element Method", the "1D Momentum Method" and a "User Defined Method".

In the blade element method, the rotor is modelled by a distribution of momentum sources. The blade geometry of the rotor is uploaded as input for this method, such as which airfoil sections the blade is made of, along with the distribution of chord, twist and sweep angle. Based on the rotor geometry and the local velocity field, the strength of the source terms is being determined. Together with the airfoil section, the lift- and drag coefficients need to be uploaded for the method to understand how the blade design impacts the airflow [55].

The 1D momentum method is employed to simulate the influence of a wind turbine on its surroundings. The one-dimensional momentum theory with wake rotation is the basis for the 1D momentum method. A source term is added to the momentum equations that account for axial and tangential effects. A power curve is uploaded as input for this method. The power curve contains the thrust coefficient and power as a function of wind speed. An inflow velocity plane, further discussed in Section 3.3.1, is used to calculate the source term from the uploaded power curve. This method is applicable for analysing the wake effects of an individual wind turbine or an entire wind farm [55].

The user defined method (UDM) was created to simulate the behaviour of a rotating device. This is achieved by defining a volume force on a cylindrical mesh in three-dimensional space. The virtual disk geometry is utilised to determine the disc's size, location and orientation. A three-dimensional resolution needs to be specified for the virtual disk, azimuthal, normal and radial resolution, further explained in Section 3.3.1. The resolution divides the virtual disk into 'buckets'. A velocity inflow plane is used to acquire velocity and density data from the flow field. A volumetric source term is assigned to each bucket on the virtual disk [55].

3.3.1 Porous Disc Simulations

For the porous disc simulations, the blade element method was determined unsuitable for the simulation of a porous disc, as the input for this particular method required airfoil sections along the blade radius. This method also has input parameters such as chord-, sweep angle- and twist distribution, which are used for typical wind turbine blades, but unsuitable for a porous disc. The 1D momentum method was also tested but deemed unsuitable as well due to the strong effect of the input parameter "rotation rate", which is not present for a porous disc. Due to this, it was decided to proceed with the user defined method (UDM), as this method was best suited to simulate a porous disc within the virtual disk environment available in STAR-CCM+.

Within the UDM, there are several choices on how to simulate the behaviour of the virtual disk. The porous disc geometry was specified to have a radius of 100 mm and a thickness of 5 mm to match the actuator disc used in [24]. The settings for disk resolution determine the number of "buckets" the virtual disk will contain. A bucket represents a cylindrical sector. The radial resolution was set to 12, meaning there will be 12 buckets spreading from the disc centre towards the edge. The azimuthal resolution was set to four and the normal resolution was set to one, as there is only one force contribution in the z-direction. How the buckets are placed on the virtual disk for these settings can be seen in Figure 3.16.

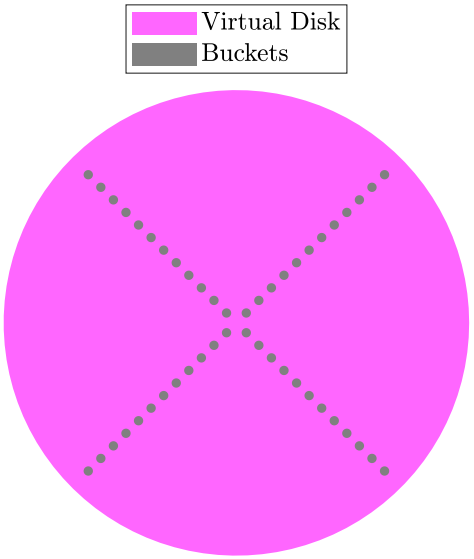

Figure 3.16: *Buckets on virtual disk*

A total of 48 buckets were created (12 radial x 4 azimuthal x 1 normal) on the virtual disk. The

buckets are run through in the azimuthal direction [55], illustrated on a simplified disc in Figure 3.17.

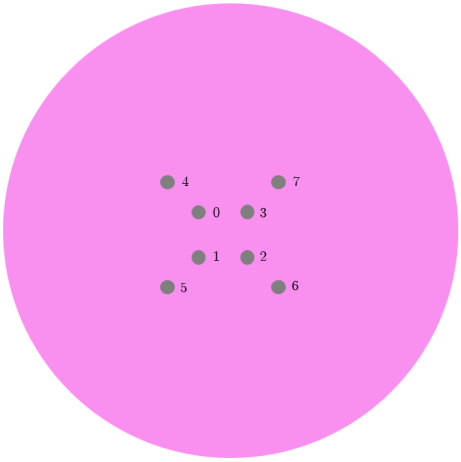

Figure 3.17: *Order of how buckets are read*

The virtual disk is also equipped with an inflow velocity plane. The inflow plane is located upstream of the disk and is oriented normally to the disk. Over the inflow velocity plane, the velocity components and the density of the fluid flowing towards the disk are volume-averaged [55]. Then they are projected onto the plane of the virtual disk. A representation is shown in Figure 3.18.

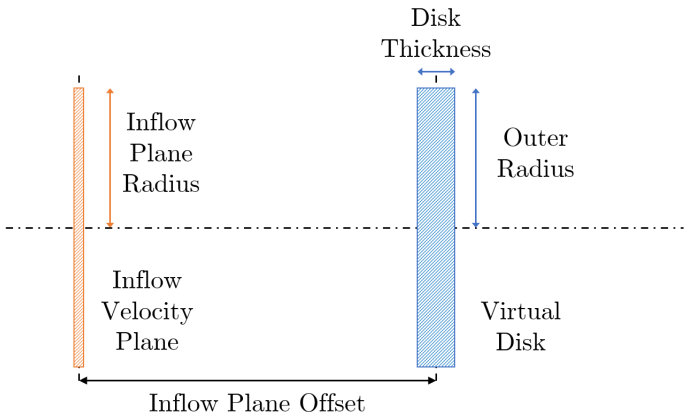

Figure 3.18: *Inflow velocity plane characteristics. Inspiration from [55].*

For the UDM, the velocity plane is the only inflow specification available. The inflow plane has the same radius as the virtual disk and the same disk resolution, i.e. the same amount of buckets. For the 1D Momentum method, several options regarding inflow specification may be chosen.

The velocity plane offset for the porous disc simulations was chosen to be -0.1 m, based on a parameter study as shown in Table 3.2.

Table 3.2: *Velocity plane offset study. As the inflow velocity plane is located upstream of the virtual disk, the offset is given in the negative z-direction.*

Velocity plane offset [m]	Convergence (Yes/No)
-0.05	No
-0.09	No
-0.10	Yes
-0.11	No
-0.15	No

3.3.2 Model Wind Turbine Simulations

Due to comparisons of important wind turbine parameters between BEM calculations in QBlade, BEM simulations in STAR-CCM+ and simulations using the 1D Momentum method in STAR-CCM+, depicted in Figure 3.19, it was decided to proceed with the 1D Momentum method in STAR-CCM+ for the virtual disk simulations using the model wind turbine as reference.

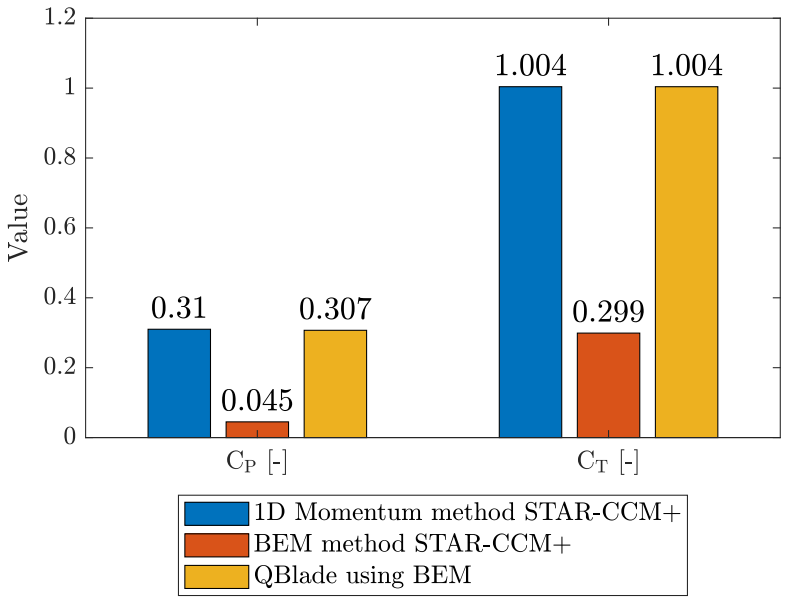

Figure 3.19: *Comparison of C_T and C_P. This comparison aimed to verify which method in STAR-CCM+ produced the most similar results to the ones obtained in QBlade through BEM calculations.*

A power curve was uploaded as input for the virtual disk model in the 1D momentum method. The power curve contains wind speed, power and thrust coefficient. The power curve can be seen in Figure 3.20.

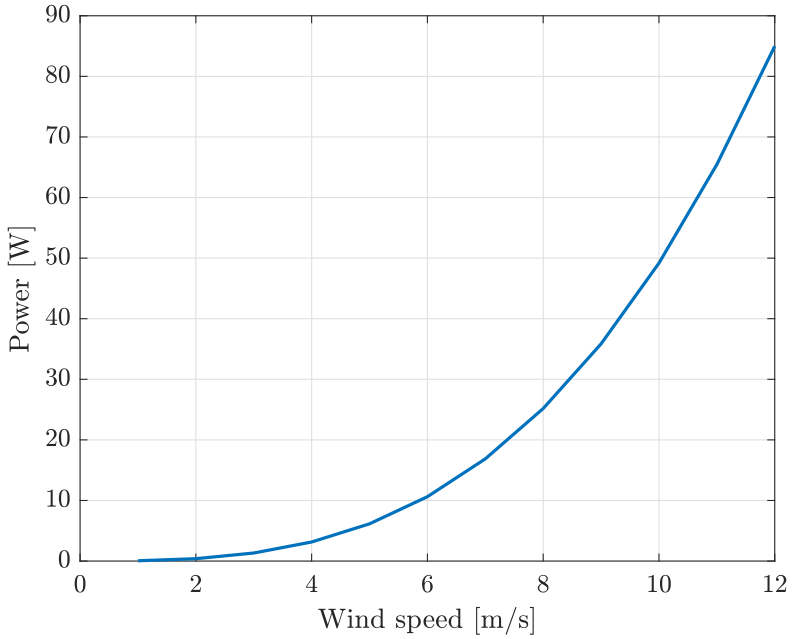

Figure 3.20: *Power curve for input to 1D Momentum Method. Data retrieved from QBlade BEM calculations on the ForWind model wind turbine.*

The thrust coefficient was held constant for all wind speeds at 1.0. Simulation parameters in QBlade were set to match the inflow conditions in Neunaber [25], with an inflow velocity of ~ 7.5 m/s and the turbine operating at a tip speed ratio of 6. The disc geometry was set to match the ForWind model turbine, except for the inner radius which was set to 0 mm due to an unfavourable W-shape forming in the wake when the inner radius was set equal to the hub radius, shown in Figure 3.21.

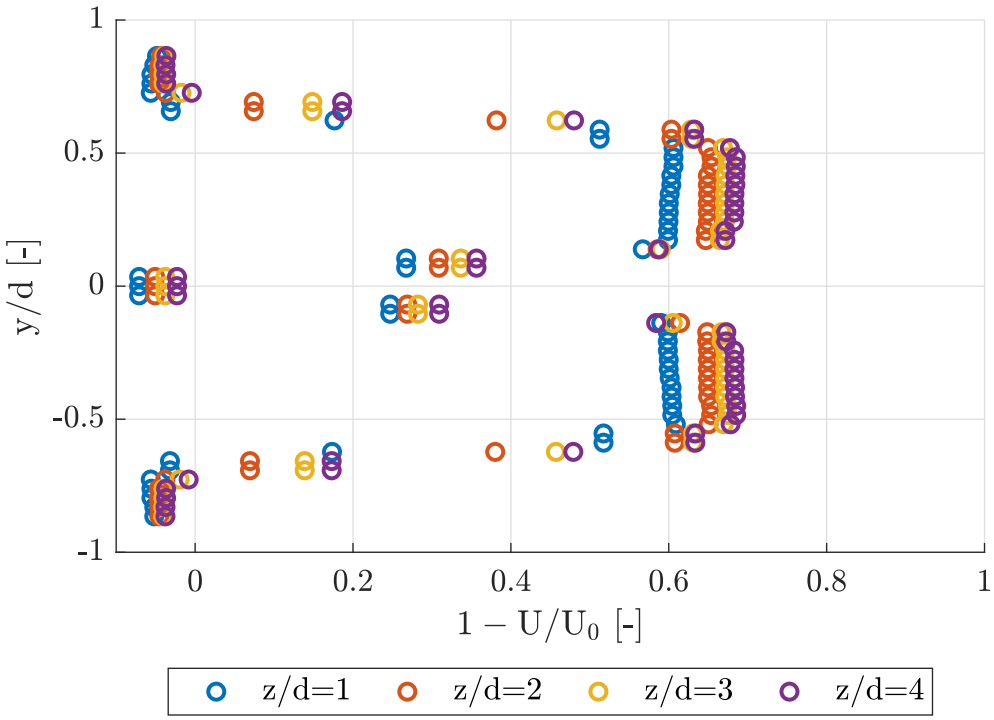

Figure 3.21: *W-shaped wake profile at different downstream distances, d equals the rotor diameter of the ForWind model wind turbine of 0.578 m.*

The rotation rate was calculated using the formula for tip speed ratio, Eq. 2.17:

$$\lambda = \frac{\omega r}{U_0} \rightarrow \omega = \frac{\lambda U_0}{r} = 155.71 \text{ rad/s}$$

with r being the rotor radius of 289 mm.

An "inflow velocity plane" study was conducted for simulations with the ForWind turbine as well. For the 1D momentum method, the user manual [55] recommends an inflow plane radius 10 % larger than the virtual disk radius. For the ForWind MWT, that represents 317.9 mm, as the radius is 289 mm. A study was carried out to find the optimal offset. Several offsets were tested, and the results are presented in Table 3.3.

Table 3.3: *Velocity plane offset study for the model wind turbine simulations using 1D momentum method. As the inflow plane is located upstream of the virtual disk, the offset is given in the negative z-direction, with d being the ForWind model wind turbine diameter.*

Velocity plane offset [d]	**Power [W]**
-0.1	13.9
-1.0	20.3
-1.5	20.9
-1.6	21.0
-1.7	21.0

Based on the performed study, an inflow velocity plane offset of -1.7 d was chosen, corresponding to an upstream distance from the virtual disk of -0.98 meters. The study aimed to produce the same power as simulated in QBlade, a value of 21.0 W.

3.4 Thrust Force Modelling Approaches

The UDM input requires force per volume. To obtain this, the thrust force values were divided by their respective volumes. For the UDM, various methods of inputting values can be selected, i.e. "table", "constant", "composite" etc. These are different ways of formatting the input data as desired. A "Table (x, y, z)" approach was selected as the forces act differently radially over the disc. The "Table (x, y, z)" method takes in coordinates in x-, y- and z-direction, as well as forces in the three directions, F_x, F_y and F_z. Only a force in the z-direction was applied.

Figure 3.22 illustrates the force distribution over the virtual disk. A total of 48 points were used as source term inputs, distributed over 12 radial, four azimuthal and one normal.

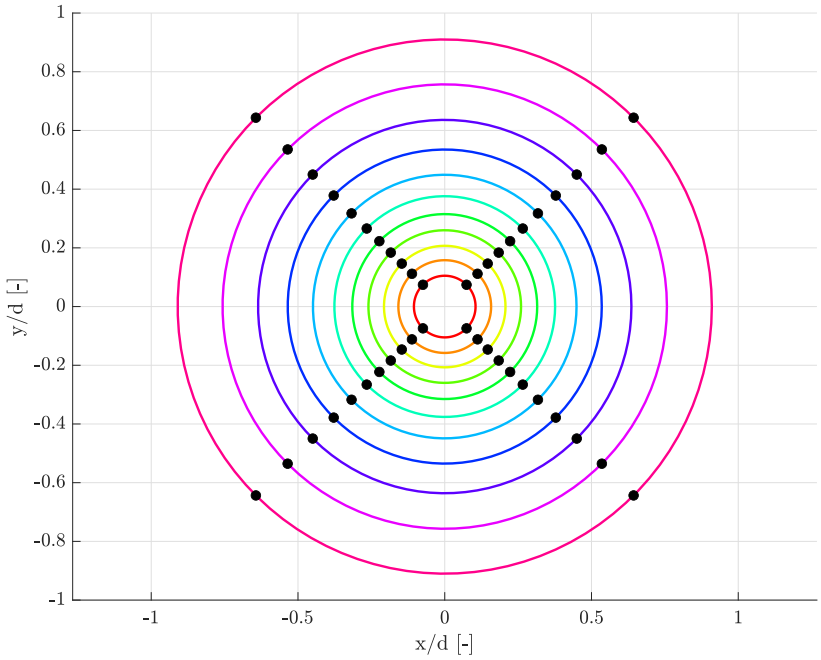

Figure 3.22: *Force distribution over the virtual disk, d represents the porous disc diameter.*

3.4.1 Approach 1: Taylor Equations

Eriksen [42] used the Taylor equations to theoretically determine the thrust coefficient C_T based on the porosity which is directly linked with solidity by Equation 2.26, and a resistance coefficient κ. The relationship between disc porosity and the resistance coefficient is described as

$$\Phi^2 = \frac{1}{1+\kappa}. \tag{3.27}$$

The resistance coefficient can further be used to calculate the thrust coefficient of the disc,

$$C_T = \frac{\kappa}{\left(1+\frac{1}{4}\kappa^2\right)}. \tag{3.28}$$

The Taylor equations originate from the work of Sir Geoffrey Ingram Taylor [72]. The porous disc used in Øye [24] had a solidity of 57 %, corresponding to a porosity of 43 %. Using Equation 3.27 and Equation 3.28, the resistance coefficient κ and thrust coefficient C_T were calculated to be 4.4 and 1.0 respectively. Knowing the thrust coefficient and some parameter values from Øye [24], the thrust force F_T can be calculated using Equation 2.10. For a towing speed of 0.4 m/s, the thrust force was calculated to 2.49 N.

Because of the discs varying solidity, a radial distribution of disc solidity was found using

data from Eriksen [42]. Implementing this into the CFD simulation will improve the force distribution acting on the simulation disc to correspond to the forces acting on the porous disc in MarinLab. The radial distribution of disc solidity and thrust coefficient at different radial distances from the disc centre can be seen in Table 3.4.

Table 3.4: *Normalised radial distribution of solidity and thrust coefficient over the porous disc using the Taylor equations.*

R/r [-]	**Solidity [%]**	**C_T [-]**
0.11	96.5	0.019
0.16	92.3	0.091
0.21	88.4	0.196
0.26	84.7	0.319
0.32	81.0	0.453
0.38	77.2	0.590
0.45	73.2	0.722
0.54	69.1	0.835
0.64	65.0	0.920
0.76	61.4	0.967
0.91	58.8	0.990

Knowing the disc solidity and thrust coefficient at different radial distances, the thrust force distribution can be calculated. These calculations are presented in Table 3.5.

Table 3.5: *Normalised radial thrust force distribution over the porous disc using the Taylor equations.*

R/r [-]	**Thrust force [N]**
0.11	0.049
0.16	0.180
0.21	0.264
0.26	0.309
0.32	0.336
0.38	0.344
0.45	0.331
0.54	0.284
0.64	0.213
0.76	0.124
0.91	0.053

An illustration of how the forces are distributed over the virtual disk is illustrated in Figure 3.23.

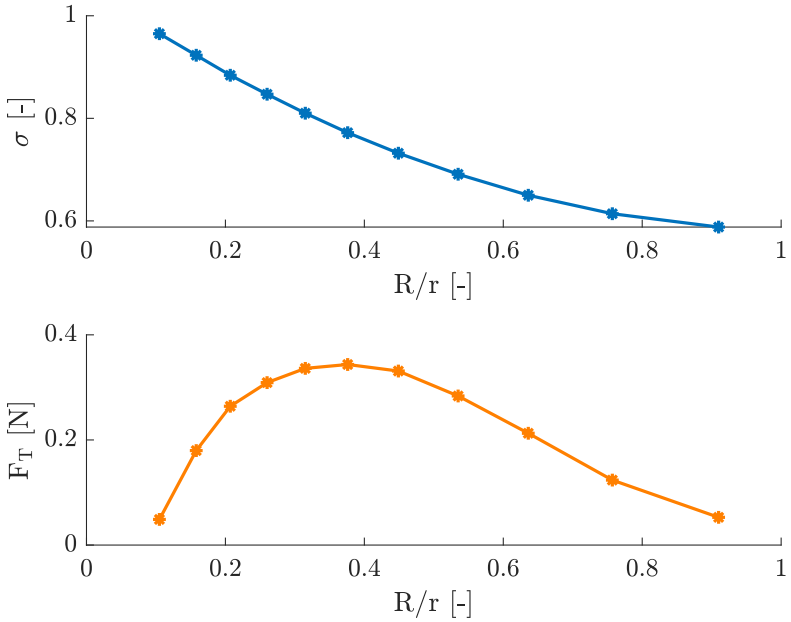

Figure 3.23: *Normalised radial distribution of solidity and thrust force on the virtual disk based on the Taylor equations.*

3.4.2 Approach 2: Ranjbar Equations

As discussed in Section 2.5.1, Ranjbar et al. [45] did both numerical simulations and physical experiments on porous discs. Based on these simulations and experiments, they formulated equations for both thrust coefficient and power coefficient, based on disc solidity. The equations were

$$C_P = \frac{64}{27}\sigma(1-\sigma)$$

and

$$C_T = \frac{64}{9}\frac{\sigma(1-\sigma)}{3-2\sigma}.$$

As these equations are only valid for a solidity range of $0.2 < \sigma < 0.6$, the total disc solidity of 0.57 was used. Calculations using the above equations are shown in Table 3.6.

Table 3.6: *Calculations from Ranjbar et al.*

σ [-]	C_T [-]	**Thrust force [N]**
0.57	0.94	2.35

The thrust force obtained through calculations was scaled according to the solidity curve as the article by Ranjbar [45] discovered that the distribution of the thrust coefficient was proportional to the solidity distribution.The thrust distribution per radial distance for this

approach is shown in Table 3.7.

Table 3.7: *Normalised radial distribution of thrust force on the porous disc using the Ranjbar equations.*

R/r [-]	Thrust force [N]
0.11	0.268
0.16	0.256
0.21	0.245
0.26	0.235
0.32	0.225
0.38	0.214
0.45	0.203
0.54	0.192
0.64	0.180
0.76	0.170
0.91	0.163

The distribution of forces along radial distances is illustrated in Figure 3.24.

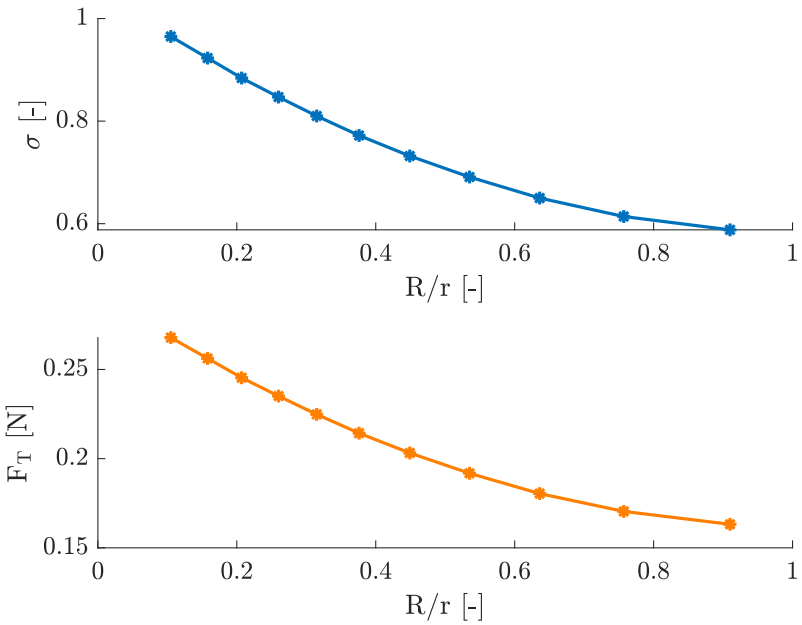

Figure 3.24: *Radial distribution of solidity and thrust force on the virtual disk from the Ranjbar equations.*

3.4.3 Approach 3: Data Retrieved from Detached Eddy Simulation

A Detached Eddy Simulation (DES) on the exact geometry of the disc was performed to accurately retrieve the force distribution acting on the porous disc. A CAD (Computer-aided design) model of the disc geometry was imported to STAR-CCM+ and meshed very finely (3

mm) to accurately capture the forces acting on the disc. The advantage of this model is that it provides accurate predictions of turbulent flows while being computationally effective. The simulation model runs RANS in the rotor plane and LES in the wake. Figure 3.25 shows the vorticity field from the Detached Eddy Simulation.

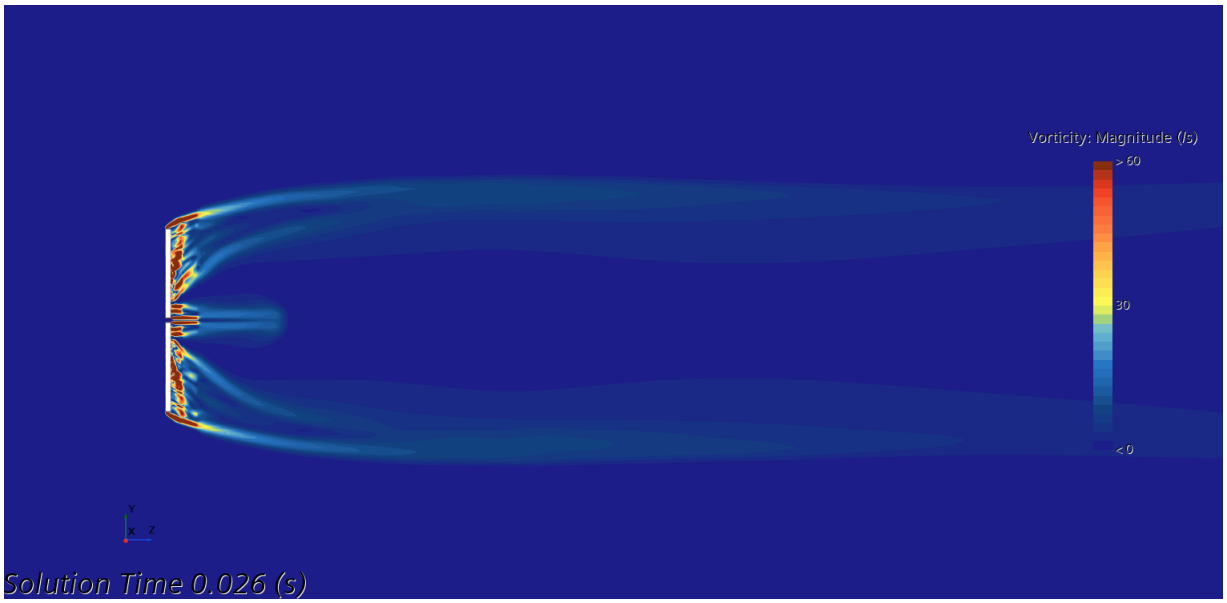

Figure 3.25: *Vorticity field from the reference Detached Eddy Simulation on the actual geometry of the porous disc which will be used for comparison against results obtained through CFD RANS simulations.*

Results from the DES simulation measured a thrust force of 2.16 N acting on the disc, within 2 % of the thrust force measured by Øye [24] in MarinLab of 2.12 N. To obtain the radial force distributions acting on the disc, "line probes" were set in STAR-CCM+ to measure forces acting on the probe from the disc centre to the disc edge. Figure 3.26 displays how the line probes were set to measure forces both along bars and also between bars.

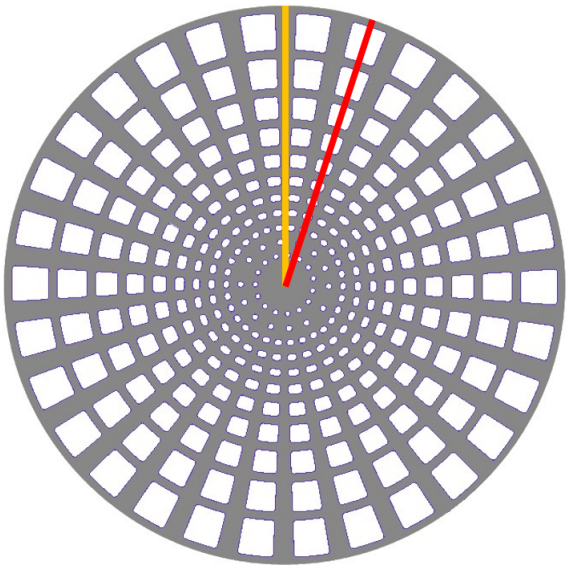

Figure 3.26: *Line probes set to retrieve thrust force measurements in the Detached Eddy Simulation.*

Each probe contained 10000 measurement points. An interpolation was performed to find the force distribution affected by both bars and between bars. This distribution is seen in Figure 3.27.

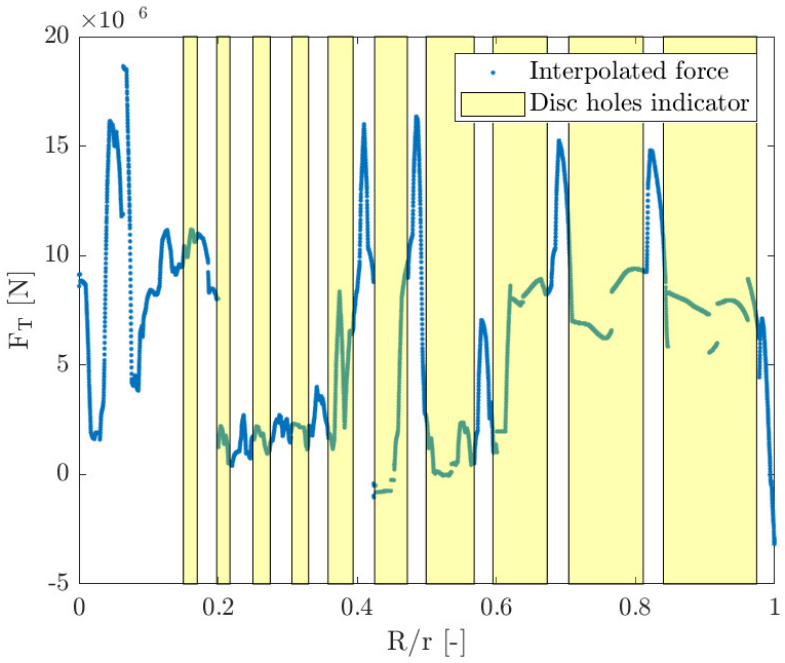

Figure 3.27: *Interpolated thrust force distribution over the porous disc.*

The yellow markings in Figure 3.27 indicate where the porous disc holes are located. It can be observed that from a normalised radial distance of 0.4 from the disc centre, the effect of the

trapezoidal holes plays a part in the force distribution towards the end. As seen in Figure 2.12, the disc has a high solidity near the centre and gradually decreases towards the end. The distribution of forces and solidity are shown in Figure 3.28.

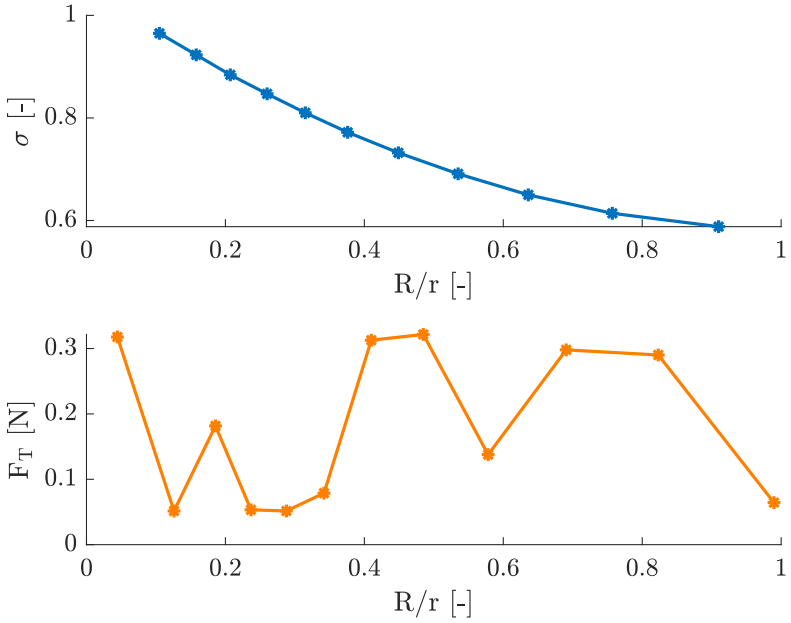

Figure 3.28: *Normalised radial distribution of solidity and thrust force on the virtual disk using input from the Detached Eddy Simulation.*

3.4.4 Comparison of Modelled Thrust Force Distribution

A comparison was made between the different approaches for modelling the distribution of thrust force on porous disc, shown in Figure 3.29. It can be seen that the different approaches tested all gave various distributions of thrust force.

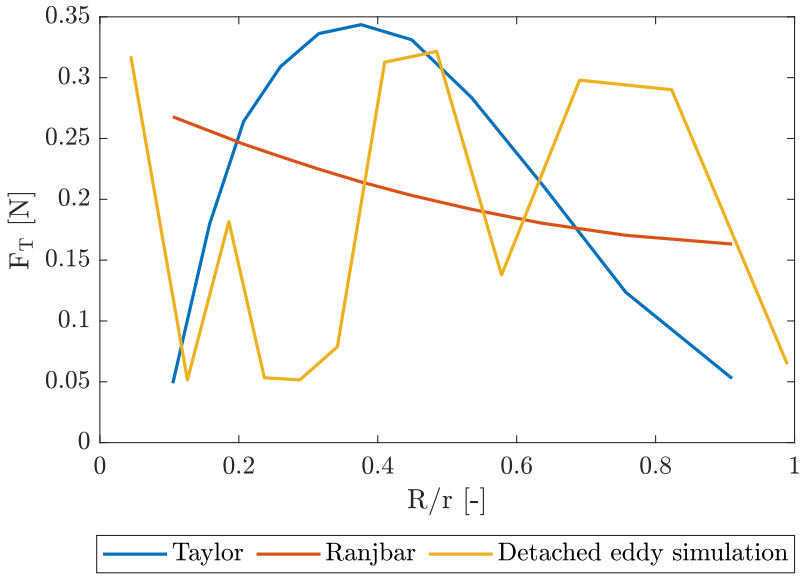

Figure 3.29: *Comparison of modelled thrust force distribution*

While the distribution using the Taylor equations shows an increase in thrust force towards the disc centre, followed by a decrease, the distribution using the Ranjbar equations shows a constant decrease from the disc centre towards the edge of the disc. From the data obtained from DES, a more uneven distribution of forces can be seen, with high forces located at the disc centre and towards the edge. All distributions are within the same order of magnitude, and the total thrust forces are listed in Table 3.8.

Table 3.8: *Total thrust force acting on virtual disk from different methods of modelling the thrust force distribution. Measurements obtained in the experimental campaign by Øye [24] showed a thrust force of 2.16 N acting on the porous disc.*

Method	**Total thrust force [N]**
Taylor equations	2.49
Ranjbar equations	2.35
Detached Eddy Simulation	2.12

3.5 Optimisation

Numerical optimisation is the science of finding the maximum or minimum value of a mathematical function by applying search algorithms [73]. A surrogate-based optimisation (SBO) will be used for maximising the performance of the multi-rotor configuration with seven rotors, within a given set of design variables. The Kriging Surrogate-based optimisation method used in this thesis has been developed by Associate Professor Thomas Hansen at the Western Norway University of Applied Sciences.

Design optimisation involves formulating a mathematical model suitable for resolution through an optimisation algorithm. The optimisation can fail or converge to a solution that is undesirable or unrealistic from an engineering perspective [74]. An optimisation loop is shown in Figure 3.30.

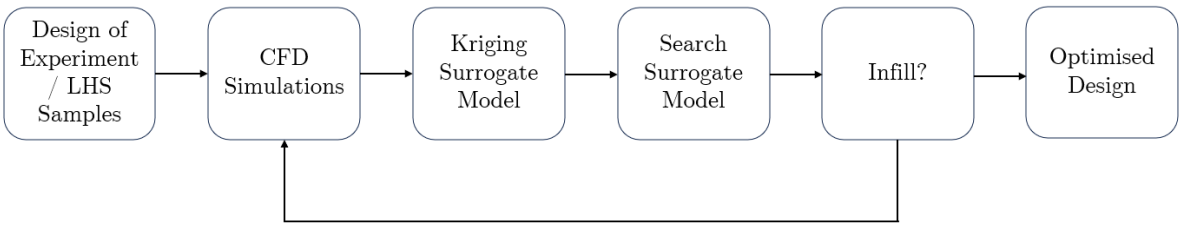

Figure 3.30: *Design optimisation procedure. The first step in the process is to design and validate the CFD simulation model. Once the model accurately reproduces the physics of the problem, the next step in the procedure is initiated. The output from CFD simulations is given to the surrogate model, which searches for the optimal solution. If no optimal solution is found, the model needs refining through an infill point, where in this case a new inter-rotor spacing is suggested. When the surrogate model finds an optimal solution, the procedure comes to an end and the optimised design is obtained. Inspired by Figure 1 in [75].*

The design variables should be independent of each other and any other parameters. The optimiser needs the freedom to select each element independently. This implies that the variables must be input parameters that stay constant throughout the analysis. Another potential problem is defining the design variables as a linear combination of other variables. This can lead to an ill-defined optimisation problem with an infinite number of combinations of design variable values that result in the same design [74]. For the optimisation of maximum performance for the MR configuration, the only considered design variable will be the inter-rotor spacing between rotors.

To find the best design, an objective function is needed. This is a quantity that determines if one design is better than another. The objective function needs to be a single, calculable value for a given set of design variables. Whether the aim is to minimise or maximise the objective function depends on the specific problem [74]. The optimisation of maximum performance will have three different objective functions. First, the objective will be to maximise the power coefficient, for maximising the power output. The second objective will be to maximise the thrust coefficient, as this is beneficial for wake recovery. The third objective will be to minimise the velocity deficit in the wake at a downstream distance of four diameters. Selecting the right objective function is vital for successful design optimisation. Even if the function and its optimal point are computed with precision, if it does not truly reflect the intent of the designer, the mathematical optimum may not align with the optimal solution from an engineering standpoint [74].

The majority of practical design optimisation problems involve enforcing constraints. Similar to the objective function, constraints are determined by a model, and their complexity can vary widely. The feasible region is the set of points that satisfy all constraints. The goal is to minimise/maximise the objective function within this feasible design space [74]. Due to the simplicity of the optimisation of optimal inter-rotor spacing for the multi-rotor configuration for maximising its performance, no constraints will be applied.

The optimisation problem can be defined as

$$\text{minimise} \quad f(x)$$

$$\text{subject to} \quad x_{i,l} \leq x \leq x_{i,u},$$

where x is the inter-rotor spacing between rotors, $x_{i,l}$ and $x_{i,u}$ are the lower and upper bounds for the design variables. For this optimisation problem, the lower bound was set to 0.0, and the upper bound was set to 1.0. There are no constraints present for this optimisation problem, apart from the upper and lower bounds. Three different objective functions will be defined, the optimisation of mean power coefficient, optimisation of mean thrust coefficient and an optimisation of the mean velocity deficit in the wake. The same upper and lower bounds apply for each objective function.

A surrogate model serves as an approximation of a functional output, essentially representing a "curve fit" to an underlying set of data. The primary objective of a surrogate model is to create a model that is considerably quicker to compute than the original function while maintaining sufficient accuracy in relation to known data points. Surrogate-based optimisation (SBO) is a more focused subset within the broader realm of surrogate modelling. Instead of pursuing a globally accurate surrogate, SBO aims for a surrogate model that is accurate enough to guide the optimiser to the true optimum [74]. As the SBO is only an approximation of the function, it needs refining by performing more simulations [73]. These additional simulations are known as infill points. The underlying set of data for this optimisation problem will be the output retrieved from the CFD simulations, which will be the mean power- and thrust coefficients, together with the mean velocity deficit in the wake.

The Kriging surrogate model utilises Latin hypercube sampling (LHS) as the sampling method. This method is built on a random process but is more efficient [74]. The difference between random sampling and LHS sampling is that while the random sampling is completely random, the LHS sampling is memory-based, such that the method ensures a well-spread distribution. The different distributions can be seen in Figure 3.31.

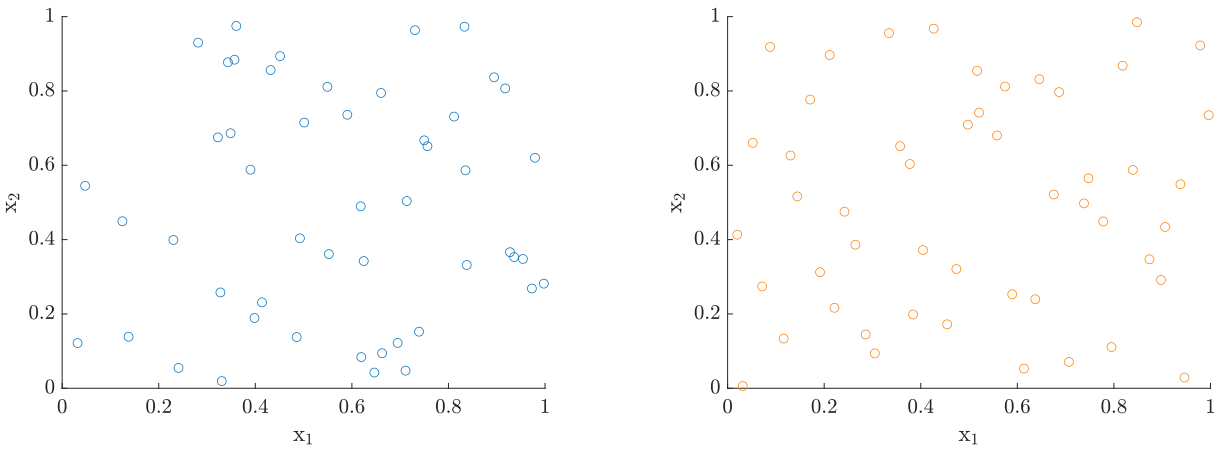

(a) *Random sampling* ***(b)*** *Latin hypercube sampling*

Figure 3.31: *Comparison between random sampling and Latin hypercube sampling. Inspired by Fig. 10.3 in [74].*

For the distribution with random sampling, it can be seen that some points are placed on top of each other, and some areas are poorly covered. For the LHS sampling, a more even distribution of points is seen, and no points are placed on top of each other. The LHS method is based on a Latin square, a concept where one point and one point only exist within any

given row or column [74], as seen in Figure 3.32.

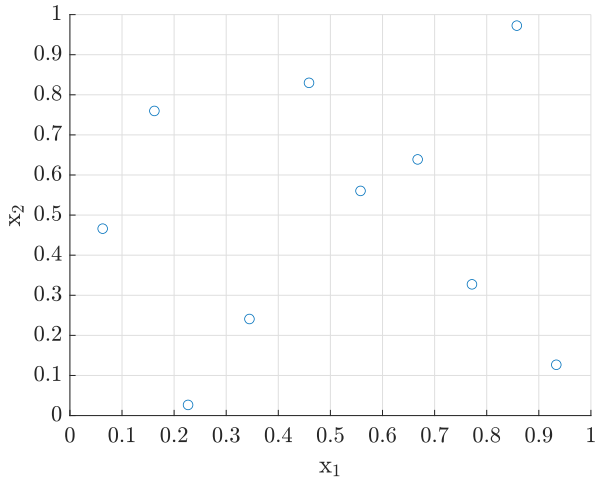

Figure 3.32: *Grid space for LHS*

The Latin square efficiently covers the whole solution space, while embracing all the variations within. When a Latin square is generalised to higher dimensions, it is called a Latin hypercube [74].

As a baseline for the Kriging surrogate model, MR simulations with the maximum and minimum inter-rotor spacings were run in STAR-CCM+. The objective functions, mean C_P, mean C_T and mean velocity deficit for the multi-rotor configuration, were read as the output. The surrogate model was given the inter-rotor spacings and corresponding response from the simulations. Based on the outputs from the CFD simulations, the optimiser was able to determine the next infill point, i.e. the next inter-rotor spacing to be simulated, until the optimal solution was obtained.

It was chosen to maximise the mean values of the power- and thrust coefficients while minimising the velocity deficit in the wake for the different multi-rotor configurations. As discussed in Chapter 2, a higher power coefficient results in higher power generated by the wind turbine. A high power coefficient is also correlated with a high thrust coefficient, and a high thrust coefficient leads to more mixing in the wake. Minimising the velocity deficit in the wake is beneficial for wind farms, as downstream wind turbines will experience higher wind velocities, resulting in higher power outputs. Optimising all of these objective functions will ensure that the whole MR system is performing to its maximum.

As the only parameter being changed between runs is the inter-rotor spacing, the number of degrees of freedom for this optimisation problem is equal to one.

Chapter 4

Results and Discussion

This chapter presents the results obtained from simulations using the virtual disk in STAR-CCM+. It aims to shed light on the obtained results compared to expected results based on the theory given in Chapter 2 and results obtained by others, presented in Section 2.5. Firstly, the results using the porous disc for simulating the single-rotor will be discussed. Then, results from ForWind model wind turbine simulations are presented, before the multi-rotor model will be discussed. Finally, the evaluation of the optimal distance will be presented based on findings from the surrogate-based optimisation.

4.1 Evaluation of SR Model with Porous Disc

Results from the different thrust force modelling approaches discussed in Section 3.4 will be presented throughout this section. As discussed in Section 3.3, an azimuthal resolution of four and a radial resolution of 12 were chosen, together with a normal resolution of one, resulting in a force distribution of 48 points over the virtual disk. Between the input points, the force distribution is interpolated [55], resulting in a force distribution as shown in Figure 4.1.

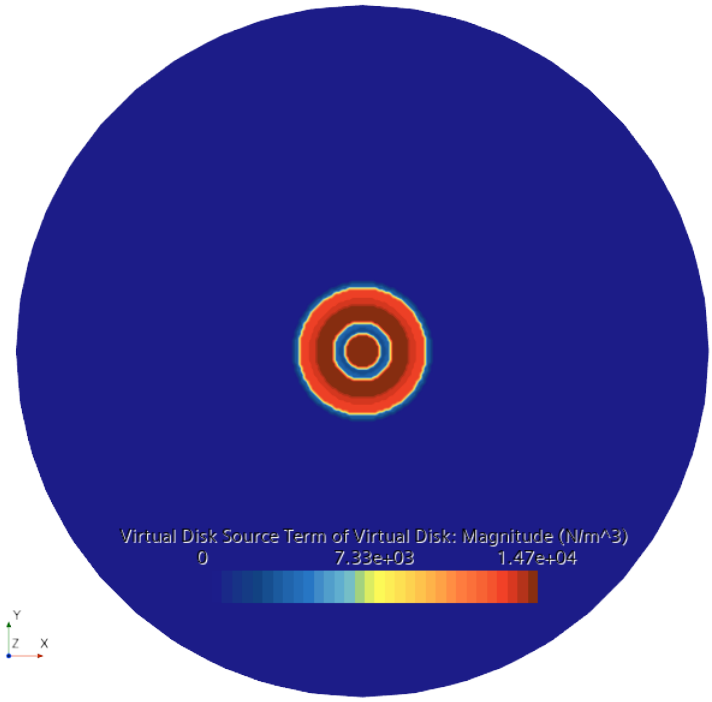

Figure 4.1: *Radial source term distribution in STAR-CCM+ for a single-rotor porous disc simulation. Retrieved from the simulation of the interpolated values from the DES simulation as input.*

The SR model will aim to match the vorticity profile from the Detached Eddy Simulation as shown in Figure 3.25 and the wake measurements taken by Øye [24] for a porous disc, as shown in Figure 2.13.

4.1.1 Taylor Equations

The thrust force obtained from this force distribution was 2.5 N, almost identical to the theoretically calculated thrust force value of 2.49 N using the Taylor equations. Two different turbulence models were tested with this force distribution, the Standard k-ϵ model and the k-ω SST Menter model. Vorticity fields for these simulations are shown in Figures 4.2 and 4.3.

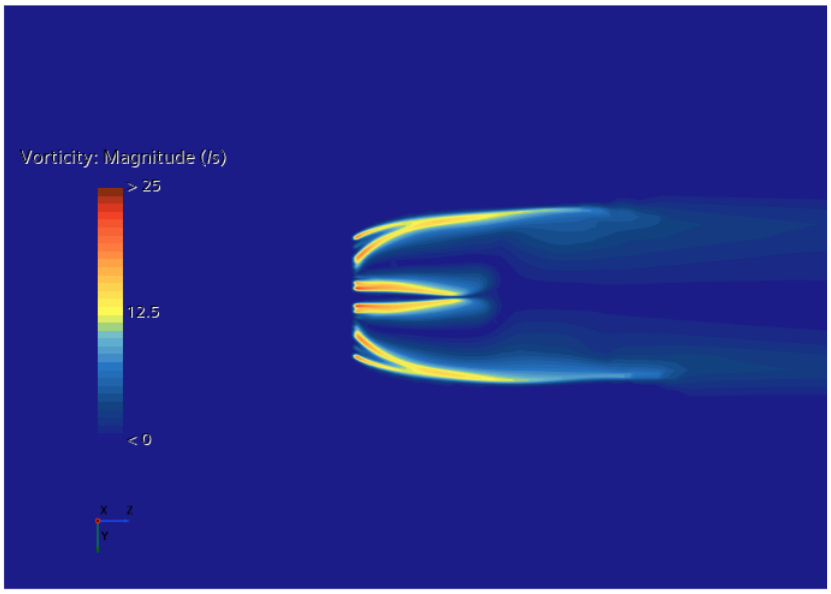

Figure 4.2: *Vorticity field from RANS Standard k-ϵ simulation using calculations from the Taylor equations as input.*

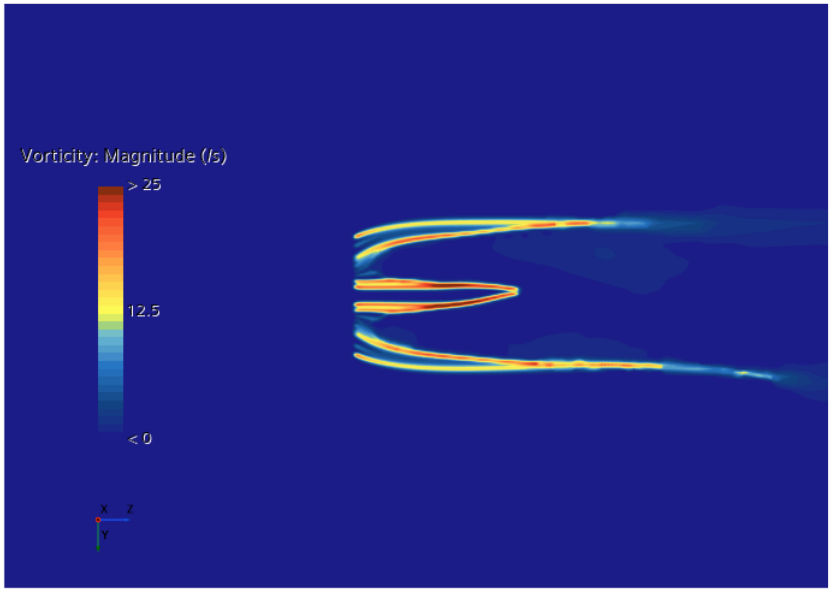

Figure 4.3: *Vorticity field from RANS k-ω SST Menter simulation using calculations from the Taylor equations as input.*

The vorticity profiles match to a certain degree the DES vorticity profile. As they are run with RANS, the accuracy in the wake is reduced, as shown in Bartl and Sætran [76]. It can still be seen that the vortices originating from the root and tip of the rotor are the significant ones. The *k-ω* SST Menter simulation shows a greater magnitude of vorticity than the Standard *k-ϵ* simulation.

A comparison of transverse velocity profiles was also carried out for both the simulation with Standard k-ϵ and the k-ω SST Menter as turbulence models. Experimental data from Øye [24] were used as comparisons at downstream distances of 2d and 4d from the virtual disk. The comparisons is seen in Figure 4.4.

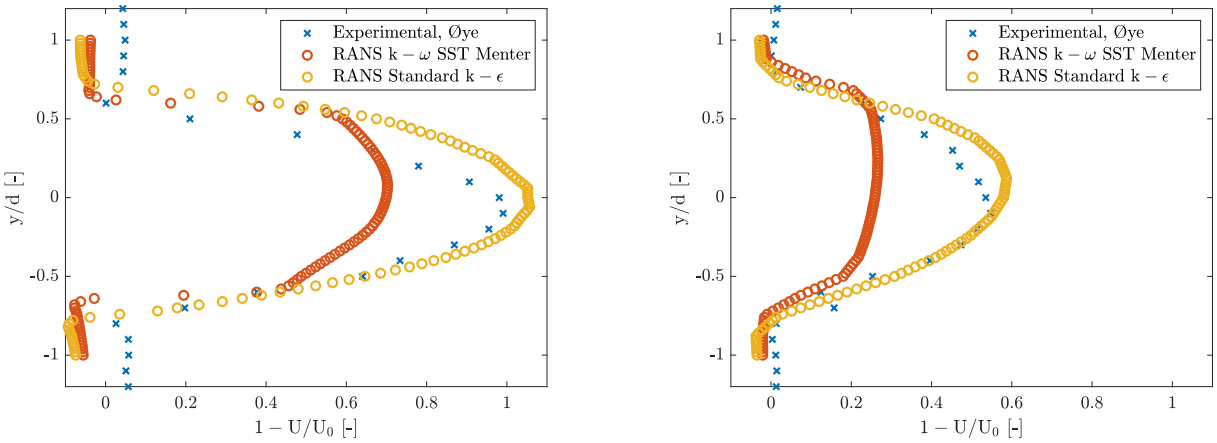

(a) *z/d=2* ***(b)*** *z/d=4*

Figure 4.4: *Normalised velocity profiles from the force distribution modelled with the Taylor equations at downstream distances of 2d and 4d where d equals the porous disc diameter*

It can be seen that the Standard k-ϵ simulation accurately matches the velocity profile at both downstream distances, while the k-ω SST Menter simulation tends to underpredict the velocity deficit at both distances. It can also be seen that for the k-ω SST Menter simulation the velocity profile turns into a top-hat profile and flattens out at 4D downstream.

4.1.2 Ranjbar Equations

Using the equations from Ranjbar et al. [45] a new thrust force was calculated based on the formula for the thrust coefficient C_T in the article. The newly calculated thrust force was 2.35 N. This force distribution were based on the solidity curve. The vorticity field from the Standard k-ϵ simulation can be seen in Figure 4.5.

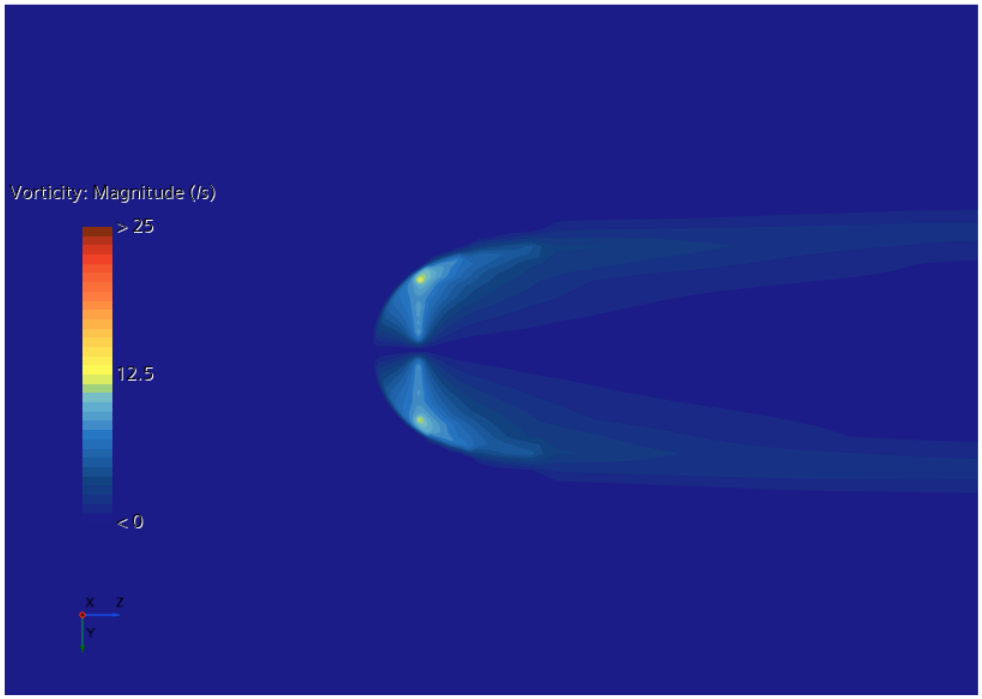

Figure 4.5: *Vorticity field from the RANS Standard k-ϵ simulation using calculations from the Ranjbar equations as input*

The vorticity field for the *k-ω* SST Menter simulation is shown in Figure 4.6.

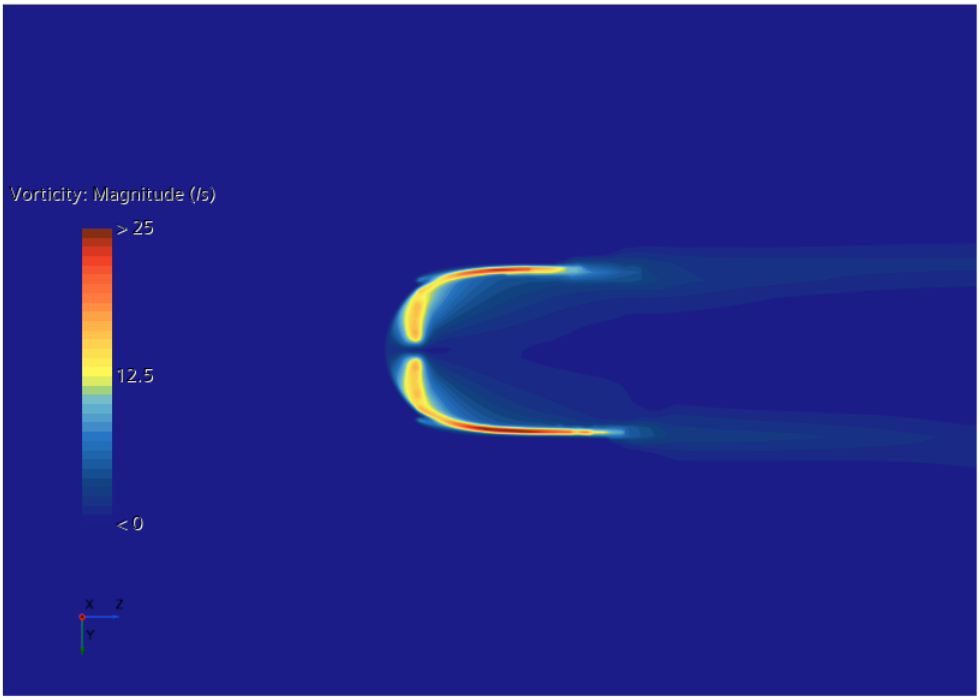

Figure 4.6: *Vorticity field from the RANS k-ω SST Menter simulation using calculations from the Ranjbar equations as input.*

In these simulations, no root vortices are present. It can also be seen that the magnitude of

vorticity is larger for the *k-ω* SST Menter simulation than for the Standard *k-ϵ* as seen in the previous approach as well. Figure 4.7 displays the comparison of normalised velocity profiles from the simulations.

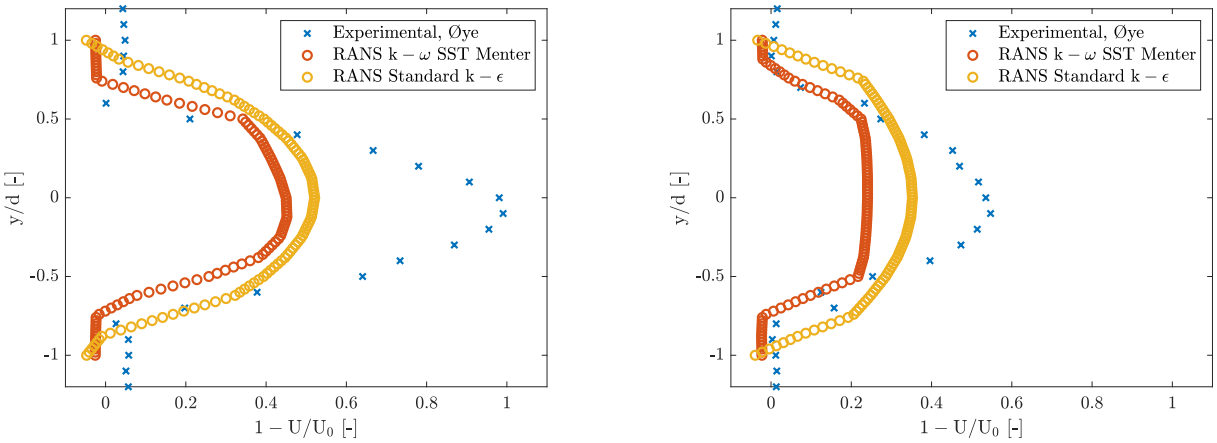

(a) *z/d=2* ***(b)*** *z/d=4*

Figure 4.7: *Normalised velocity profiles from the force distribution modelled with the Ranjbar equations at downstream distances of 2d and 4d where d equals the porous disc diameter*

Both the simulation with the Stanard *k-ϵ* and the simulation with *k-ω* SST Menter underpredict the velocity deficit in the near wake. For these simulations, a thrust force of 1.91 N was measured on the virtual disk in the CFD simulations, somewhat lower than the calculated value of 2.35 N which the input was based on.

Martínez-Tossas et al. [77] discovered that with higher thrust coefficients ($C_T > 0.96$), the streamlines expand near the rotor and then contract, which leads to a faster recovery of the wake. With reduced thrust coefficients, as the airflow passes the rotor, the streamlines widen and continue to expand until the local pressure matches the pressure of the surrounding free stream airflow. Obtained results from simulations using the Taylor (C_T=0.99) and Ranjbar (C_T=0.94) equations are in contradiction with these findings, as simulations using the Ranjbar equations show a lower velocity deficit at both downstream distances.

4.1.3 Data Retrieved from Detached Eddy Simulation

The thrust force measured from the DES was equal to 2.16 N. As with the previous approaches, the Standard *k-ϵ* turbulence model and the *k-ω* SST Menter turbulence model were chosen. The vorticity field from the Standard *k-ϵ* simulation is shown in Figure 4.8

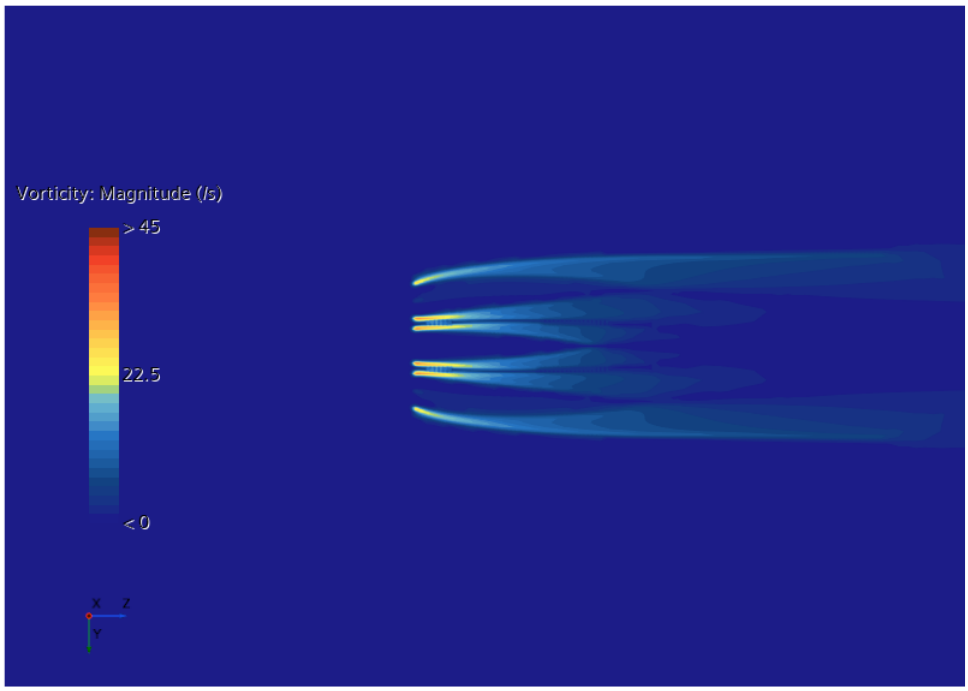

Figure 4.8: *Vorticity field from RANS Standard k-ϵ simulation using data from the Detached Eddy Simulation as input*

The vorticity field of the simulation using the *k-ω* SST Menter turbulence model can be seen in Figure 4.9

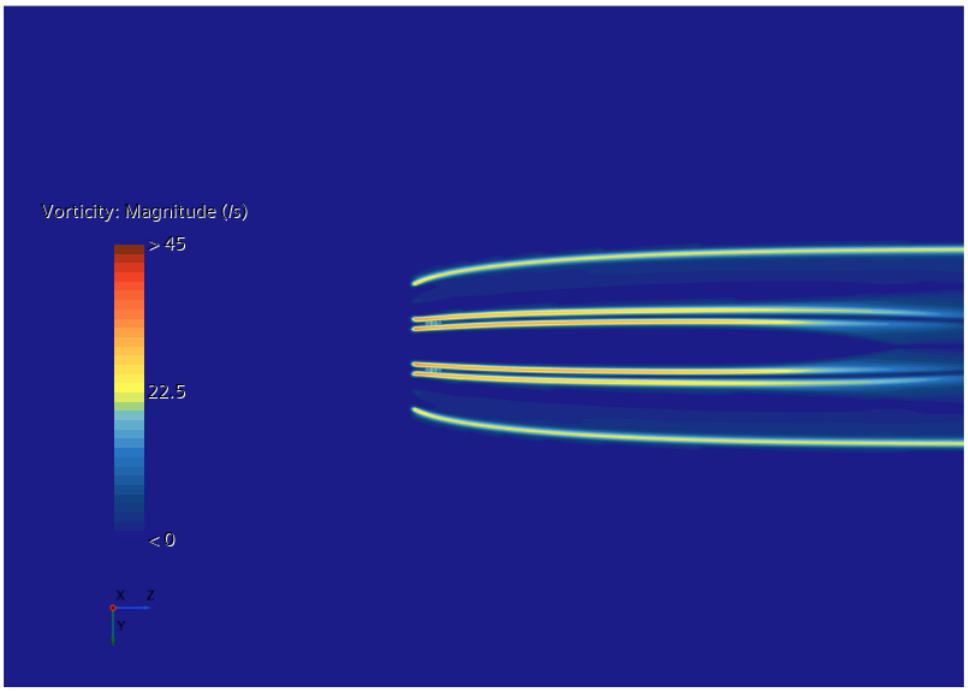

Figure 4.9: *Vorticity field from RANS k-ω SST Menter simulation using data from the Detached Eddy Simulation as input*

Compared with the vorticity field from the DES in Figure 3.25, these vorticity profiles match better than the previous approaches. However, it can be seen that the vorticity originating from the disc centre is higher in these simulations compared to the DES. Compared with the previous approach, it can more clearly be seen where the force distributions come from the disc centre towards the edge.

Studying the normalised velocity profiles in Figure 4.10, it can be seen that a W-shape appears for both turbulence models at a downstream distance of two diameters.

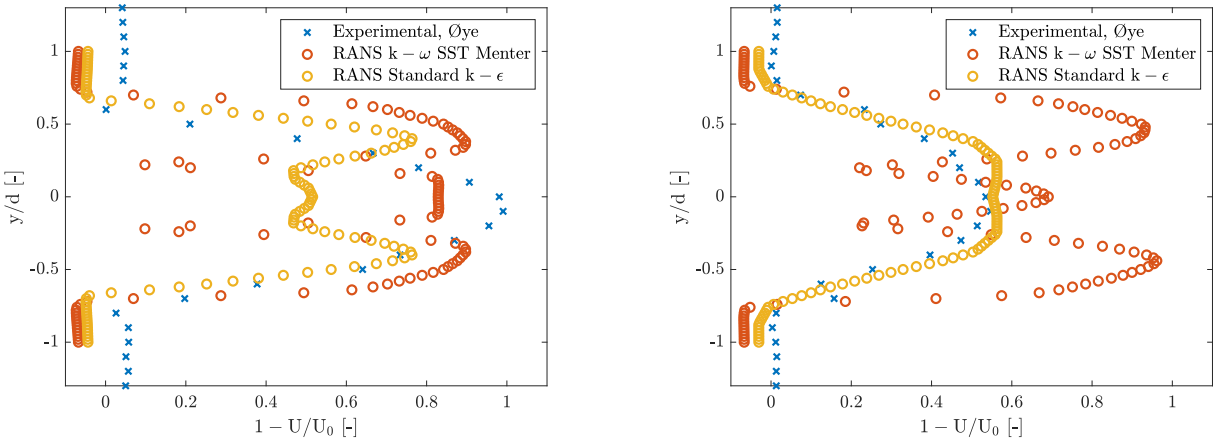

(a) *z/d=2* ***(b)*** *z/d=4*

Figure 4.10: *Normalised velocity profiles from the force distribution modelled with data from the Detached Eddy Simulation at downstream distances of 2d and 4d where d equals the porous disc diameter.*

For the Standard *k-ϵ* simulation, the velocity profile corresponds well with the experimental profile at four diameters downstream, while for the *k-ω* SST Menter simulations the W-shape only magnifies. The W-shape is created by the strong vortices originating from the disc centre for these simulations. Based on the vorticity profiles, the magnitude of the vorticity is lower for the Standard *k-ϵ* simulation, which leads to it reaching a Gaussian velocity profile at 4d downstream, where the *k-ω* SST Menter velocity profile still maintain the W-shape.

4.2 Evaluation of SR Model with Model Wind Turbine

Simulations of the ForWind model wind turbine have been performed and compared mainly to experimental data from Neunaber [25]. The obtained results from the CFD RANS simulations will also be evaluated against expected results based on the theory explained in Chapter 2.

Comparisons of wake profiles from experiments and RANS 1D Momentum method CFD simulations using the *k-ω* SST Menter as turbulence model at different downstream locations of the model wind turbine are shown in Figure 4.11.

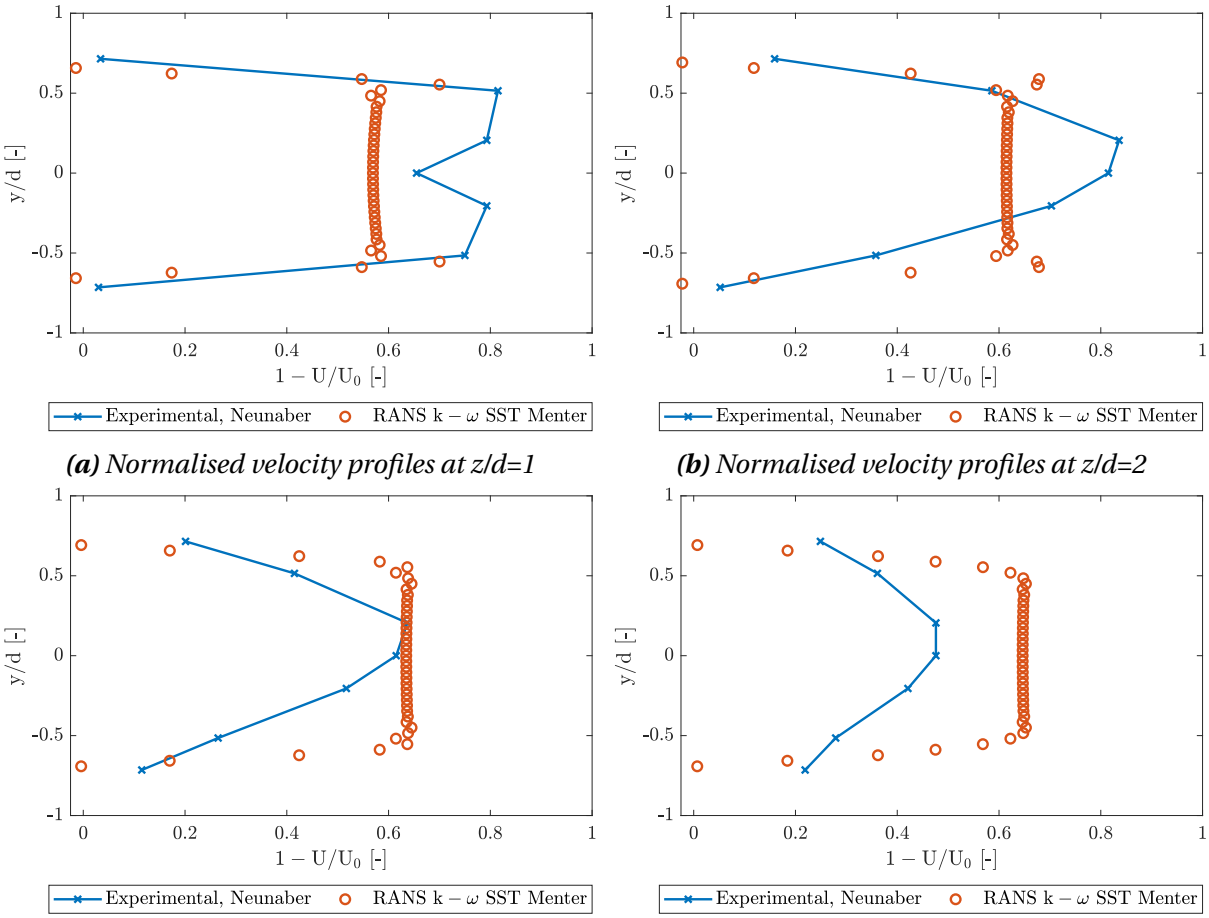

(a) *Normalised velocity profiles at z/d=1*

(b) *Normalised velocity profiles at z/d=2*

(c) *Normalised velocity profiles at z/d=3*

(d) *Normalised velocity profiles at z/d=4*

Figure 4.11: *Normalised velocity profile comparisons at different downstream locations, d equals the diameter of the ForWind model wind turbine.*

At a distance of one diameter downstream, the width of the simulation wake corresponds well with that of the experimental wake and has similar trends even though the velocity deficit is higher for the experimental wake. At two diameters downstream the experimental wake changes form from a "top-hat" like shape, towards a Gaussian shape. From 2d to 4d it can be seen that the experimental velocity increases, while the simulation wakes velocity slightly decreases as the flow propagates downstream. Studying the trend for the simulation wake at 4d, a Gaussian shape may be developing, but is impossible to determine. It can be concluded that the velocity in the simulation struggles to recover as it propagates downstream, likely due to the simplifications in the turbulence modelling.

A different view on the velocity development downstream is shown in Figure 4.12.

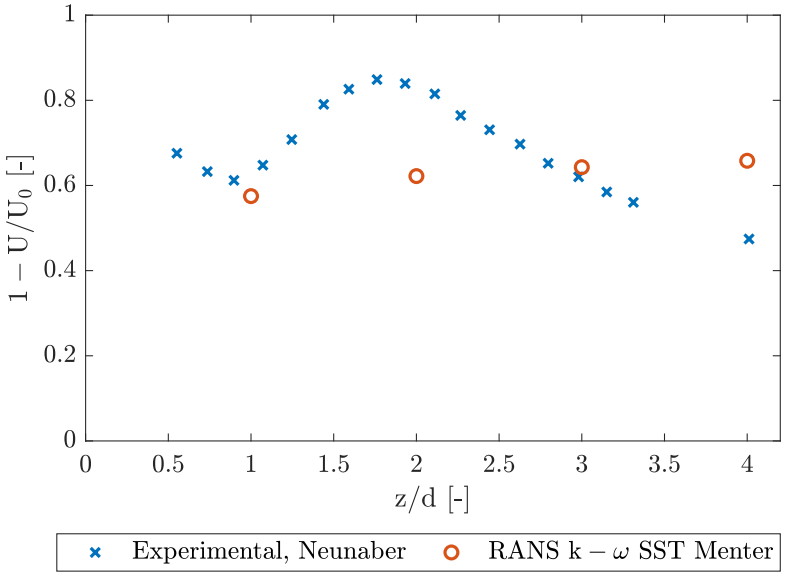

Figure 4.12: *Normalised mean velocity comparison at centerline distances downstream (z/d) of the ForWind MWT between experimental data obtained by Neunaber and RANS CFD simulations.*

Figure 4.12 shows that the simulations match the experiments at 1d and 3d downstream, but do not match at 2d and 4d. It can also be seen that for the experimental data, the velocity deficit increases from 1d to 2d, but then it decreases thereafter. For the CFD simulations, the velocity deficit increases, following a linear path from 1d to 4d. This is most likely due to computational limitations as discussed in Section 3.1.5. The RANS model does not resolve any of the eddies in the wake, they are only modelled [28].

As RANS simulations are accurate in predicting the flow around the rotor and less precise in the wake, as shown in [76], the thrust and power acting on the rotor were compared between simulations in STAR-CCM+ and QBlade. These are summarised in Table 4.1.

Table 4.1: *Comparison of simulated wind turbine characteristics*

Parameter	**STAR-CCM+**	**QBlade**	**Similarity**
C_P [-]	0.31	0.307	96.8 %
C_T [-]	1.0042	1.0042	100 %
Power [W]	21.02	20.75	98.7 %
Thrust [N]	9.08	9.05	99.7 %

Figure 4.13 displays the velocity field from the single-rotor (SR) simulations using the ForWind

turbine. The turbulence model in this simulation was the *k-ω* SST Menter model.

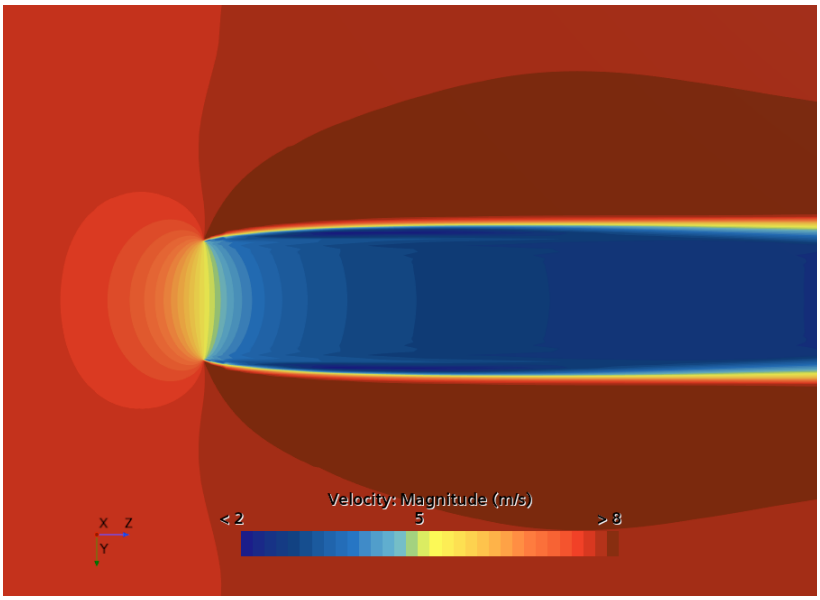

Figure 4.13: *Velocity field for SR RANS simulation with k-ω SST Menter as turbulence model.*

For the simulation in Figure 4.13 an inlet speed of $U_0 = 7.5$ m/s was applied. It can be seen that the model follows the physics from the one-dimensional momentum theory, with the velocity slowing down in front of the rotor because of the thrust force acting on the incoming flow. However, greater interaction and mixing between the wake flow and the free stream velocity was expected. A greater expansion of the wake was also expected, as seen in Figure 2.11. The pressure field in Figure 4.14 corresponds well with the theory of a pressure increase upstream of the rotor and a sudden decrease immediately behind the rotor.

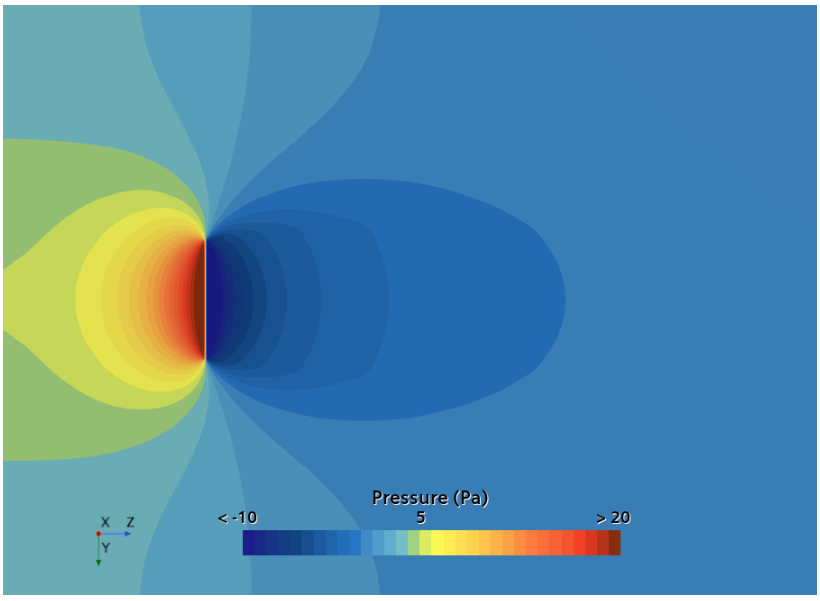

Figure 4.14: *Pressure field for SR RANS simulation with k-ω SST Menter as turbulence model*

How the velocity and pressure are affected by the presence of the virtual disk is presented in Figure 4.15 as well.

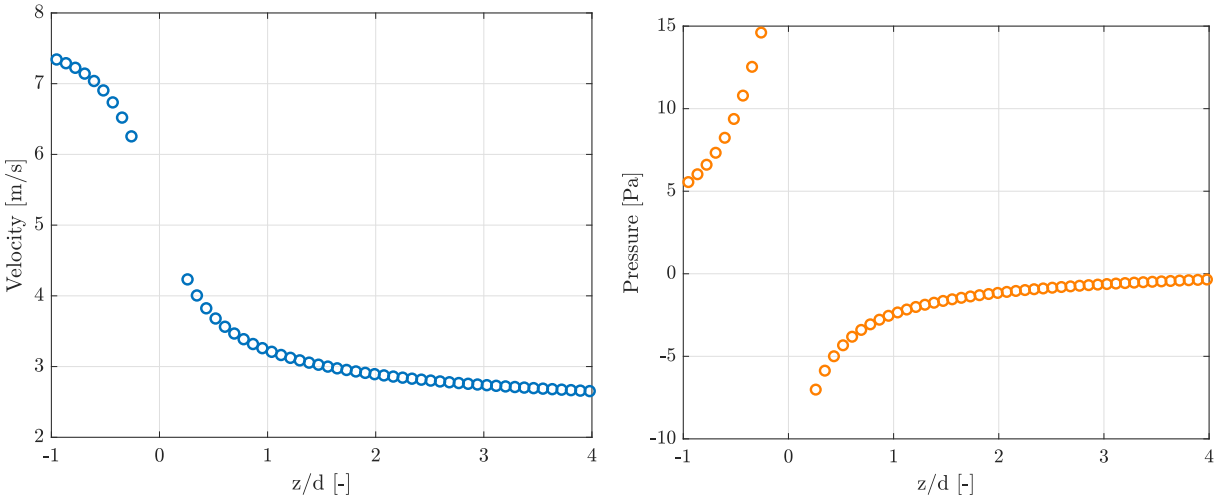

(a) *Velocity drop over rotor*

(b) *Pressure drop over rotor*

Figure 4.15: *Velocity and pressure drop over the virtual disk located at z/d=0, d equals the ForWind MWT diameter.*

These results are in great agreement with Figure 2.4 from Section 2.2.

The SR simulations have shown that the CFD simulation model is capable of accurately predicting the flow around the rotor. However, the model is less capable of capturing the wake mixing and velocity recovery in the wake. These results are consistent with other studies such as Bartl and Sætran [76]. It was shown here that RANS models are capable of capturing the thrust and power on an upstream turbine, but challenges appeared in predicting the kinetic energy in the wake. To accurately capture the wake flow, more complex models are needed, such as DES or LES.

4.3 Evaluation of Multi-Rotor Model

The multi-rotor (MR) simulation model consists of virtual disks with the same settings as the single-rotor (SR) simulation model using the ForWind MWT data and the 1D momentum method. As there is no MR module available in STAR-CCM+, the virtual disk from the SR model has been used to build an MR simulation model. The MR simulation model has been compared against experimental results with inter-rotor spacings of s/d=0.0, s/d=0.1 and s/d=0.4. The different MR configurations can be seen in Figure 4.16.

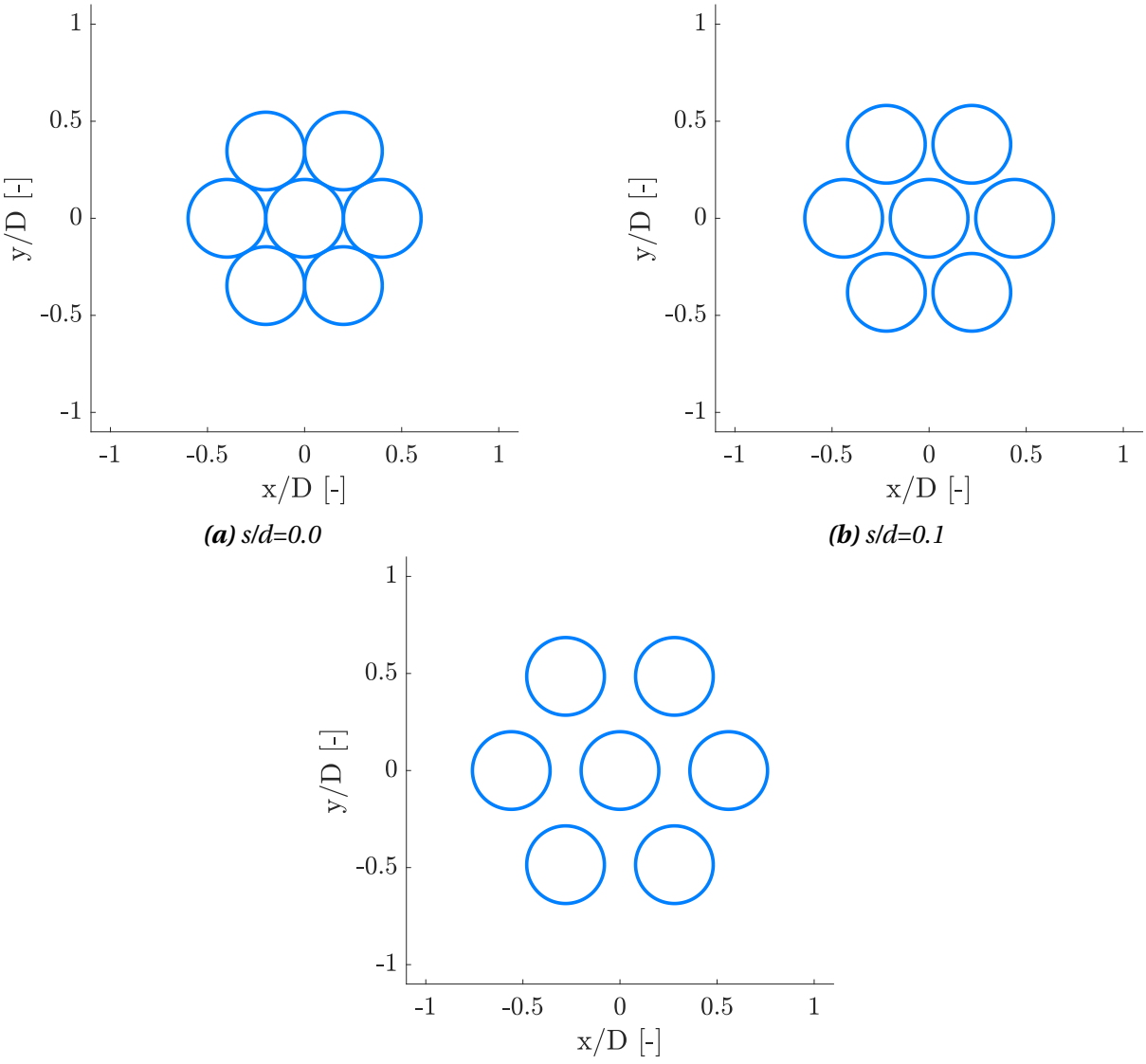

(a) *s/d=0.0*

(b) *s/d=0.1*

(c) *s/d=0.4*

Figure 4.16: *MR7 configurations with different inter-rotor spacings. As physical experiments have been conducted using these spacings [21][23], comparisons between experiments and numerical simulations will be performed using these inter-rotor spacings.*

For these inter-rotor spacings, several physical experiments have been performed using porous discs, such as Koi [21] and Skoland [23]. Although the CFD simulations are performed using a model wind turbine instead of a porous disc, trends between experiments and numerical simulations for different spacings can be used for comparison.

The thrust force measurements obtained by Koi [21] on the centre actuator disc in the multi-rotor setup are being compared with results from the RANS CFD simulations in Table 4.2.

Table 4.2: *Comparison of measured thrust force on the centre disc between Koi [21] and MR CFD simulations. It should be remembered that Koi used porous discs while the CFD simulations were performed using data from a model wind turbine. The trends will be compared.*

Model	**Thrust force from Koi [N]**	**Thrust force from CFD [N]**
MR7 s/d=0.0	2.59 ± 0.02	7.92
MR7 s/d=0.1	2.53 ± 0.02	7.96
MR7 s/d=0.4	2.45 ± 0.02	8.06

While measurements from Koi [21] show a decrease in the thrust force acting on the centre disc with increasing inter-rotor spacing, the CFD simulations show the opposite. For the CFD simulations, it can be seen that the thrust force increases with increasing spacing between rotors. The same applies to the thrust coefficient as well for both the centre disc and the edge discs. While the thrust coefficients from Koi [21] decrease with increased spacing, the thrust coefficients from the CFD simulations tend to increase with increased spacing. However, given the small differences in the experimentally measured and numerical simulated thrust forces, the trends are within the same range.

The velocity deficit from the CFD simulations in the induction zone of the virtual disk is shown in Figure 4.17, and compared against induction zone measurements from Koi [21] in Figure 4.18.

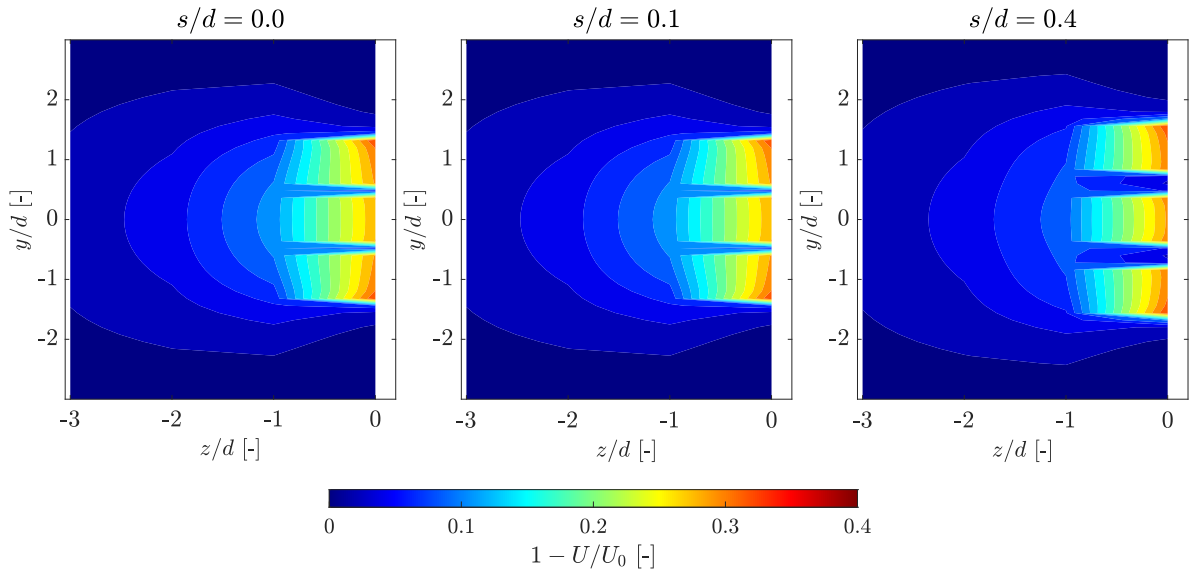

Figure 4.17: *Normalised velocity deficit in the induction zone from RANS CFD simulations.*

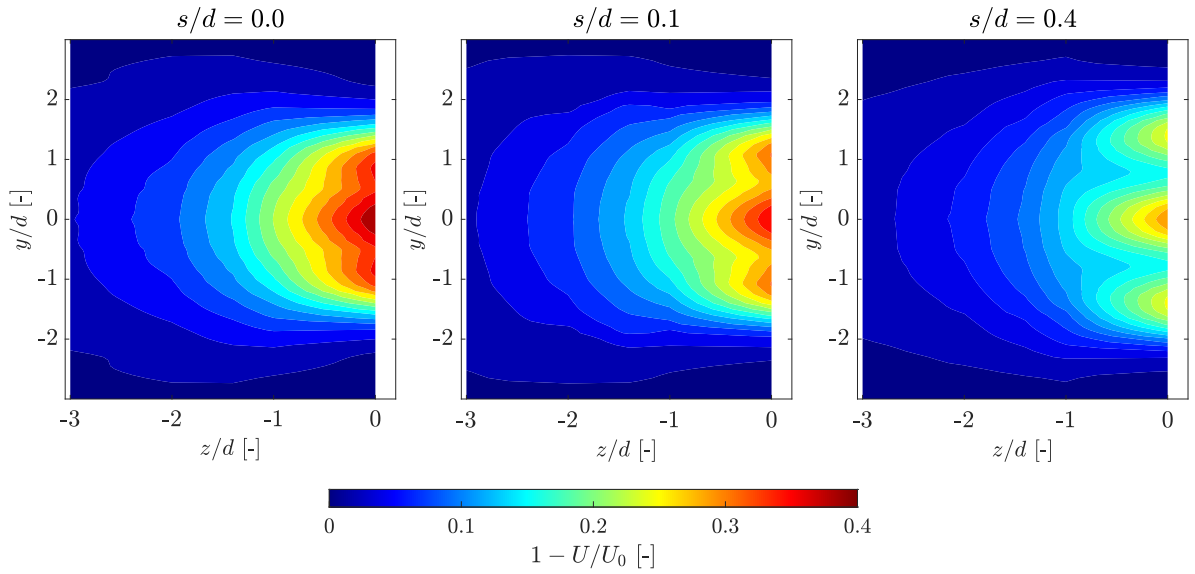

Figure 4.18: *Normalised velocity deficit in the induction zone from experimental data obtained by Koi [21].*

The findings of Koi [21] illustrate that a higher velocity deficit is experienced in the induction zone in front of the centre disc. For the CFD simulations, less variation in velocity deficit is observed between discs. The velocity reduction increases with increasing blockage ratios [21], clearly seen in the experimental induction zone. Less reduction in velocity is seen in the CFD simulations, where the velocities remain similar for every tested inter-rotor spacing. From the experimental data, clear interaction and mixing are present in the induction zone between the individual rotor ahead flows, while for the CFD simulations, less interaction is observed between the upstream rotor flows.

Comparison of normalised velocity deficit in the wake is compared with Skoland [23] for inter-rotor spacings of s/d=0.0, s/d=0.1 and s/d=0.4. The comparison of normalised velocity deficit for an inter-rotor spacing of s/d=0.0 is presented in Figures 4.19 and 4.20.

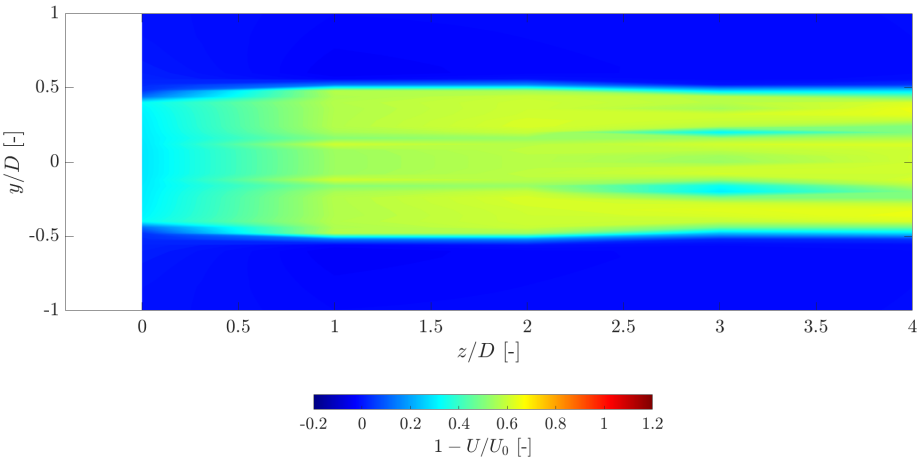

Figure 4.19: *Normalised velocity deficit field from RANS CFD simulations with an inter-rotor spacing of s/d=0.0.*

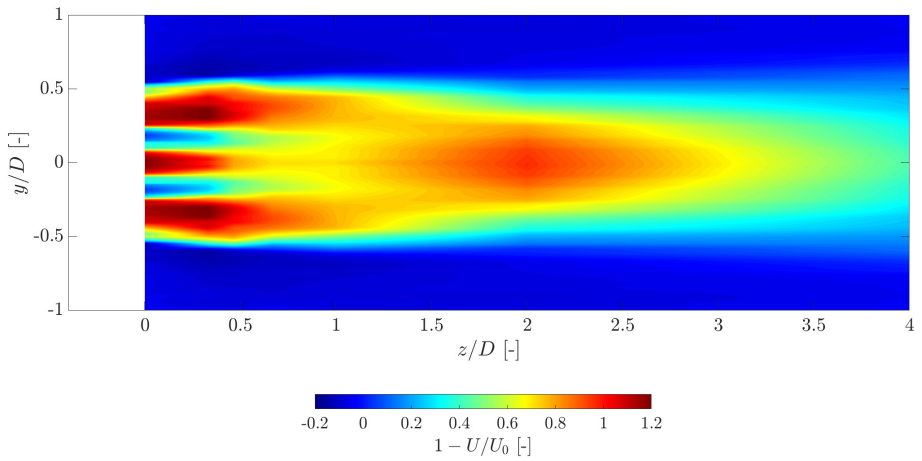

Figure 4.20: *Normalised velocity deficit measurements from Skoland [23] with an inter-rotor spacing of s/d=0.0*

For the experimental wake, a larger velocity deficit is present in the immediate near wake, compared to the velocity deficit of the CFD simulation. Even though the velocity deficit is larger in the experimental wake, the recovery as the flow propagates downstream is faster. For the CFD simulation, the velocity deficit remains almost constant from the rotor plane and far downstream. The lack of recovery for the CFD simulations was also present in the

single-rotor simulations. Figures 4.21 and 4.22 display the wake comparisons from simulation and experiment respectively with an inter-rotor spacing of s/d=0.1.

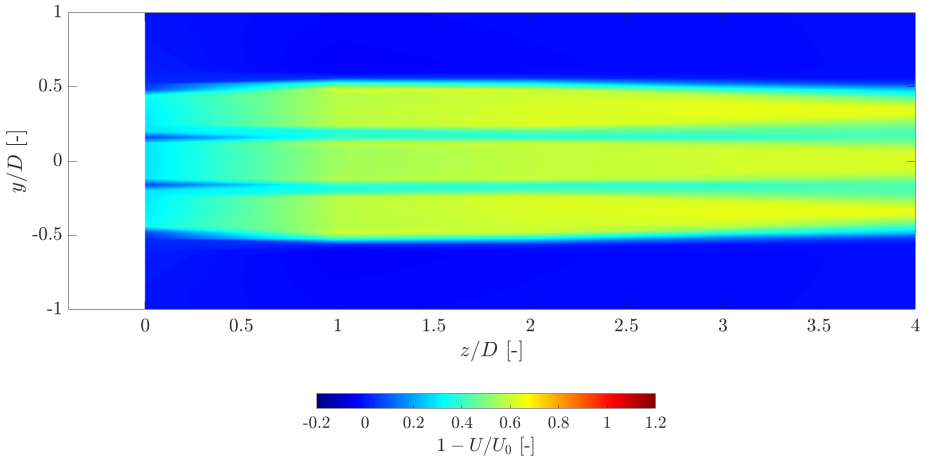

Figure 4.21: *Normalised velocity deficit measurements from RANS CFD simulations with an inter-rotor spacing of s/d=0.1.*

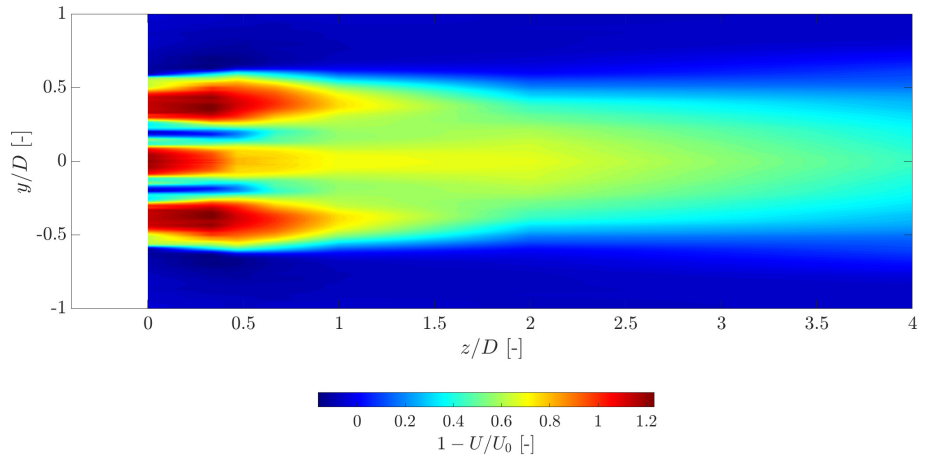

Figure 4.22: *Normalised velocity deficit measurements from Skoland [23] with an inter-rotor spacing of s/d=0.1*

When the spacing between rotors is increased to s/d=0.1, a faster wake recovery is present for the experimental measurements, but less recovery is seen in the CFD simulations. Similar to an inter-rotor spacing of s/d=0.0, the CFD simulations struggle when it comes to wake recovery and mixing between the individual rotor wakes. As also seen with a spacing of s/d=0.0, the velocity deficit in the experimental wake is higher and recovering faster. It can also be seen that the mixing of individual wakes occurs already at one diameter downstream for the experimental wake, while for the simulation wake, they are independent of each other

across the entire simulated domain. Figures 4.23 and 4.24 displays the velocity deficits when the inter-rotor spacing increase to s/d=0.4.

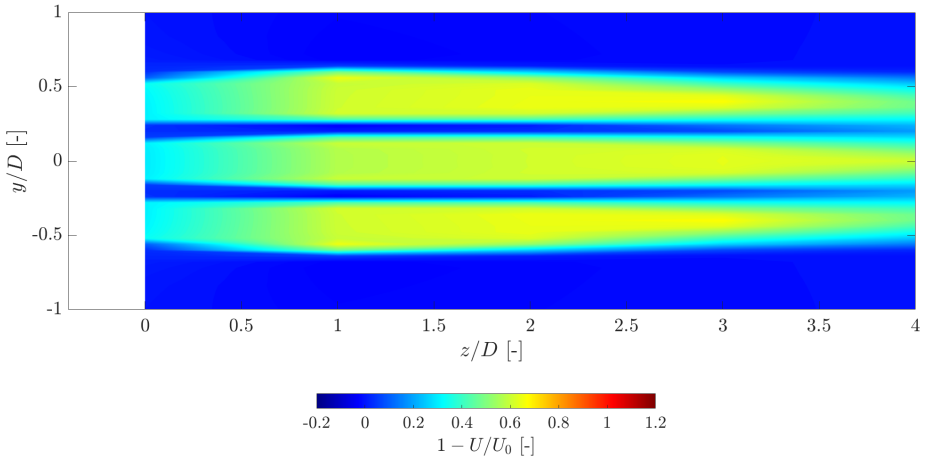

Figure 4.23: *Normalised velocity deficit measurements from RANS CFD simulations with an inter-rotor spacing of s/d=0.4.*

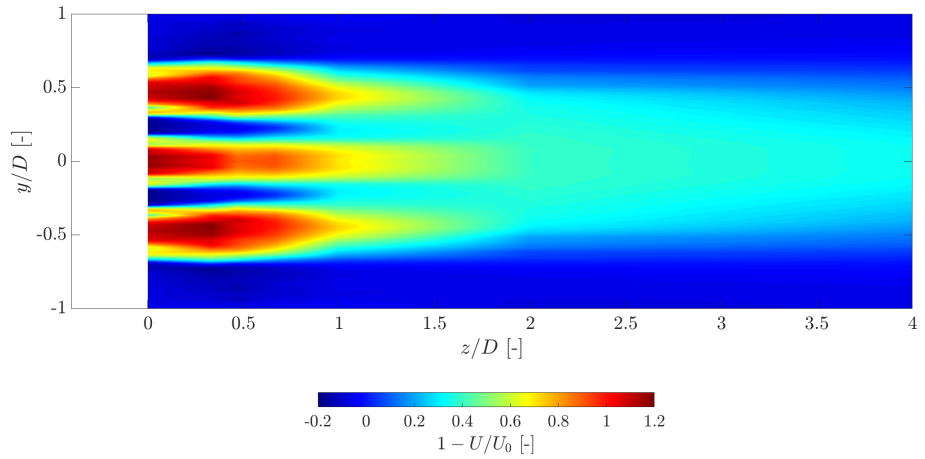

Figure 4.24: *Normalised velocity deficit measurements from Skoland [23] with an inter-rotor spacing of s/d=0.4*

For an inter-rotor spacing of s/d=0.4, the wake recovers faster for both the CFD simulation and the experimental campaign. However, as with the previous inter-rotor spacings, the velocity recovers at a shorter distance downstream for the experimental measurements compared to the CFD simulations. Trends for increased velocity recovery in the wake of an increasing inter-rotor spacing correspond well between experiments and simulations. As more free stream air is allowed to pass through, this allows for greater mixing with the rotor wakes, resulting in a faster wake recovery.

A comparison of velocity deficit profiles between experimental data from Skoland [23] and RANS simulations in CFD with an inter-rotor spacing of s/d=0.1 are shown in Figure 4.25.

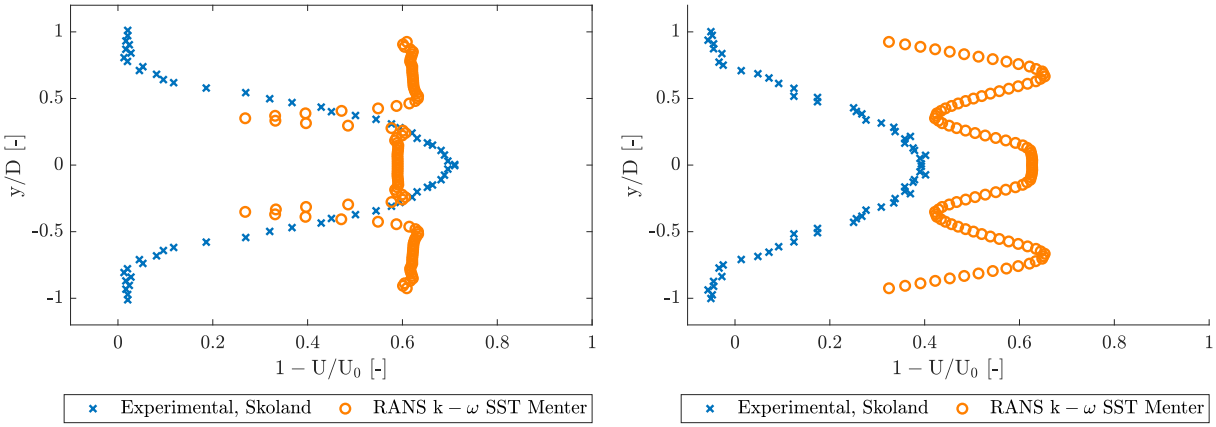

(a) *Normalised velocity deficit profile at 2D*

(b) *Normalised velocity deficit profile at 4D*

Figure 4.25: *Comparison of normalised lateral velocity profiles from Skoland [23] and RANS CFD simulations using the k-ω SST Menter turbulence model with an inter-rotor spacing of s/d=0.1. D represents the total diameter for the individual multi-rotor system.*

Comparison between Skolands lateral wake profiles with the CFD simulations in Figure 4.25 indicate that the wake mixing in the simulation model is poor compared to experiments. The two distinct peaks present in the velocity profiles are between rotors where the free stream velocity passes through. For the experimental measurements by Skoland, these entrances of free stream velocity quickly mix with the rotor wake to create the Gaussian shape as seen in Figure 4.25. It can also be seen that the velocity deficit decreases from 2D to 4D for the experimental wake, while for the simulation wake it slightly increases from 2D to 4D.

Figure 4.26 further illustrates the lack of mixing between the rotor wakes and the free stream velocity entering between the rotors. Instead of mixing and dissipating downstream, the wake profiles become cylindrical behind the individual rotors.

Figure 4.26: *Isosurface velocity profile for MR7 with s/d=1.0. The lack of mixing between individual rotor wakes is presented.*

Looking back at Equation 2.6 from Chapter 2, given as

$$\Delta p_r = p_r^+ - p_r^- = \frac{1}{2}\rho(U_0^2 - u_w^2),$$

the pressure difference across the rotor is dependent on the velocity in the wake and upstream of the rotor. This pressure difference directly affects the thrust force acting on the rotor as seen in Equation 2.10

$$F_T = \Delta p \cdot A_r,$$

which again affects the power output given by

$$P = F_T \cdot u_r.$$

Deviating results in thrust measurements by Koi [21] can be explained by the wake velocity effect on the thrust force acting on the rotor in the CFD simulations. As seen in the simulations, the wake mixing and recovery are not modelled well by the simulations. Deviations in the wake flow may lead to consequential errors in the simulated thrust force and further in the simulated power output from the rotor.

4.4 Evaluation of Optimal Distance

After evaluating the simulations performed on the multi-rotor system with different inter-rotor spacings, the output from the simulations was used as input for the Kriging surrogate model. The objective functions to maximise for the optimisation model were the power- and thrust coefficients, as well as to minimise the velocity deficit at a distance of four diameters downstream in the wake. Optimisation of these parameters will ensure that the multi-rotor system is performing to its maximum. Figure 4.27 displays the outcome from the optimisation of the power coefficient.

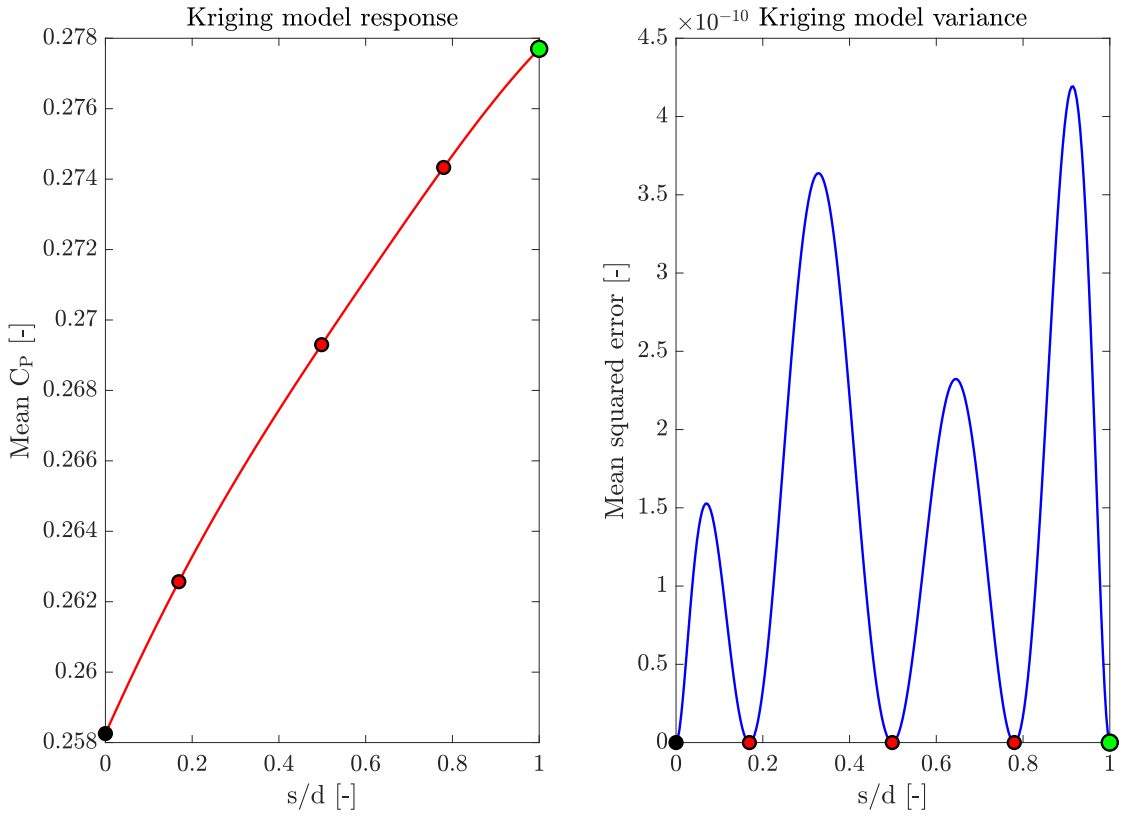

Figure 4.27: *Outcome of optimisation of power coefficient. On the left side, the solution space for the optimisation is shown. The infill points for different inter-rotor spacings with their parametric value are shown along with the discovered optimal spacing indicated with a green dot. On the right the mean squared error for the optimisation is shown, indicating the accuracy of the solution.*

Evaluation of the results from the optimisation indicates that the optimal inter-rotor spacing for maximising the power coefficient is s/d=1.0. From s/d=0.0 to s/d=1.0 the mean power coefficient increases by 0.02, representing a 7.8 % increase in mean power coefficient. The variance or uncertainty in the right plot indicates with an order of magnitude of X^{-10} that the solution found is indeed the optimal one. For this MR setup, each rotor operates almost

without any effect from the other rotors. The power coefficient acting on each virtual disk (VD) is shown in Figure 4.28.

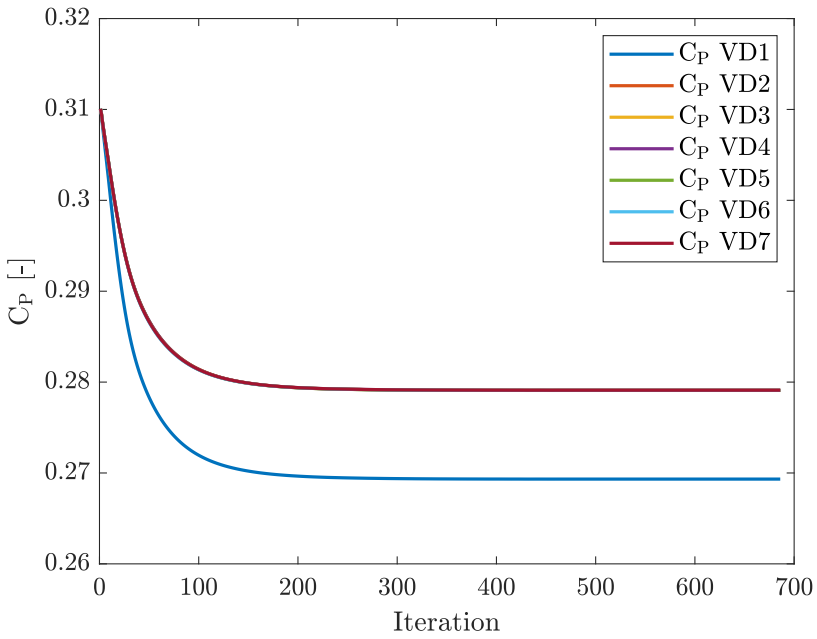

Figure 4.28: *Individual C_P curves. VD1 is the centre virtual disk in the MR setup. It can be seen that the centre virtual disk has a lower power coefficient than the others, which all lay on top of each other.*

The power coefficient curve for the centre disc lies under the rest of the power coefficient curves. As discussed in Section 4.3 the outer discs experience higher forces than the centre disc.

An optimisation of the thrust coefficient was also performed. The same infill points were used as in the power coefficient optimisation, to have enough samples for the optimiser to find the next infill point for the thrust coefficient optimisation. The results from optimising the thrust coefficient are seen in Figure 4.29.

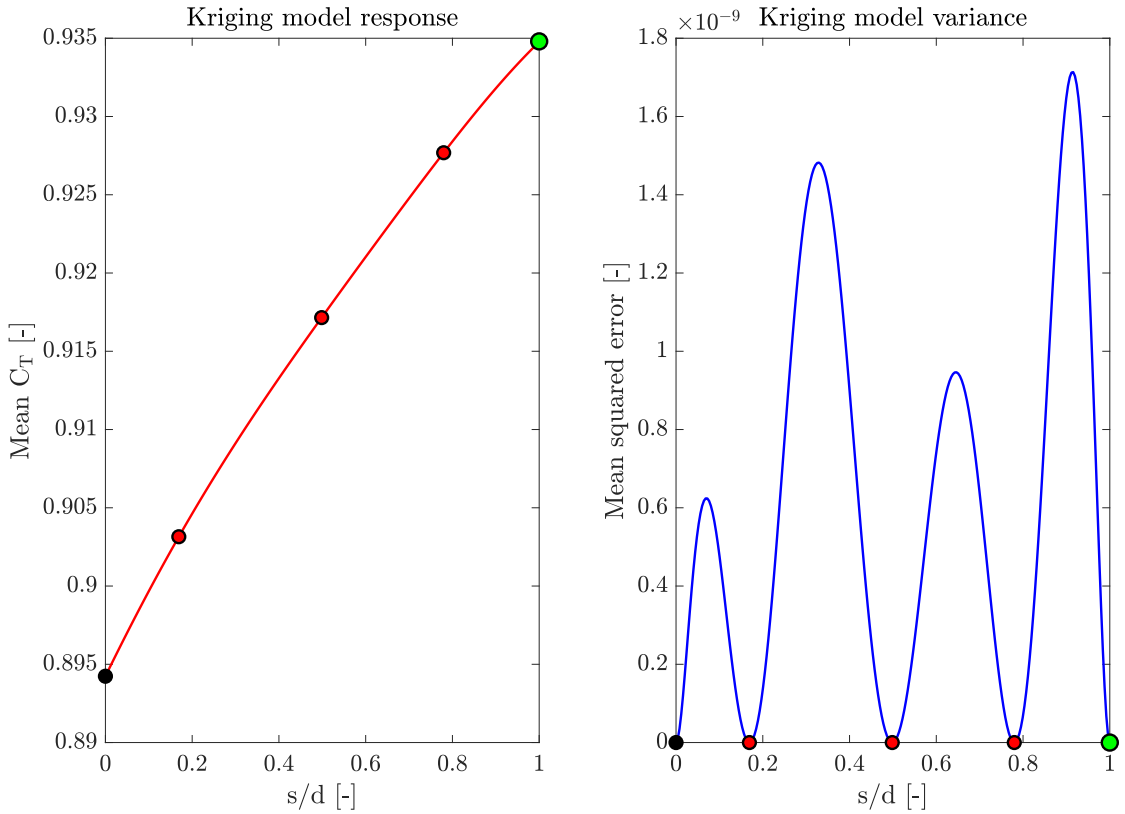

Figure 4.29: *Outcome of optimisation of thrust coefficient. On the left side, the solution space for the optimisation is shown. The infill points for different inter-rotor spacings with their parametric value are shown along with the discovered optimal spacing indicated with a green dot. On the right the mean squared error for the optimisation is shown, indicating the accuracy of the solution.*

The inter-rotor spacing of s/d=1.0 also gave the best results for maximising the mean thrust coefficient of the MR7 system. An increase in the mean thrust coefficient of 3.7 % was recorded between s/d=0.0 and s/d=1.0. The thrust coefficient acting on each virtual disk is shown in Figure 4.30.

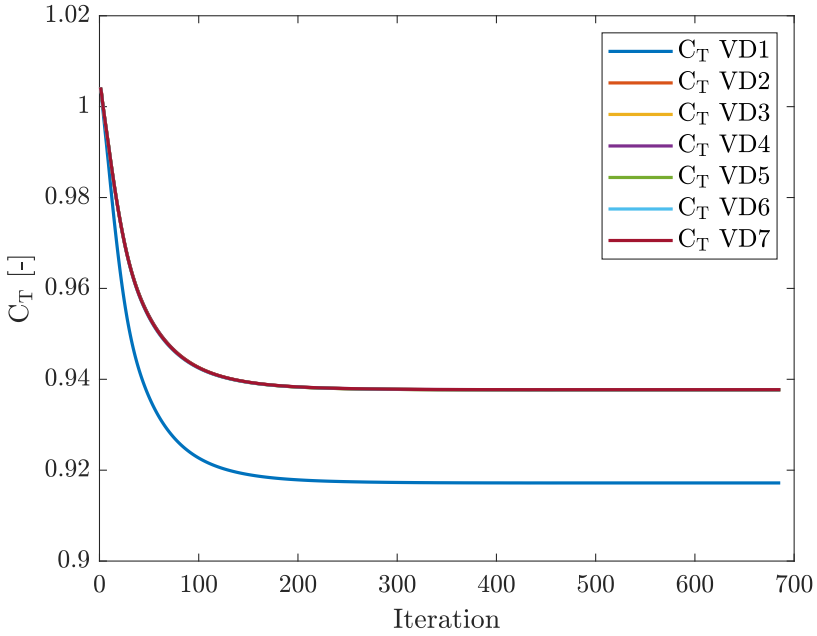

Figure 4.30: *Individual C_T curves. VD1 is the centre virtual disk in the MR setup. Similar to the C_P curves, it can be seen that the centre virtual disk has a lower thrust coefficient than the others, which all lay on top of each other.*

Unlike the other two optimisations, the optimisation of velocity deficit was chosen to minimise instead of maximise. It is desirable with a minimal velocity deficit in the wake such that the downstream wind turbines can extract the most amount of energy from the wind. The optimisation of minimal velocity in the wake at a distance of four diameters downstream is shown in Figure 4.31.

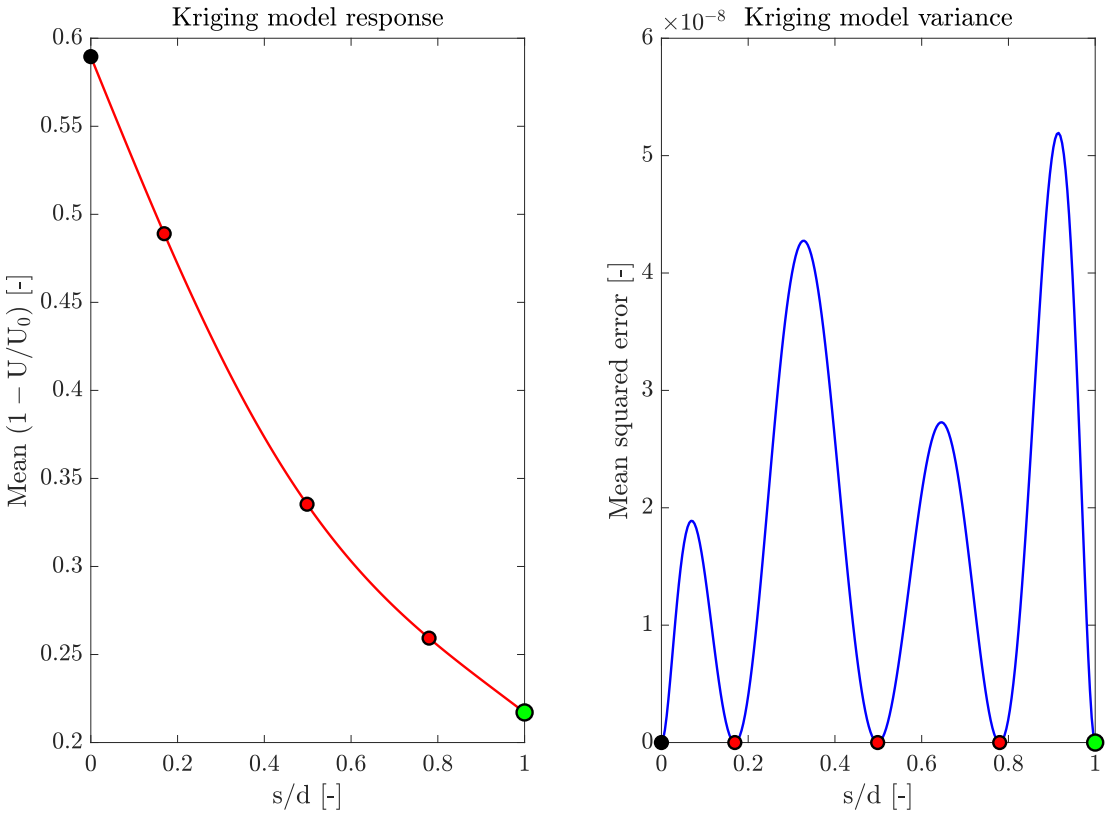

Figure 4.31: *Outcome of the optimisation of the velocity deficit. On the left side, the solution space for the optimisation is shown. The infill points for different inter-rotor spacings with their parametric value are shown along with the discovered optimal spacing indicated with a green dot. On the right the mean squared error for the optimisation is shown, indicating the accuracy of the solution.*

A line probe placed at four diameters downstream with equal length as the total diameter for that particular MR system was used to determine the mean velocity deficit. 100 points were sampled at this distance, and the mean value was calculated.

The velocity deficit profile for the optimal inter-rotor distance concerning optimal wake velocity is shown in Figure 4.32.

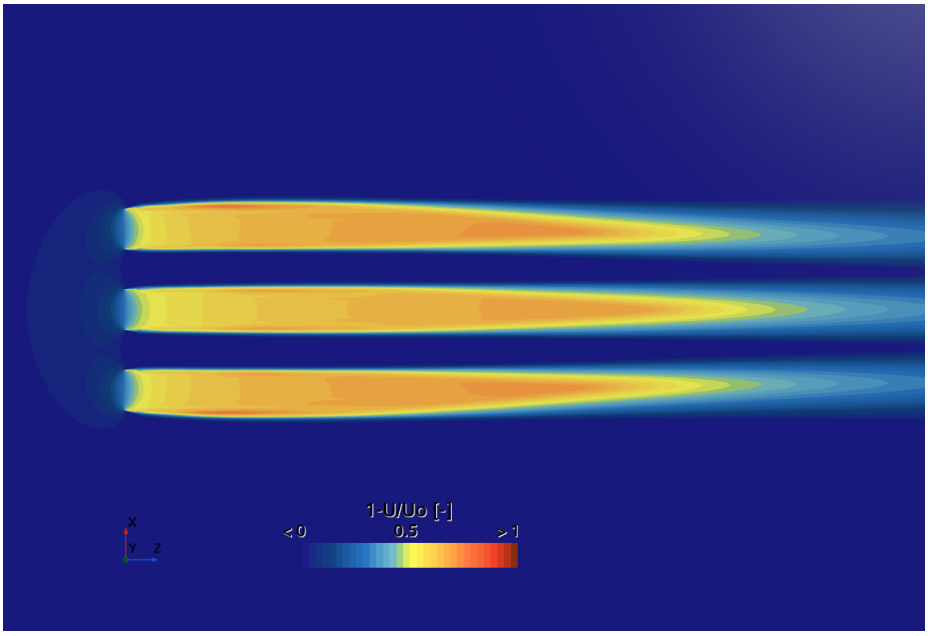

Figure 4.32: *Velocity deficit field from CFD RANS simulations with s/d=1.0.*

Towards the end of the simulation domain, at four diameters downstream, it can be seen that the velocity deficit decreases towards zero. Another view on the wake development is shown in Figure 4.33.

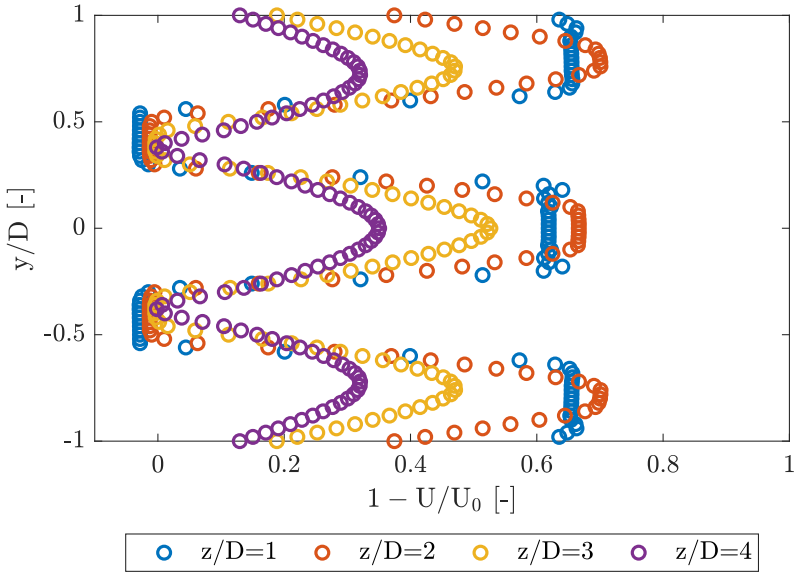

Figure 4.33: *Normalised velocity profile comparisons at different downstream locations (z/D) for RANS CFD simulations with an inter-rotor spacing of s/d=1.0, where D equals the total rotor diameter for the MR system.*

The wake development shows an increased velocity deficit from 1D to 2D, but from 2D to 3D and further to 4D it can be observed that the wake recovers well, having peaks at 0.35 at 4D

compared to 0.7 at 2D. However, the wake retains its W-shape, further illustrating the lack of mixing between the free stream velocity and the rotor wake. The mean velocities at each downstream distance are shown in Table 4.3.

Table 4.3: *Mean velocities at different downstream distances for the CFD simulation with optimal inter-rotor spacing of s/d=1.0. The free stream velocity is equal to 7.5 m/s.*

Downstream distance	**Mean velocity [m/s]**
1D	4.45
2D	4.57
3D	5.36
4D	5.87

The optimal inter-rotor spacing of s/d=1.0 is in contradiction to findings from Nishino and Wilden [78]. Their findings on the maximum global power coefficient for an array of tidal turbines indicated an optimal spacing of s/d=0.25. It was also discovered that for this inter-rotor spacing, the efficiency exceeded the Betz limit of 0.593 to an even higher efficiency value of 0.798. Based on the findings by Nishino and Wilden [78] it was expected to find the optimal inter-rotor spacing for the multi-rotor configuration somewhere between s/d=0.0 and s/d=1.0. However, as discussed in Section 4.2 and 4.3, the lack of mixing and recovery in the wake may affect the simulated thrust force and power output from the RANS simulations, giving conflicting results to what has been calculated by Nishino and Wilden.

- This page is intentionally left blank -

Chapter 5

Conclusion

This thesis aimed to build computationally efficient simulation models for wind turbine research and find the optimal inter-rotor spacing for maximising the performance from a multi-rotor wind turbine configuration with seven rotors. A single-rotor computational model was first built, using two different approaches. At first, the simulation model was attempted to be built based on porous disc data. Porous disc experiments in MarinLab provided detailed measurements of the behaviour of the disc, and a Detached Eddy Simulation was also performed to verify the disc measurements. Several different approaches for simulating the porous disc were performed using the virtual disk environment with varying results.

Introducing the ForWind model wind turbine and comparing simulation results with BEM calculations in QBlade and experimental data obtained by Neunaber [25] indicated a match in the rotor plane, but larger deviations were observed in the wake, likely due to the computational limitations of the RANS turbulence model. A lack of mixing between the wake and the free stream velocity was observed, in addition to a lack of velocity recovery in the wake. However, given the equalities in the rotor plane, the simulation model was deemed accurate enough to proceed with multi-rotor simulations.

Multi-rotor simulations compared with experimental data from Koi [21] showed slightly different trends. Where Koi discovered that the thrust force decreased with increasing inter-rotor spacing, the CFD simulations showed an increase in thrust force with increased spacing between rotors. Multi-rotor simulations of the wake showed a lack of mixing, resulting in

W-shaped wake profiles instead of Gaussian-shaped ones as obtained in experiments by Skoland [23]. The single rotors are being moved around to create a multi-rotor model, which may affect the interaction between rotors. The lack of wake mixing and recovery may be a contributor to the inconsistent results obtained from the RANS simulations. As the velocity in the wake directly influences the pressure drop and forces in the rotor plane, deviations in the wake may lead to consequential errors obtained for both thrust force and power output.

Through an optimisation study based on RANS simulations combined with a Kriging surrogate based model, the maximum possible inter-rotor spacing tested of s/d=1.0 was found optimal for maximising the performance of the multi-rotor system. This inter-rotor spacing was deemed optimal for maximising the power- and thrust coefficients as well as minimising the velocity deficit in the wake downstream of the rotor. These results are in contradiction to theoretical calculations from Nishino and Wilden [78], where an optimal inter-rotor spacing of s/d=0.25 was found for maximising the power coefficient. Additionally, their calculations indicated that the inter-rotor spacing value should lay somewhere between s/d=0.0 and s/d=1.0.

Chapter 6

Future Work

To obtain more accurate results in the wake downstream of the multi-rotor system, a Large Eddy Simulation (LES) can be performed to include more detailed information about the wake flow. The distance the wake needs to recover may also be studied, which is relevant for multi-rotor wind farm studies. However, LES studies are time-consuming and computationally expensive. Alternatively, a framework based on the reformulated vortex particle method such as FLOWUnsteady may be utilised. This method utilises LES to solve the Navier-Stokes equations in their vorticity form [79].

Several other aspects may be investigated once the wake simulations are validated and produce reliable results. One of them could be an optimisation of yaw angles in multi-rotor setups as done in Speakman et al. [80]. This study investigated different ways of yawing an MR4 setup, and results showed that all of the yaw configurations led to lower velocity deficits in the wake.

Another goal of multi-rotor configuration optimisation could be also to maximise the kinetic energy combined in the MR7 wake, considering that these MR systems might be set up in wind farm configurations. Maximising the kinetic energy in the wake would lead to more energy available for extraction in the wind for downstream wind turbines.

References

[1] Det Norske Veritas. ENERGY TRANSITION OUTLOOK 2023. Forecast, October 2023.

[2] United Nations Climate Change. The Paris Agreement. URL https://unfccc.int/process-and-meetings/the-paris-agreement. Accessed: 22.03.2023.

[3] United Nations. Renewable energy – powering a safer future. URL https://www.un.org/en/climatechange/raising-ambition/renewable-energy. Accessed: 15.01.2024.

[4] European Environment Agency. Share of energy consumption from renewable sources in Europe, 2024. URL https://www.eea.europa.eu/en/analysis/indicators/share-of-energy-consumption-from. Accessed: 30.05.2024.

[5] UNFCCC. Nationally determined contributions under the Paris Agreement. Synthesis report by the secretariat. Synthesis reports, United Nations Framework Convention on Climate Change, November 2023.

[6] H. Wagner and J. Mathur. *Introduction to Wind Energy Systems*. Springer, Berlin (DE), 2009.

[7] T. Ackermann and L. Söder. An overview of wind energy-status 2002. *Renewable and Sustainable Energy Reviews*, 6(1):67–127, 2002. ISSN 1364-0321. doi: 10.1016/S1364-0321(02)00008-4.

[8] A. Bonou, A. Laurent, and S. I. Olsen. Life cycle assessment of onshore and offshore wind energy-from theory to application. *Applied Energy*, 180:327–337, 2016. ISSN 0306-2619. doi: 10.1016/j.apenergy.2016.07.058.

[9] G. A. Heath, P. O'Donoughue, D. J. Arent, and M. Bazilian. Harmonization of initial

estimates of shale gas life cycle greenhouse gas emissions for electric power generation. *Proceedings of the National Academy of Sciences*, 111(31):E3167–E3176, 2014. doi: 10.1073/pnas.1309334111.

[10] M. Whitaker, G. A. Heath, P. O'Donoughue, and M. Vorum. Life Cycle Greenhouse Gas Emissions of Coal-Fired Electricity Generation. *Journal of Industrial Ecology*, 16(s1): S53–S72, 2012. doi: 10.1111/j.1530-9290.2012.00465.x.

[11] G. Brindley G. Constanzo and P. Cole. Wind energy in Europe. Technical report, Wind Europe, Brussels, Belgium, 2023.

[12] G. Sieros, P. Chaviaropoulos, J. D. Sørensen, B. H. Bulder, and P. Jamieson. Upscaling wind turbines: theoretical and practical aspects and their impact on the cost of energy. *Wind Energy*, 15(1):3–17, 2012. doi: 10.1002/we.527.

[13] P. Verma. Multi Rotor Wind Turbine Design And Cost Scaling. Master's thesis, University of Massachusetts Amherst, February 2014.

[14] P. Jamieson and M. Branney. Multi-rotors; A Solution to 20 MW and Beyond? *Energy Procedia*, 24:52–59, 2012. ISSN 1876-6102. doi: 10.1016/j.egypro.2012.06.086.

[15] M. P. van der Laan, S. J. Andersen, N. Ramos García, N. Angelou, G. R. Pirrung, S. Ott, M. Sjöholm, K. H. Sørensen, J. X. Vianna Neto, M. Kelly, T. K. Mikkelsen, and G. C. Larsen. Power curve and wake analyses of the Vestas multi-rotor demonstrator. *Wind Energy Science*, 4(2):251–271, 2019. doi: 10.5194/wes-4-251-2019.

[16] N. Ghaisas, A. Ghate, and S. Lele. Large-eddy simulation study of multi-rotor wind turbines. *Journal of Physics: Conference Series*, 1037:072021, jun 2018. doi: 10.1088/1742-6596/1037/7/072021.

[17] M. Bastankhah and M. Abkar. Multirotor wind turbine wakes. *Physics of Fluids*, 31(8): 085106, 2019. doi: 10.1063/1.5097285.

[18] M.P. van der Laan and M. Abkar. Improved energy production of multi-rotor wind farms. *Journal of Physics: Conference Series*, 1256(1):012011, jul 2019. doi: 10.1088/1742-6596/1256/1/012011.

[19] P. Chasapogiannis, J. Prospathopoulos, S. Voutsinas, and P.K. Chaviaropoulos. Analysis of the aerodynamic performance of the multi-rotor concept. *Journal of Physics: Conference Series*, 524(1):012084, 2014. doi: 10.1088/1742-6596/524/1/012084.

[20] T. Nishino and S. Draper. Local blockage effect for wind turbines. *Journal of Physics: Conference Series*, 625(1):012010, jun 2015. doi: 10.1088/1742-6596/625/1/012010.

[21] I. Koi. Aerodynamic Interaction Effects on a Multi-Rotor Wind Turbine. Master's thesis, University of Bergen, June 2022.

[22] A. Jørs and T. Mjåtveit. Wake flow lab measurements of multi-rotor wind turbines. Bachelor's thesis, Western Norway University of Applied Sciences, June 2021.

[23] M. Skoland. Experimental investigation of multirotor wind turbine wakes. Master's thesis, University of Bergen, June 2022.

[24] S. Øye. Experimental Study of the Wake Flow and Thrust Coefficient of Porous Actuator Discs. Master's thesis, University of Bergen, June 2022.

[25] I. Neunaber. *Stochastic investigation of the evolution of small-scale turbulence in the wake of a wind turbine exposed to different inflow conditions*. PhD thesis, Carl von Ossietzku Universität Oldenburg, 2019.

[26] M. O. L. Hansen. *Aerodynamics of Wind Turbines*. Earthscan, London (UK), 2nd edition, 2008.

[27] Airfoil Design 101: What Is an Airfoil?, March 2022. URL `https://www.naa.edu/airfoil-design/`. Accessed: 09.10.2023.

[28] Y.A. Çengel and J.M. Cimbala. *Fluid Mechanics: Fundamentals and Applications*. McGraw-Hill Education, Singapore (SG), 4th edition, 2020.

[29] A.L. Rogers J.F. Manwell, J.G. McGowan. *WIND ENERGY EXPLAINED Theory, Design and Application*. Wiley, West Sussex (UK), 2nd edition, 2009.

[30] P. Moriarty and A. Hansen. Aerodyn theory manual. *National Renewable Energy Laboratory*, jan 2005. doi: 10.2172/15014831.

[31] R. Barthelmie, K. S. Hansen, S. Frandsen, O. Rathmann, J. Schepers, W. Schlez, J. Phillips, K. Rados, A. Zervos, E. Politis, and P.K. Chaviaropoulos. Modelling and Measuring Flow and Wind Turbine Wakes in Large Wind Farms Offshore. *Wind Energy*, 12:431 – 444, jul 2009. doi: 10.1002/we.348.

[32] L.J. Vermeer, J.N. Sørensen, and A. Crespo. Wind turbine wake aerodynamics. *Progress in Aerospace Sciences*, 39(6):467–510, 2003. ISSN 0376-0421. doi: 10.1016/S0376-0421(03)00078-2.

[33] Y. Li, Z. Xu, Z. Xing, B. Zhou, H. Cui, B. Liu, and B. Hu. A Modified Reynolds-Averaged Navier–Stokes-Based Wind Turbine Wake Model Considering Correction Modules. *Energies*, 13(17), 2020. ISSN 1996-1073. doi: 10.3390/en13174430.

[34] University of Bergen. Boundary Layer Meteorology, February 2014. URL `https://www.uib.no/en/rg/meten/53207/boundary-layer-meteorology`. Accessed: 30.11.2023.

[35] M. Abkar and F. Porté-Agel. The effect of atmospheric stability on wind-turbine wakes: A large-eddy simulation study. *Journal of Physics: Conference Series*, 524(1):012138, jun 2014. doi: 10.1088/1742-6596/524/1/012138.

[36] P. A. Lynn. *Onshore and offshore wind energy*. Wiley-Blackwell, New Jersey (US), 2011.

[37] Y. Li, Z. Xu, Z. Xing, B. Zhou, H. Cui, B. Liu, and B. Hu. A comparison of lab-scale free rotating wind turbines and actuator disks. *Energies*, 209(17), 2020. ISSN 0167-6105. doi: 10.3390/en13174430.

[38] M. Gaumond, P-E. Réthoré, S. Ott, A. Peña, A. Bechmann, and K. S. Hansen. Evaluation of the wind direction uncertainty and its impact on wake modeling at the Horns Rev offshore wind farm. *Wind Energy*, 17, aug 2014. doi: 10.1002/we.1625.

[39] R. J. Barthelmie and L. E. Jensen. Evaluation of wind farm efficiency and wind turbine wakes at the Nysted offshore wind farm. *Wind Energy*, 13(6):573–586, 2010. doi: 10.1002/we.408.

[40] K. S. Hansen, P.-E. Réthoré, J. Palma, B. G. Hevia, J. Prospathopoulos, A. Peña, S. Ott, G. Schepers, A. Palomares, M. P. van der Laan, and P. Volker. Simulation of wake effects between two wind farms. *Journal of Physics: Conference Series*, 625(1):012008, jun 2015.

doi: 10.1088/1742-6596/625/1/012008.

[41] K. S. Hansen, R. J. Barthelmie, L. E. Jensen, and A. Sommer. The impact of turbulence intensity and atmospheric stability on power deficits due to wind turbine wakes at Horns Rev wind farm. *Wind Energy*, 15(1):183–196, 2012. doi: 10.1002/we.512.

[42] T. Eriksen. Flow measurements in the wake of multirotor wind turbine arrangements. Master's thesis, University of Bergen, June 2023.

[43] S. Helvig, M. K. Vinnes, A. Segalini, N. A. Worth, and R. J. Hearst. A comparison of lab-scale free rotating wind turbines and actuator disks. *Journal of Wind Engineering and Industrial Aerodynamics*, 209:104485, 2021. ISSN 0167-6105. doi: 10.1016/j.jweia.2020.104485.

[44] J. W. Kurelek, A. Piqué, and M. Hultmark. Performance of the porous disk wind turbine model at a high Reynolds number: Solidity distribution and length scales effects. *Journal of Wind Engineering and Industrial Aerodynamics*, 237:105377, 2023. ISSN 0167-6105. doi: 10.1016/j.jweia.2023.105377.

[45] M. H. Ranjbar, H. Z. Kia, S. A. Nasrazadani, Kobra G., and J. Nathwani. Experimental and numerical investigations of actuator disks for wind turbines. *Energy Science & Engineering*, 8(7):2371–2386, 2020. doi: 10.1002/ese3.670.

[46] B. Öztürk, A. Hassanei, A. Abdulrahim, M. Percin, and O. Uzol. Effects of freestream turbulence on the wake growth rate of a model wind turbine and a porous disc. *Journal of Physics Conference Series*, 2265, jun 2022. doi: 10.1088/1742-6596/2265/2/022042.

[47] L. Lignarolo, D. Ragni, C. Ferreira, and G. van Bussel. Experimental comparison of a wind-turbine and of an actuator-disc near wake. *Journal of Renewable and Sustainable Energy*, 8:023301, mar 2016. doi: 10.1063/1.4941926.

[48] L. Lignarolo, D. Ragni, C. Ferreira, and G. van Bussel. Turbulent mixing in wind turbine and actuator disc wakes: An experimental analysis. *33rd Wind Energy Symposium*, jan 2015. doi: 10.2514/6.2015-0223.

[49] P. Hulsman, M. Wosnik, V. Petrović, M. Hölling, and M. Kühn. Development of a curled wake of a yawed wind turbine under turbulent and sheared inflow. *Wind Energy Science*,

7(1):237–257, 2022. doi: 10.5194/wes-7-237-2022.

[50] J. Schottler, J. Bartl, F. Mühle, L. Sætran, J. Peinke, and M. Hölling. Wind tunnel experiments on wind turbine wakes in yaw: redefining the wake width. *Wind Energy Science*, 3 (1):257–273, 2018. doi: 10.5194/wes-3-257-2018.

[51] M. A. Miller, J. Kiefer, C. Westergaard, M. O. L. Hansen, and M. Hultmark. Horizontal axis wind turbine testing at high Reynolds numbers. *Physical Review Fluids*, 4:110504, nov 2019. doi: 10.1103/PhysRevFluids.4.110504.

[52] L. Sætran, F. Mühle, J. Bartl, J. Schottler, M. Hölling, and M. S. Adaramola. Invitation to the 2017 "Blind test 5" workshop - The wake behind a yawed wind turbine. Technical report, Norwegian Institute of Science and Technology (NTNU), Norwegian University of Life Sciences (NMBU) and Carl-von-Ozzietzky University of Oldenburg, 2017.

[53] M. S. Selig, J. J. Guglielmo, A. P. Broeren, and P. Giguère. *Summary of Low-Speed Airfoil Data*, volume 1. SoarTech Publications, Virginia Beach (US), 1995. ISBN 0-9646747-1-8.

[54] J. Blazek. *"Computational Fluid Dynamics: Principles and Applications"*. Elsevier, Oxford (UK), 2nd edition, 2005.

[55] *Simcenter STAR-CCM+ 2310 User Guide*. Siemens Digital Industries Software, 2023.

[56] M. Acker. *A 2D CFD Simulation for Wind Turbine Wakes Using a Porous Element*. PhD thesis, Northern Arizona University, 2018.

[57] University of Waterloo. Vorticity, December 2014. URL `https://uwaterloo.ca/applied-mathematics/current-undergraduates/continuum-and-fluid-mechanics-students/amath-463-students/vorticity`. Accessed: 11.03.2024.

[58] D. C. Wilcox. *Turbulence Modeling for CFD*. DCW Industries, California (US), 3rd edition, 2006.

[59] J. O. Hinze. *Turbulence*. McGraw-Hill Book Company, Inc., New York (US), 1959.

[60] W.P. Jones and B. Launder. The prediction of laminarization with a two-equation model of turbulence. *International Journal of Heat and Mass Transfer*, 15:301–314, 02 1972. doi:

10.1016/0017-9310(72)90076-2.

[61] B. Launder and B. Sharma. Application of energy dissipation model of turbulence to the calculation of flow near spinning disc. *Letters Heat Mass Transfer*, 1:131–137, 11 1974. doi: 10.1016/0735-1933(74)90024-4.

[62] C.D. Argyropoulos and N.C. Markatos. Recent advances on the numerical modelling of turbulent flows. *Applied Mathematical Modelling*, 39(2):693–732, 2015. ISSN 0307-904X. doi: 10.1016/j.apm.2014.07.001.

[63] A. N. Kolmogorov. Equations of turbulent motion in an incompressible fluid. *Proceedings of the USSR Academy of Sciences*, 30:299–303, 1941.

[64] B. E. Launder and D. B. Spalding. Mathematical models of turbulence. *Academic Press*, 1972.

[65] J. Mcnaughton, S. Rolfo, D. Apsley, I. Afgan, T. Stallard, and P. Stansby. CFD Prediction of Turbulent Flow on an Experimental Tidal Stream Turbine using RANS modelling. Jeju, South Korea. 1st Asian Wave and Tidal Energy Conference, 27-30 November 2012.

[66] N. Stergiannis, C. Lacor, J. V. Beeck, and R. Donnelly. CFD modelling approaches against single wind turbine wake measurements using RANS. *Journal of Physics: Conference Series*, 753(3):032062, sep 2016. doi: 10.1088/1742-6596/753/3/032062.

[67] D. Garcia-Ribeiro, V. Malatesta, R. Moura, and H. Cerón-M. Assessment of RANS-type turbulence models for CFD simulations of horizontal axis wind turbines at moderate Reynolds numbers. *Journal of the Brazilian Society of Mechanical Sciences and Engineering*, 45, oct 2023. doi: 10.1007/s40430-023-04488-0.

[68] K. Boorsma and J. G. Schepers. Description of experimental setup, New Mexico experiment. *Techical Report ECN-X15-093 ECN*, 2015.

[69] QBlade. Information About QBlade Software, July 2022. URL `https://qblade.org/about-qblade-software/`. Accessed: 25.03.2024.

[70] D. Marten, J. Peukert, G. Pechlivanoglou, C. Nayeri, and C. Paschereit. QBLADE: An Open Source Tool for Design and Simulation of Horizontal and Vertical Axis Wind Turbines.

International Journal of Emerging Technology and Advanced Engineering, 3:264–269, mar 2013.

[71] M. Alaskari, O. Abdullah, and M. H. Majeed. Analysis of Wind Turbine Using QBlade Software. *IOP Conference Series: Materials Science and Engineering*, 518(3):032020, may 2019. doi: 10.1088/1757-899X/518/3/032020.

[72] G. I. Taylor. Air resistance of a flat plate of very porous material. *Reports of the Memoranda of the Aeronautical Research Council, no. 2236*, 1944.

[73] T. Hansen. *Aerodynamic Optimisation of Airfoils and Winglets for Wind Turbine Application*. PhD thesis, Norwegian University of Science and Technology, 2017.

[74] J. R. R. A. Martins and A. Ning. *Engineering Design Optimization*. Cambridge University Press, Jan 2022. ISBN 9781108833417.

[75] T. H. Hansen and F. Mühle. Winglet optimization for a model-scale wind turbine. *Wind Energy*, 21(8):634–649, 2018. doi: 10.1002/we.2183.

[76] J. Bartl and L. Sætran. Blind test comparison of the performance and wake flow between two in-line wind turbines exposed to different turbulent inflow conditions. *Wind Energy Science*, 2(1):55–76, 2017. doi: 10.5194/wes-2-55-2017.

[77] L. A. Martínez-Tossas, E. Branlard, K. Schaler, G. Vijayakumar, S. Ananthan, P. Sakievich, and J. Jonkman. Numerical investigation of wind turbine wakes under high thrust coefficient. *Wind Energy*, 25(4):605–617, 2022.

[78] T. Nishino and R. H. J. Willden. The efficiency of an array of tidal turbines partially blocking a wide channel. *Journal of Fluid Mechanics*, 708:596–606, 2012. doi: 10.1017/jfm.2012.349.

[79] E. Alvarez, J. Mehr, and A. Ning. FLOWUnsteady: An Interactional Aerodynamics solver for Multirotor Aircraft and Wind Energy. *AIAA Aviation Forum*, 2022. doi: 10.2514/6.2022-3218.

[80] G. A. Speakman, M. Abkar, L. A. Martínez-Tossas, and M. Bastankhah. Wake steering of multirotor wind turbines. *Wind Energy*, 24(11):1294–1314, 2021. doi: 10.1002/we.2633.